Quantifying Columbia River Flood Basalt Eruption Durations Using the Resetting of Low-Temperature Thermochronometers Next to Dikes

by

Rebecca Goughnour

A thesis

submitted in partial fulfillment

of the requirements for the degree of

Master of Science in the Department of Geosciences

Idaho State University

Summer 2022

Photocopy and Use Authorization

In presenting this thesis in partial fulfillment of the requirements for an advanced degree at Idaho State University, I agree that the Library shall make it freely available for inspection. I further state that permission for extensive copying of my thesis for scholarly purposes may be granted by the Dean of the Graduate School, Dean of my academic division, or by the University Librarian. It is understood that any copying or publication of this thesis for financial gain shall not be allowed without my written permission.

Signature ___________________________________

Date _______________________________________

Committee Approval

To the Graduate Faculty:

The members of the committee appointed to examine the thesis of Rebecca Goughnour find it satisfactory and recommend that it be accepted.

Dr. Kendra E. Murray,
Major Advisor

Dr. David M. Pearson,
Committee Member

Dr. Tracy Payne
Graduate Faculty Representative

Acknowledgements

First and foremost, a big thank you to Kendra Murray and Dave Pearson for your extremely constructive feedback throughout this whole process. I've learned so much from you over these past two years—how to crush rocks, how much caffeine is "just the right amount" when picking and packing zircons, the difference between "further" and "farther" (which I'll most likely continue to mess up), and probably a few other things too. I've grown a lot throughout this program, and I credit a good portion of that growth to your mentorship.

Thank you to Leif Karlstrom at the University of Oregon, whose modeling expertise was essential to this project. Your patience in taking the time to answer my *many* questions and to help me troubleshoot code have been greatly appreciated. This research has also been greatly enriched through my collaboration with Rachel Hampton (UO) and Joe Biasi (UO and Dartmouth) both in and out of the field area. Rachel, thank you for inspiring me with your enthusiasm for the Maxwell Lake study area. You have been a continual role model for me, and I've learned so much from you throughout these two years.

To the graduate students at Idaho State University, thank you for creating the absolute best department culture anyone could dream of. To Kyra, Kyle, Josh, Andrew, and Gene thanks for always loitering in my office and distracting me when I was desperately trying to work (and for being amazing friends in so many ways). To Tyler Paladino, I would be absolutely lost without both your Matlab expertise and your general goofy shenanigans. Thank you for introducing me to so many good songs, letting me steal your computer dongle and tea every day, and reminding me to laugh even when life seems pretty bleak. And to Lindsey Sutherland, you've been there for me since day one at ISU. Thank you for helping me through pretty much every difficult thing that has happened in the past two years—you are a force of nature!

Finally, thanks to the Arizona Radiogenic Helium Dating Laboratory at the University of Arizona for running my (U-Th)/He analyses, Paul O'Sullivan and everyone at GeoSep Services for processing my fission-track analyses, Stephen Cox at Lamont-Doherty Earth Observatory for your help processing my Biotite $^{40}Ar/^{39}Ar$ analyses, and Million Hailemichael at ISU for your help running my apatite hydrogen isotope analyses. Also, thank you to Adrianna Gibson for processing many of my samples at ISU. This research is based upon work supported by the National Science Foundation under Grant Nos. EAR-1759200 and EAR-1759353. Thanks to the AGeS program for its support.

TABLE OF CONTENTS

List of Figures

List of Tables

Quantifying Columbia River Flood Basalt Eruption Durations Using the Resetting of Low-Temperature Thermochronometers Next to Dikes

Thesis Abstract--Idaho State University (2022)

The high-volume, short-duration magmatism that forms large igneous provinces (LIPs), such as the Miocene Columbia River Flood Basalts (CRFBs), has been linked to paleo-biospheric perturbations. To accurately assess the climatic impacts of these LIP events, the durations of individual eruptions need to be measured at the scale of years-decades, i.e., 2-3 orders of magnitude higher resolution than the highest-precision geochronometers. I use the thermal footprints of dikes that fed CRFB eruptions (measured by thermochronology and stable isotopes) to quantify the duration of magma flow through these dikes, better understand the transport of magma across multiple dike segments, and measure the extent of hydrothermal circulation during dike emplacement. Numerical modeling of thermochronologic ages yields magma flow durations of 2.2-11 years at one dike segment. Additional thermochronologic transects suggest that there was spatial variability in dike-adjacent heat transfer. Finally, hydrogen isotope data suggests that dike emplacement triggered the circulation of meteoric fluids.

Key Words: Columbia River Flood Basalts, thermochronology, magma flow duration, numerical modeling

Chapter 1: Introduction

Large igneous provinces (LIPs) are the products of Earth's most voluminous volcanic events, characterized by more than 100,000 km^3 of volcanic material erupted over a period of less than 5 myr (Bryan and Ernst, 2008; Black et al., 2021). These rapid and prodigious eruptions release volatiles into the atmosphere (such as CO_2, SO_2, and halogens dissolved in magma), which can significantly perturb Earth's climate and biosphere (Bond and Wignall, 2014). To better measure the magnitudes of these perturbations and assess their climatic significance in the geologic record, it is necessary to calculate the magmatic, and therefore volatile, fluxes that occur during LIP eruptions. Most studies of LIP eruptive timescales measure the absolute ages of lava flows or interbedded ash horizons using geochronology, extracting time-averaged eruptive rates over multiple lava flows (e.g., Burgess and Bowring, 2015; Kasbohm and Schoene, 2018; Schoene et al., 2019; Sprain et al., 2019). However, these studies average over eruptive hiatuses, and even the most precise geochronologic methods have uncertainties of ~10,000 years and are therefore unable to distinguish between eruption durations of years, decades, or millennia. This limitation in timescale resolution may underestimate volatile pulses during individual LIP eruptions and is insufficient for assessing the impact of magmatic flux on the climate system. Therefore, the question remains: What is the tempo of individual LIP eruptions? To answer this question, I focus on the magmatic conduits of surface flows (i.e., feeder dikes), rather than the lava flows themselves, and use the widths of thermal imprints around individual feeder dike segments as proxies for how long the dike segments were actively transporting magma to surface flows.

This thesis is organized into six chapters. Chapter 2 introduces the geologic background of the LIP, the Columbia River Flood Basalts (CRFBs), that is discussed in the following chapters. Chapter 2 is an overview of the thermochronologic tools used in Chapters 3 and 4. In Chapter 3, I use a numerical model to quantify the duration of magma flow through a CRFB dike exposed in the Wallowa Mountains, Oregon, using the width of the dike's thermal imprint as measured by low-temperature thermochronometers. Chapter 4 qualitatively compares the thermochronologic imprint of three dike segments in the Maxwell Lake area of the Wallowa Mountains to preliminarily assess how magma was transferred through the crust during the main eruptive phase of the CRFBs. Chapter 5 measures the extent of hydrothermal activity generated during the emplacement of a CRFB dike using hydrogen isotopes measured in the mineral apatite. Finally, Chapter 6 summarizes the findings from Chapters 3, 4, and 5 into final conclusions.

Chapter 2: Background and Introduction to Thermochronology

2.1 Columbia River Flood Basalt Eruption Durations

The Miocene Columbia River Flood Basalts (CRFBs) are the youngest and most well-exposed LIP on Earth today, and years of research have attempted to determine how quickly CRFB lava flows erupted (Shaw and Swanson, 1970; Self et al., 1996; Reidel, 1998; Petcovic and Dufek, 2005; Reidel et al., 2013; Kasbohm and Schoene, 2018; Karlstrom et al., 2019; Biasi and Karlstrom, 2021). The CRFBs erupted ~210,000 km^3 of basaltic andesite across Washington, Oregon, and Idaho (Figure 2.1) during seven episodes (Figure 2.2; Reidel et al., 2013). Three of these episodes, which produced the Imnaha, Grande Ronde, and the Wanapum formations, contributed 82% of the total CRFB eruptive volume over only ~700 kyr and may have contributed to the Mid-Miocene Climatic Optimum (Kasbohm and Schoene, 2018; Figure 2.2). Although a ~700 kyr timeframe for this main eruptive phase suggests an impressive eruptive rate for these basalts, important information about intra-LIP eruptive hiatuses and individual eruption durations is still lacking. Without a clear consensus on individual eruption durations, it is impossible to accurately assess the climatic impact of the CRFBs.

The duration of individual CRFB eruptions has been widely debated: Previous work from Shaw and Swanson (1970) advocated for rapid, turbulent CRFB lava emplacement over days to weeks. In contrast, Self et al. (1996) used mapping of compound pahoehoe flows to advocate for slow inflation of the lava flows over many years. Later work by Reidel (1998), which focused on flow members from the Saddle Mountain Formation, used evidence of intermixed flows to once again advocate for rapid emplacement, perhaps only a few months.

More recent work by Kasbohm and Schoene (2018) used high-resolution U-Pb dating of zircon crystals through isotope dilution thermal ionization mass spectrometry to constrain the ages of interbedded ash horizons from the Steens, Imnaha, Grande Ronde, and Wanapum formations, allowing for a more comprehensive understanding of time-averaged eruption rates. Despite improving geochronologic constraints on the CRFBs, their absolute ages still have uncertainties of at least 10,000 years– a resolution that fails to distinguish between individual eruptions occurring over years, decades, or millennia.

One alternative to using absolute ages to measure the tempos of LIP eruptions is to use numerical modeling to interpret the duration of magma flow through feeder dikes (Petcovic and Dufek, 2005; Karlstrom et al., 2019; Biasi and Karlstrom, 2021). For example, Petcovic and Grunder (2003) used systematic changes in the mineralogy of wallrock partial-melt zones next to a CRFB feeder dike to estimate that this crustal melting, driven by dike heating, took place over a four year period. The dike segment they studied (hereafter referred to as the Maxwell A dike) is geochemically linked to the voluminous Wapshilla Ridge member (~40,000 km^3; Reidel et al., 2013), which is the largest group of lava flows in the CRFBs. Thus, a constraint on the duration of this eruption would therefore represent end-member behavior for CRFB lava flows. Continuing this work, Petcovic and Dufek (2005) capitalized on the relationship between heating during dike emplacement and the spatial distribution of partial melt textures next to a dike (observed in Petcovic and Grunder, 2003) to inform different models for magma flow duration. Based on the presence of a 4 m partial melt zone next to the Maxwell A dike, their model suggested 3-4 years of sustained, steady magma flow. Using the length and width of the Maxwell A dike segment, this inferred eruption duration suggests a magmatic flux of 3-5 km^3 per day to erupt a typical flow of the Wapshilla Ridge member (Petcovic and Grunder, 2005). This modeling technique is able to constrain much shorter eruptive timescales than absolute geochronologic ages alone; however, this calculation represents an upper estimate for flux given that more than one dike segment likely fed the Wapshilla Ridge flows.

Building on the approach used by Petcovic and Dufek (2005), new research has introduced additional tools for measuring transient heating adjacent to CRFB feeder dikes. For example, Karlstrom et al. (2019) used resetting in two low-temperature thermochronometers to quantify the duration of magma flow in two CRFB dikes, and Biasi and Karlstrom (2021) used the resetting of paleomagnetic inclination in wallrocks as proxies for the duration of magma flow through CRFB dikes. When inverse models, rather than forward models, are implemented (as in Karlstrom et al., 2019), key parameters related to magma flow can be quantified. For Karlstrom et al. (2019), a Bayesian Markov-Chain Monte Carlo inversion yielded magma flow durations of 1-6 years.

In this study, I build upon the Karlstrom et al. (2019) method because it has the power to resolve dike emplacement timescales on the order of years. The many of the dikes that were investigated in the aforementioned studies (Table 2.1) are located in the Wallowa Mountains of northeastern Oregon. In the Wallowa Mountains, localized exhumation has exposed the upper two km of the CRFB's shallow crustal plumbing system, the Chief Joseph dike swarm (Reidel and Tolan, 2013). The Chief Joseph dike swarm transported magma during both the Imnaha and Grande Ronde eruptive phases of the CRFBs ca. 16.6-16.1 Ma (Morriss et al., 2020). These basaltic dikes were emplaced into ca. 130 Ma granitoid wallrocks in the Wallowa Mountains (Žák et al., 2015) To determine the duration of individual CRFB eruptions, I focus on constraining magma flow duration through long-lived feeder dikes of the Chief Joseph dike swarm. Identification of these long-lived feeder dikes in the field was based on the premise that the presence of partially melted granite at the dikes' margins suggests that these dikes acted as long-term heat sources.

2.2 Thermochronology as a Tool for Studying Dike Emplacement

Because of the pronounced age and compositional contrast of the basaltic dikes (ca. 16 Ma) and their granitoid wallrocks (ca. 130 Ma) in the Wallowa Mountains, the thermal impacts of individual dike intrusions are observable using the resetting of low-temperature chronometers that reside in the surrounding wallrock (Figure 2.3). Although low-temperature chronometers are commonly used for constraining events over geologic (>1 myr) timescales (Gautheron and Zietler, 2020), these chronometers can also be reset by high-temperature events occurring over minutes to decades (Calk and Naeser, 1973; Reiners, 2009). Therefore, resetting associated with the rapid emplacement of the Chief Joseph dike swarm can be observed in the granitoid country rock of the Wallowa Mountains, and the magnitude of resetting can be used to quantify how long certain dikes acted as conduits for individual CRFB surface eruptions.

Thermochronologic ages (i.e., cooling ages) reflect a rock's time-temperature (tT, thermal) history, and in this study I use cooling ages to document brief (years to decades) thermal perturbations. As with all radioisotopic ages, thermochronologic ages are calculated from the measured abundance of parent radionuclides and daughter products in minerals. Within a mineral, the production of daughter products occurs at a constant rate. However, in thermochronologic systems, the rate of diffusion of radiogenic daughter products out of a crystal (as well as annealing of damage within the crystal lattice) depends on temperature: at high temperatures, these systems are "open" and do not retain any daughter products, whereas at low temperature they become "closed" and daughter products are quantitatively retained.

Most commonly, thermochronology is used to document processes, such as erosion (e.g., Reiners and Brandon, 2006) that drive changes in rock temperature on geologic timescales (10^6 - 10^9 years). In such applications, closure temperature (T_c) is a mathematical determination of the temperature at which a noble gas thermochronometer became effectively closed and started accumulating daughter products (Dodson, 1973):

$$T_c = \frac{E_a/R}{ln\left[\frac{-ART_c^2\left(D_0/a^2\right)}{E_a(dT/dt)}\right]} \; (2.1)$$

given a specific and constant cooling rate (dT/dt), experimentally derived activation energy (E_a) and diffusivity at infinite temperature (D_0), the gas constant (R) the crystal size (a), and a geometric term (A). The closure-temperature concept is useful for both simple interpretations of cooling ages and describing the relative temperature sensitivities of different thermochronologic systems.

In this study, however, I focus on rock heating and cooling next to dike segments that occurs on timescales of days to decades. Rocks that experience high-temperature, short-duration heating events do not have cooling histories that can be characterized by a single cooling rate and therefore cooling ages from these rocks cannot be interpreted using the closure-temperature concept. Instead, heat pulses initiate fractional loss of radioisotopic daughters in proportion to the duration and temperature of heating. For noble gas thermochronometers, diffusivity (τ), and thus fractional loss of daughter product, varies as a function of time (t) and temperature (T; Karlstrom et al., 2019):

$$\tau(T,t) = \frac{D_0}{a^2}\int_0^t \exp\left[\frac{-E_a}{R}\frac{1}{T(t')}\right]dt'. \; (2.2)$$

Although E_a, R, a, and D_0 are the same parameters that are used in the closure temperature equation (2.1), $\tau(T,t)$ depends on the thermal history $T(t')$ of a rock. Once the diffusivity has been calculated throughout the heating event, τ can be used to calculate the total fractional loss (*f*) of the radioisotopic daughter through diffusion (Karlstrom et al., 2019),

$f = 1 - \frac{6}{\pi^2} \sum_{n=1}^{\infty} \frac{1}{n^2} \exp\left(-n^2 \pi^2 \tau\right)$. *(2.3)*

Finally, for any thermochronometer, the magnitude of fractional loss can be used to predict a measurable thermochronologic age (Karlstrom et al., 2019),

$A_f = f \times (A_i - A_r) + A_r$, *(2.4)*

where A_r is the unreset (unperturbed) thermochronologic age, A_r is the age of the heat pulse, and A_f is the fractionally reset thermochronologic age.

Wallrocks near a dike will reach higher peak temperatures than wallrocks far from the dike and, therefore, experience greater diffusive loss of daughter product (Figure 2.3). As a result, the spatial pattern of fractionally reset thermochronologic ages will reflect the distinctive thermal histories of the wallrocks, where chronometers experience full, partial, and no fractional loss with increasing distance from the dike (Calk and Naeser, 1973; Reiners, 2005). I refer to this spatial pattern of thermochronometer resetting as a “resetting curve”.

In addition to its dependence on thermal history, diffusivity (equation 2.2) is also highly dependent on the kinetics (E_a, D_0/a^2) of the chronometer being modeled. Each chronometer has a different set of kinetics that controls the rate of diffusion (or, in the case of fission-track thermochronometers, annealing) and, therefore, how sensitive the chronometer is to heating. For this study, I use several different thermochronometers to capture the thermal history of a dike in order to independently constrain both high and low temperature histories next to the dikes.

2.3 Sample Preparation and Analysis

2.3.1 Sample Processing and Crystal Selection

All samples (Table 2.2) were processed using standard crushing, sieving, magnetic, and density separation methods at Idaho State University. The typical workflow used in this study was as follows: samples were crushed using a chipmunk jaw crusher and disk-mill, sieved using 420 μm sieve fabric, density separated using a Wilfley table, and fed through a Frantz barrier magnetic separator at 0.5, 1, and 1.4 A intervals. Biotite crystals were handpicked from both the Wilfley light fraction and the 0.4 A Frantz fraction (for samples 2E1-2E9). The non-magnetic fraction from the Frantz was then immersed in tetrabromoethane, allowing all apatite and zircon crystals to separate from the non-magnetic fraction by density difference. Finally, the mixture of apatite and zircon crystals was added to methylene iodide, this time separating the two by density.

At this stage, aliquots of the apatite and zircon separates were used for fission-track analysis, and ~40-50 biotite crystals between 250-500 μm were picked for $^{40}Ar/^{39}Ar$ analysis. Preference was given to biotite crystals that were euhedral, unbroken, and consistent of only a single sheet (i.e., not a compound biotite booklet). Finally, individual apatite and zircon crystals were selected for (U-Th)/He analysis based on size, morphology, and clarity using a stereomicroscope (Figure 2.4).

2.3.2 Sample Analysis

(U-Th)/He thermochronology. Apatite (U-Th)/He *(*AHe) and zircon (U-Th)/He (ZHe) thermochronology are both based on the production of ^{4}He during alpha decay of U, Th, and Sm, as well as the diffusion of ^{4}He daughter from the crystal lattice during reheating events (e.g.,

Gautheron and Zeitler, 2020). For each sample, four apatite crystals and four zircon crystals were individually picked, packed, and sent to the Arizona Radiogenic Helium Dating Laboratory at the University of Arizona, where ages were generated by heating and extracting ^{4}He with a diode laser, spiking the ^{4}He sample with ^{3}He through isotope dilution, and measuring the concentration of U-Th-Sm using isotope dilution and inductively coupled plasma mass spectrometry. All analytical methods followed standard procedure for Arizona Radiogenic Helium Dating Laboratory (Reiners and Nicolescu, 2006).

Fission-track thermochronology. Rather than document the abundance of a radioisotopic nuclide, as in the (U-Th)/He system, fission-track thermochronology measures the abundance of damage within the crystal caused by the spontaneous fission of ^{238}U (Tagami and O'Sullivan, 2005; Hurford, 2019). During fission, recoil of daughter nuclei results in a line of crystallographic damage called a fission track. These tracks are produced at a rate in proportion to the abundance of U and anneal at different rates depending on the time and temperature conditions that the mineral has experienced. Calculating a fission-track age requires measurements of track density and ^{238}U concentration in the mineral.

To generate AFT and ZFT ages for this study, I sent bulk apatite and zircon separates to GeoSep Services, where crystals were mounted in epoxy and teflon, respectively, polished, and etched with HNO_3 and KOH respectively. Once etched, the fission tracks were counted. Confined track lengths were also measured in the apatite crystals. Rather than employ the traditional external detector method, GeoSep used laser ablation inductively coupled plasma mass spectrometry (Hasebe et al., 2004; Chew and Donelick, 2012) to determine each crystal's ^{238}U concentration.

40Ar/39Ar thermochronology. In the biotite $^{40}Ar/^{39}Ar$ system, the radioactive parent ^{40}K decays to both ^{40}Ar (via electron capture) and ^{40}Ca (via β-decay; Min et al., 2000). $^{40}Ar/^{39}Ar$ ages are calculated from the ratio of ^{40}Ar to ^{39}Ar, the latter of which is generated by neutron bombardment of ^{39}K in a nuclear reactor. These ages can be determined by total fusion, in which all of the Ar is liberated by melting the sample and then measured by mass spectrometry, or by step-heating, in which the sample is sequentially heated to release the Ar in stages. Step-heating analysis produces an age spectrum when plotted as a function of ^{39}Ar released and yields additional information about thermal history and composition that can be useful in geologic interpretation. In this study, biotite $^{40}Ar/^{39}Ar$ ages were generated through both single step fusion experiments and step-heating experiments at Lamont-Doherty Earth Observatory's Argon Geochronology for the Earth Sciences (AGES) lab. Below, more information is given about Ar analysis because the AGES lab does not currently have a published laboratory procedure to reference (Stephen Cox, personal comm).

Samples were irradiated at the USGS TRIGA Reactor for 17.5 hours ($J=3.6090 \times 10^{-3}$) with Fish Canyon Tuff sanidine monitor standard (28.201 ± 0.046 Ma, Kuiper et al., 2008; using decay constants of Min et al., 2000). Samples were loaded into disks based on procedures outlined in Renne et al. (1998), and then the stacked disks were wrapped in Al foil and placed into a cadmium-lined irradiation tube at the TRIGA facility.

After irradiation, samples were removed from disks and placed in 2 mm pits in a machined Ti sample holder under an ultra-high vacuum in a chamber made of stainless steel with a differentially-pumped ZnS viewport. Once in the Ti pits, each aliquot was heated using an automated Photon Machines CO_2 laser (10.6 µm wavelength) with a uniform 3 mm diameter beam completely covering the sample. Fused samples were heated for 30 seconds with 12%

output power after a 15 s ramp. Step-heated samples were sequentially heated using one of two step-heating schedules: six-step experiments used 0.1, 0.3, 0.5, 0.7, 1, and 12% power, while eight-step experiments used 0.1, 0.3, 0.5, 0.6, 0.7, 0.85, 1, and 12% power. Each heating step was 30 s at full power after 15 s ramp, and heating power was increased to generate gas release spectra until the sample was fully melted and degassed. Gases evolved during heating were exposed to a hot (~400 °C) SAES St 101 Zr-Al non-evaporable getter for five minutes.

Purified Ar was released from the getter chamber into the mass spectrometer for 30 seconds, during which the signal was monitored on all detectors. Ar isotopes were measured on an Isotopx NGX multicollector mass spectrometer (tuned for good sensitivity and best isotope ratio linearity), with the ion source set to 6000 V accelerating voltage and the trap current at 200 μA. To account for mass discrimination and instrument backgrounds, samples were heated with calibrated air standards and procedural blanks between every three heating steps. The isotopes 37Ar, 38Ar, 39Ar, and 40Ar were measured on ATONA Faraday detectors while the isotope 36Ar was measured on a Hamamatsu ion counting multiplier modified by Isotopx for the NGX. Isotope intensities were determined using background correction from the procedural blanks and a measured $^{40}Ar/^{36}Ar$ ratio correction using the air standards. The $^{40}Ar/^{39}Ar$ ratios for age determination were then calculated using nuclear interference corrections from Dalrymple et al. (1981), and a J value calculated using the Kuiper et al. (2008) age of 28.201 ± 0.046 Ma for the Fish Canyon Tuff sanidine monitor standard. Plateau ages were defined as three or more contiguous steps corresponding to a minimum of 50% of the ^{39}Ar released and showing no statistically significant slope.

Chapter 2 Figures and Tables

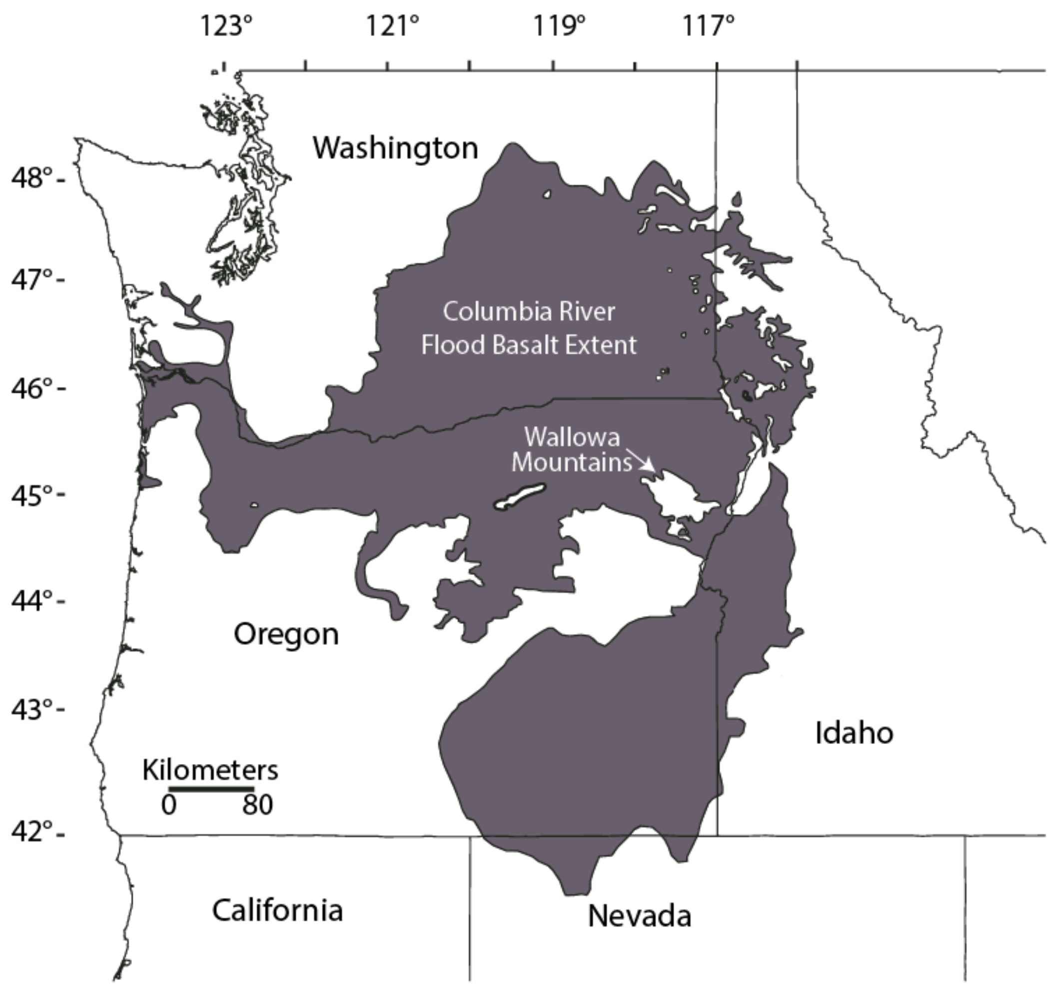

Figure 2.1– Map showing the spatial distribution of all Columbia River Flood Basalt formations (gray) across the Pacific Northwest. Wallowa Mountains are labeled and shown in white. Modified from Reidel et al. (2013).

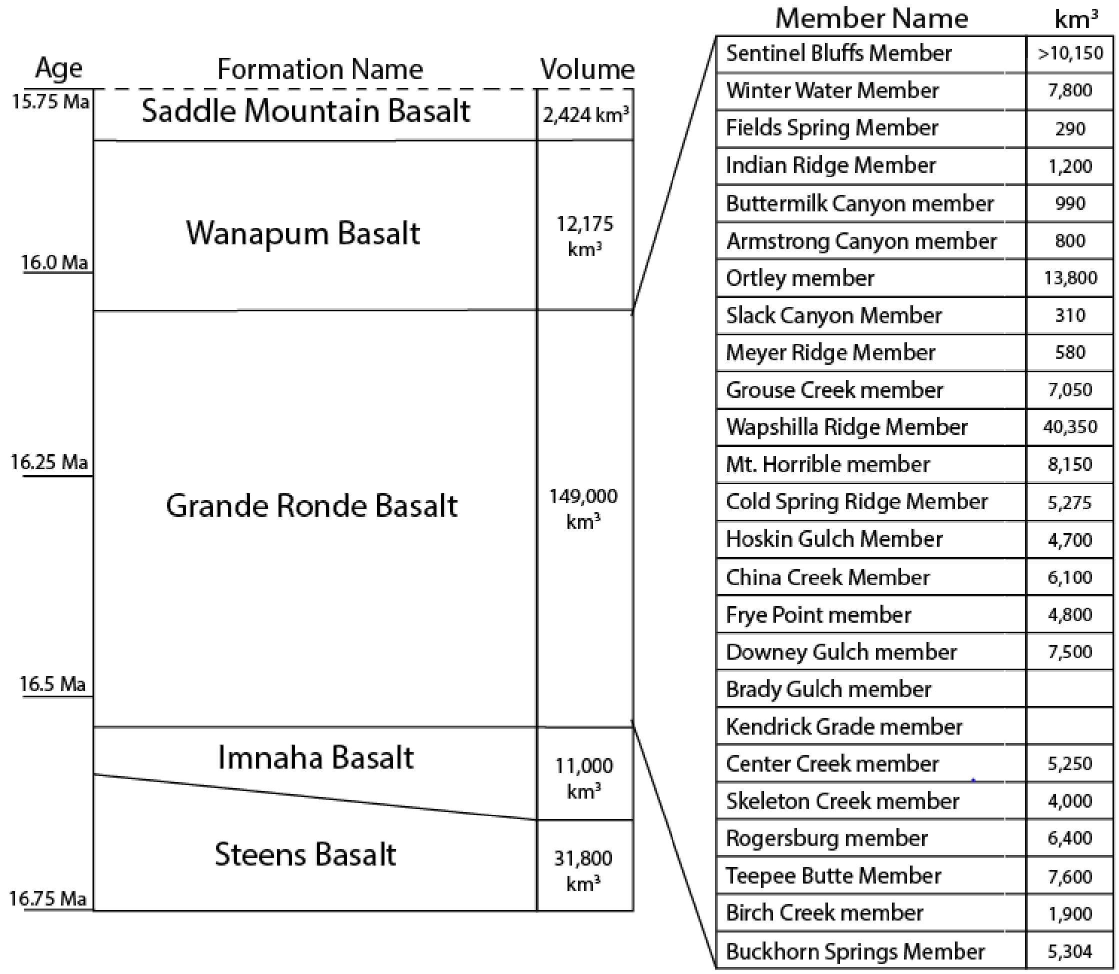

Figure 2.2– Chart showing the timing and volume of five of the seven Columbia River Flood Basalt formations (based on Kasbohm and Schoene, 2018). Pop out shows the volume of members within the Grande Ronde Formation (Reidel and Tolan, 2013).

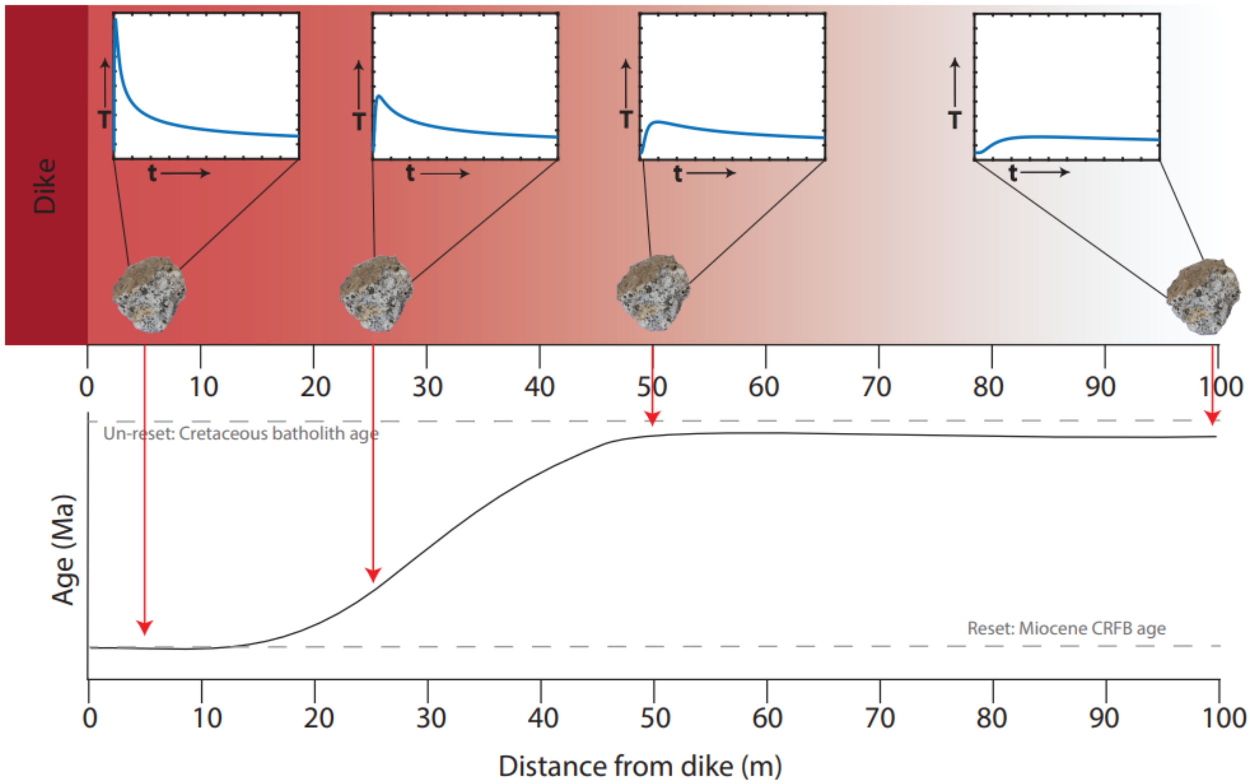

Figure 2.3– Expected thermochronologic ages (bottom) based on hypothetical, idealized thermal histories at different distances from a dike (top). Cooling ages are expected to be younger closer to the dike and older farther from the dike. This "resetting curve" reflects how samples closer to the dike experienced more net heating, and are therefore more reset, than samples farther from the dike.

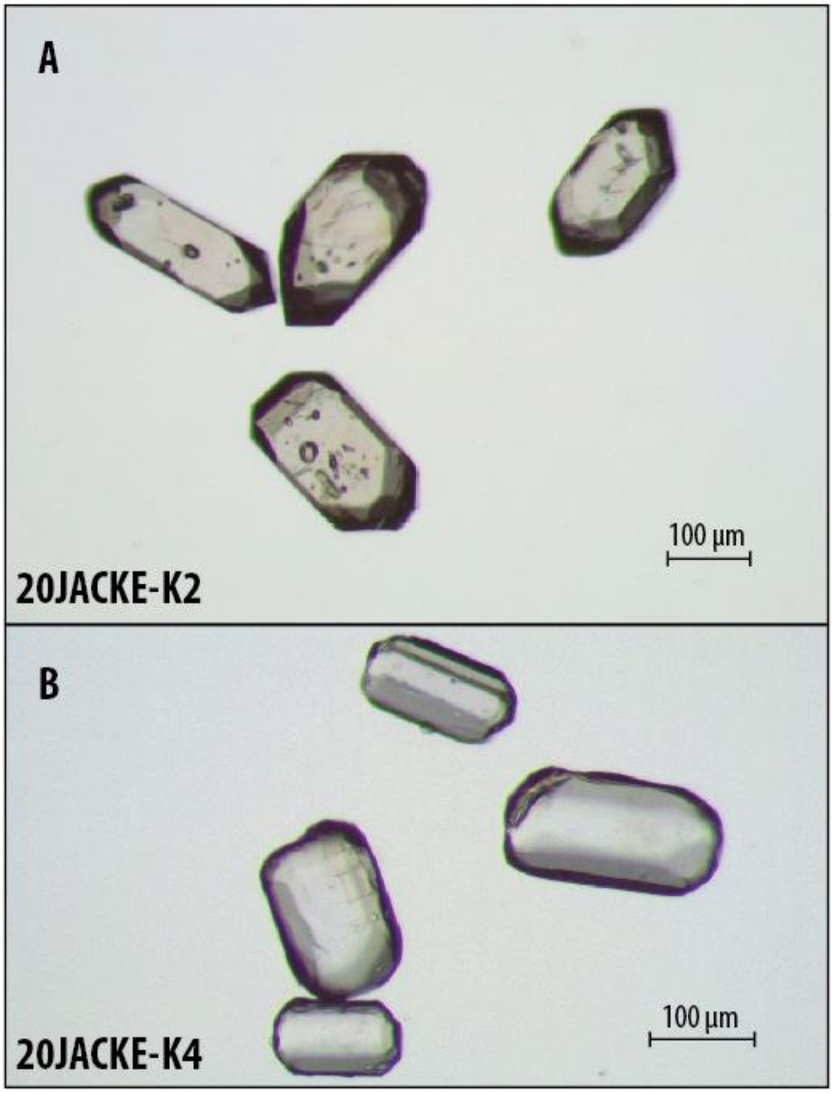

Figure 2.4– Representative zircon (A) and apatite (B) crystals picked for (U-Th)/He analysis. Samples from the Jackson E transect.

Table 2.1– Previous naming conventions for dike segments in the Maxwell Lake area compared to names used in this study. Latitude and longitude use WGS84 geographic coordinate system.

			Dike name in past literature			
Dike name (this study)	Latitude	Longitude	Petcovic and Grunder, 2003	Karlstrom et al., 2019	Bindeman et al., 2020	Biasi and Karsltrom, 2021
Jackson A	45.25087	-117.40854	NA	Maxwell Lake	Maxwell Lake	Jackson A
Jackson E	45.25332	-117.40685	NA	NA	NA	NA
Maxwell A	45.25783,	-117.40336	Maxwell Lake	NA	NA	Maxwell A

Table 2.2– List of all samples used in this study and their associated dike segments. Latitude and longitude use WGS84 geographic coordinate system.

Sample Name	Distance from dike (m)	Dike Name	Latitude	Longitude	Data from
2E1	2.0	Jackson A	45.250810	-117.408536	Karlstrom et al., 2019
2E2	5.0		45.250794	-117.408506	
2E3	11.0		45.250769	-117.408436	
2E4	21.0		45.250736	-117.408323	
2E5	30.0		45.250697	-117.408215	
2E6	40.0		45.250649	-117.408113	
2E7	53.5		45.250598	-117.407953	
2E8	72.5		45.250529	-117.407736	
2E9	100.0		45.250408	-117.407428	
20JACK-K1	215		45.250168	-117.405637	This study
20MAX-K1	3.1	Maxwell A	45.257842	-117.403415	
20MAX-K2	15		45.257873	-117.403559	
20MAX-K3	22.5		45.257889	-117.403650	
20JACKE-K1	2.70	Jackson E	45.253349	-117.406883	
20JACKE-K2	5.50		45.253376	-117.406905	
20JACKE-K3	16.9		45.253452	-117.407000	
20JACKE-K4	40		45.253607	-117.407195	
20JACKE-K5	100		45.254018	-117.407709	

Chapter 3: Jackson A Dike Segment and Intercalibration of Chronometers

3.1 Introduction

In this chapter, I expand the scope of Karlstrom et al. (2019) by introducing new thermochronologic tools with which to quantify magma flow through dikes. I add biotite $^{40}Ar/^{39}Ar$ (BtAr), zircon fission track (ZFT), and apatite fission-track (AFT) data to the existing apatite and zircon (U-Th)/He (AHe and ZHe) data next to the Jackson A dike segment (see Figure 3.1 and Table 2.1) in order to: (1) improve the analytical strategy by determining which chronometers most effectively measure key dike flow parameters, such as magma flow duration; and (2) perform an intercalibration test of four thermochronometers, which allows us to test how well laboratory observations of thermochronometer kinetics hold true in this natural setting. These goals prompt two main questions: (1) do high-temperature and low-temperature thermochronometers constrain different parts of a dike's thermal history? and (2) using published thermochronometer kinetics, can I find a single thermal history that explains multiple resetting patterns for each thermochronologic system simultaneously? To answer these questions and address these goals, I build upon the numerical model described in Karlstrom et al. (2019) to quantify key parameters (dike flow, background temperature, and thermochronometer kinetics) using observed thermochronologic ages next to the Jackson A dike segment.

The Jackson A dike segment is part of the 16.6-16.1 Ma Chief Joseph dike swarm (Figure 3.2), which fed the Grande Ronde and Imnaha eruptive phases and locally heated rocks of the Hurricane Divide pluton (130.2 ± 1.0 Ma; Žák et al., 2015) in the Wallowa batholith (Reidel and Tolan, 2013; Morriss et al., 2020). The Wallowa batholith was emplaced during the accretion of the Blue Mountain Province with North America between 140 and 120 Ma (Žák et al., 2015). Previous interpretations of thermochronologic data from the Wallowa batholith (Reiners, 2005;

Kahn et al., 2020; Schoettle-Greene et al., 2022) suggest that the Hurricane Divide pluton cooled to temperatures of <100 °C by ca. 100 Ma and then experienced cooling rates of 4-6 °C/Myr from ca. 100-88 Ma and cooling rates of 0.5-0.7 °C/Myr from ca. 88 Ma to present (Schoettle-Greene et al., 2022), where not impacted by the Chief Joseph dike swarm. The batholith's relatively simple Cretaceous-Recent cooling history, together with the contrasting age and composition between the Hurricane Divide pluton and the Chief Joseph dike swarm make the Wallowa Mountains an ideal natural setting for studying the effects of high-temperature, transient heating on low-temperature thermochronometers.

Previous research by Calk and Naeser (1973) used the natural setting of the Little Devil Postpile basaltic plug in the Sierra Nevada Mountains of California to document the resetting of AFT and sphene fission track thermochronometers in the surrounding granite wallrock. However, a subsequent attempt to intercalibrate low-temperature thermochronometers using natural data next to the Little Devil Postpile was stonewalled due to the uncertain, but apparently complex, subsurface geometry of the basaltic plug (Zeitler et al., 2020). The complexity there resulted in anomalous thermochronologic age patterns and was ultimately abandoned as the ages could not be modeled using simple 1-dimensional heat conduction. In contrast, the geometry of dike segments in the Chief Joseph dike swarm are relatively straight-forward: Reiners (2005) observed relatively well-behaved spatial patterns of AHe, ZHe, AFT, and ZFT ages next to a dike segment in the Cornucopia stock (116.8 ± 1.2; Johnson et al., 1997) of northeastern Oregon, and Karlstrom et al. (2019) have demonstrated that both AHe and ZHe ages follow the expected resetting trends next to the Jackson A dike segment, which I investigate in this study.

The Jackson A dike is exposed on the southwestern side of Jackson Lake in the Wallowa Mountains (Figure 3.1 and 3.3). This dike is ~9 m wide and strikes N20E with an undulating sub-vertical dip. Each margin of the Jackson A dike has partially melted granite wallrock of variable thickness (up to two meters in some places), suggesting that this dike was likely a long-lived conduit for a surface eruption (i.e., a feeder dike; Petcovic and Grunder, 2003; Morriss et al. 2020).

3.2 Background: A One-Dimensional Conductive Heating and Chemical Diffusion Model

Recently, Karlstrom et al. (2019) measured the thermal imprint of a potential feeder dike segment (called Jackson A dike segment in this study; see Table 2.1) using the spatial pattern of resetting in low-temperature thermochronometers next to the dike. Because thermochronometers are sensitive to both time and temperature, the amount of time that the dike was hot (actively transporting magma) is proportional to the width of the thermal footprint (Figure 3.4; see also section 2.2). Karlstrom et al. (2019) developed a new numerical method for systematically predicting how combinations of magma flow duration, ambient wallrock temperature, and wallrock thermal conductivity produce the observed spatial patterns of resetting. Using a Bayesian Markov-Chain Monte Carlo (MCMC) inversion of these parameters matched to the AHe and ZHe ages observed next to the Jackson A dike, they were able to constrain flow durations of 1-6 years (Karlstrom et al., 2019).

As part of their methods for inferring flow durations at the Jackson A dike segment, Karlstrom et al. (2019) developed a 1-dimensional conductive heating model coupled to a chemical diffusion model. The conductive heating code calculates the time-temperature history of the granitic wallrock at specified distances from the dike. Once generated, this time-temperature history is used to predict fractional resetting of the AHe and ZHe systems based on the chemical diffusion of ^{4}He from the crystal (equations 2.2, 2.3, and 2.4; Figure 3.3).

Running this model in a forward sense helps build intuition for how magma flow duration impacts AHe and ZHe resetting next to a dike; however, a robust quantitative estimate of a dike's active lifetime requires an inverse solution. To that end, Karlstrom et al. (2019) implemented a Bayesian MCMC inversion of the conductive heating and chemical diffusion models using AHe and ZHe data collected from a 100 meter transect next to the Jackson A dike segment.

This inversion could require exploration of up to 26 different variables, so Karlstrom et al. (2019) narrowed their focus to explore only six of the more sensitive parameters, assuming constant values for the others. The six parameters explored in that study are: activation energy kinetics (E_a) for the AHe and ZHe systems, which control the rate of ^{4}He diffusion; the thermal conductivity (k) of the wallrocks, which accounts for the rate of heat conduction in the granite (typically between 2-4 W/m°C; Dalla Santa et al., 2020); the background temperature (T_{BG}) of the wallrocks, which controls how much dike heating is needed to reset the chronometers; the active flow scale (τ_c), which scales the overall duration of magma flow through the dike assuming instantaneous shut-off; and the flow unsteadiness scale (τ_w), which parameterizes how quickly the temperature of the dike-wallrock boundary cools down towards the end of the dike's lifetime and allows the model to mimic, but not explicitly model, various dike processes that would impact heating, such as changes in flow rates as pressure gradients in the dike decrease over time (Bruce and Huppert, 1989, 1990). Finally, the total duration of active magma flow (τ_f) is derived from τ_c and τ_w using the equation (Karlstrom et al., 2019):

$$\tau_f = \tau_c + \frac{\tau_w \times \tanh^{-1}(0.98)}{10}. \quad (3.1)$$

This relationship between τ_c and τ_w is such that if the dike cools quickly (small τ_w) then τ_f will closely resemble τ_c (close to instantaneous magma shut-off); alternatively, if there is a monotonic decrease in flow (higher τ_w), then τ_f will be longer than τ_c. Ultimately, τ_f is the most important parameter for magma flow duration within the model and is, therefore, the parameter used to interpret eruption durations.

To fully explore these parameters, Karlstrom et al. (2019) ran 70-75 parallelized MCMC chains (MCMC Hammer; Anderson and Poland, 2016). Each chain started at a random point in parameter space and was made up of 2-4 x 10^4 iterations. As each chain works through a set number of iterations, the model selects for and pursues the smallest residuals, so it converges on a true posterior probability density function (PDF). The resulting PDF represents the highest likelihood solutions for the inverted parameters that produce predicted cooling ages that best fit the observed cooling ages. In this study, I broaden the application of the Karlstrom et al. (2019) method by testing whether adding more thermochronologic data produces model results that better resolve the history of CRFB dike emplacement.

3.3 Methods

3.3.1 Sampling Strategy

Samples used in this study are the same as those collected by Karlstrom et al. (2019) for apatite and zircon (U-Th)/He analysis, plus one new sample. They sampled a ~100 m lateral transect perpendicular to the contact of the Jackson A dike and the wallrock, with a focus on high-resolution sampling within 10 m of the dike (Figure 3.1). All of these samples were taken at approximately the same elevation along the transect. I collected one additional sample to supplement the transect collected by Karlstrom et al (2019). The purpose of this sample was to capture a non-reset age for the AHe system, which was not captured in the original 100 meter transect (Figure 3.1). As such, I sampled ~215 meters from the dike boundary, following the same sampling procedure as Karlstrom et al. (2019). Samples collected in 2016 by Karlstrom et al. (2019) were processed using standard methods by Zirchron, LLC, and the 2020 sample was processed at Idaho State University using the standard techniques outlined in Section 2.3.

The sampling strategy employed by Karlstrom et al. (2019) capitalized on the spatial relationship between the dike and the wallrock. In a simple dike-heating scenario, cooling ages should vary spatially based on both the magnitude of dike heating and the temperature sensitivity of the thermochronometer. Karlstrom et al.'s (2019) results demonstrate that at each distance along a transect away from a dike, the wallrocks experienced a distinct tT history that depends on the amount of heat supplied by the dike. Additionally, peak temperatures at each sample location are dependent on the how long magma actively flowed through the dike, with longer magma flow durations resulting in higher peak temperatures farther from the dike. Therefore, magma flow duration controls the extent of fractional resetting for all thermochronologic systems. In contrast, each different thermochronologic system within a single wallrock sample documents this heating, and therefore magma flow, as a function of its specific temperature sensitivity. So, although magma flow duration controls the overall spatial resetting pattern for each thermochronometer, lower-temperature thermochronometers can be fully reset (f = 100% and A_f = 16 Ma, in equation 2.4) farther from the dike, and higher-temperature thermochronometers can remain unreset (f = 0% and A_f > 100 Ma) much closer to the dike (e.g., ZHe vs. AHe in Karlstrom et al., 2019). Despite this spatial variability in reset ages between low and high temperature chronometers, each system documents the same dike emplacement history.

3.4 Thermochronologic Results

Each thermochronometer (AHe, ZHe, BtAr, AFT, and ZFT) has characteristic fully reset, partially reset, and non-reset age patterns moving away from Jackson A dike segment (Figure

3.5). Additionally, the width of resetting (i.e., the distance from the dike-wallrock contact to the closest non-reset age) for each chronometer varied as expected with the chronometers' temperature sensitivity. As such, BtAr had the narrowest resetting width (5 m) and AHe had the widest (215 m), with the other chronometers' resetting zones "nested" between them (Figure 3.5). A summary of the measured cooling ages next to the Jackson A dike can be found in Table 3.1, and detailed data tables for each thermochronometer can be found in the Appendix A.

As expected, the BtAr ages have the narrowest resetting width next to the Jackson A dike, with nine of the ten samples yielding mean ages that range from 121 ± 6.2 Ma to 127 ± 1.3 Ma (Table 3.1, Table A.5, and Table A.6), a few million years younger than the emplacement age of the Hurricane Divide pluton (Žák et al., 2015). The sample closest to the dike (two meters from the contact) yielded a mean BtAr age of 34 ± 6.8 Ma. This sample has a wide range of plateau ages from multiple step-heating experiments (26 ± 2.0 Ma to 49 ± 1.1Ma). The highly variable ages, which are all older than ca. 15 Ma, suggests that in this sample the BtAr system was only partially reset by heating during dike emplacement.

AFT pooled ages range from 15 +1.6/-1.7 Ma to 100 +5/-5.2Ma (Table 3.1, Table A.3). AFT ages are fully reset out to 53.5 meters from the dike, partially reset (58 +3.6/-3.4 Ma) at 72.5 m from the dike, and non-reset (95 +5.0/-4.8 Ma) at 100 m from the dike. In contrast, ZFT pooled ages range from 16 +1.9/-2.2 Ma to 121 +12.7/-14.1 Ma (Table 3.1, Table A.4). The ZFT ages are only fully reset to 16 +1.9/-2.2 Ma at two meters from the dike and reach a non-reset age of 121 +12.7/-14.1 at 40 meters from the dike. Between 5 and 30 m from the dike, ZFT ages are partially reset (47 +5.6/-5.0 Ma and 105 +12.5/-11.2 Ma).

Track-length distributions from AFT analyses (Figure 3.6) show a bimodal distribution in the partially reset sample 2E8. In radial plots, samples 2E8 and 2E9 also show a characteristic “open-jaw” pattern (Figure 3.7). This “open-jaw” pattern is commonly encountered in samples that resided in the AFT partial-annealing zone on geologic timescales (O’Sullivan and Parrish, 1995). Here, this trend is present in the wallrock samples that were partially reset by dike emplacement.

As a supplement to the AHe and ZHe ages generated in Karlstrom et al. (2019), I generated eight new single-crystal ages (215 m from the dike) for the AHe and ZHe systems for this study. Single-crystal AHe ages for this sample ranged between 80 ± 0.9 Ma and 92 ± 1.1 Ma (Table A.1), with an average of 86 ± 5.8 Ma (Table 3.1). Single-crystal ZHe ages ranged between 78 ± 1 Ma and 105 ± 1.4 Ma (Table A.2), with an average of 94 ± 12.2 Ma (Table 3.1).

3.5 Model Design

In order to use the Karlstrom et al. (2019) numerical model to interpret the new thermochronologic data, I modified their code. In particular, I added modules that calculate the diffusion of Ar in biotite crystals and the annealing of fission tracks in apatite crystals.

The new Ar diffusion code is a variation on the solution for volume diffusion that Karlstrom et al. (2019) used for the He systems. To model the diffusion of He in zircon and apatite crystals, they used a standard spherical model (Wolf et al., 1996). However, studies suggest (Giletti, 1974) that diffusion in the biotite Ar system is best modeled through an infinite cylinder (Reiners, 2009):

$$f = 1 - 4\sum_1^{\infty}(1/\alpha_n^2)\exp(-\alpha_n^2\tau), \quad (3.2)$$

where α_n are roots of $J_0(a\alpha_n) = 0$, and where $J_0(x)$ is the Bessel function of the first kind of order zero.

In contrast, fission-track annealing is a fundamentally different process than noble gas diffusion. As such, I developed a new module to calculate fission-track annealing and performed numerous benchmarking tests to ensure it was operating correctly. I based this code for annealing on the FTIndex code written by Richard Ketcham (described in Ehlers et al., 2005), and benchmarked the code to the program HeFTy (Ketcham, 2005).

3.5.1 Sensitivity Testing of the Fission-Track Annealing Model

To test the sensitivity and accuracy of the AFT annealing model compared to published models, I used synthetic time-temperature histories with a Gaussian-distributed heat pulse to compare fission-track ages predicted by the model to those predicted by the HeFTy program (Ketcham, 2005). I completed four tests using this method that varied (1) the maximum temperature reached by the heat pulse, (2) the duration of the heat pulse, (3) the date of the resetting event (A_r), and (4) the initial AFT age (A_i) while keeping A_r constant. I used kinetics from Ketcham et al. (1999) and a length reduction scale of 0.89 to calculate AFT ages. My model predicts AFT ages that are a few percent older than HeFTy's predicted ages (Figure 3.8). This small systematic offset may be the result of post-heating annealing (R. Ketcham, personal comm.), which HeFTy accounts for but this model does not. However, because the offset is within error of the AFT ages, I conclude that my fission-track annealing model is adequate for the purposes of this study.

3.5.2 Choosing Reset and Unreset Ages

Although each thermochronologic system requires a different equation to calculate fractional resetting, the final calculation of predicted age is the same (equation 2.4). However, equation 2.4 requires the selection of an initial age (A_i) and a reset age (A_r) in order to convert fractional resetting (a unitless value between 0 and 100%) to a predicted age (Ma) that can be compared to the observed ages. The observed ages reflect the integrated Cretaceous-Recent thermal history, as well as how the different temperature sensitivities of each thermochronologic system document that history, so the geologically appropriate A_i and A_r values may be different for each thermochronologic system. Therefore, I develop a method for choosing A_i and A_r using the cooling ages generated during this study, rather than using geochronologic ages of the Miocene Grande Ronde Formation and the Cretaceous Hurricane Divide pluton, as described below.

In dike-perpendicular sampling transects like the one in this study, A_r ages are close to the dike and are separated from the A_i ages by a zone of partially reset samples with ages between A_r and A_i. I set A_i for each thermochronologic system as the average of the oldest mean cooling ages for that system (i.e., farthest from the dike), and I set A_r as the average of the youngest mean cooling ages for all thermochronologic systems combined (i.e., all clearly reset samples closer to the dike; Figure 3.9; Table 3.2). My approach is different from the approach used in Karlstrom et al. (2019), where they assumed the same A_i for both the ZHe and AHe systems.

The unreset cooling ages from the Jackson A transect were unperturbed by Miocene CRFB-related heating but vary from ~125 Ma (high-temperature systems; see chapter 3.4) to ~86 Ma (low-temperature systems; see chapter 3.4) because they document the post-emplacement cooling of the Hurricane Divide pluton (130.2 ± 1.0 Ma; Žák et al., 2015; Schoettle-Greene et al., 2022). For example, biotite $^{40}Ar/^{39}Ar$ ages (closure temperature of ~350 °C for a 10°C/Myr cooling rate; Reiners and Brandon, 2006) are ~125 Ma, whereas AHe ages (closure temperature of 46-77°C for 1°C/Myr cooling rate; Flowers et al., 2009) across the Wallowa Mountains, even those far from dike intrusions, rarely exceed 100 Ma (Reiners, 2005; Kahn et al., 2020; Karlstrom et al., 2019; Schoettle-Greene et al., 2022). This age difference suggests that the batholith took a minimum of 30 Myr to cool below the AHe closure temperature after emplacement.

The fully reset cooling ages give approximately the same age as the dike (ca. 15-16 Ma; Reidel and Tolan, 2013) because the crystals lost all of their thermochronologic daughter products when the Jackson A dike was emplaced. In contrast to the unreset cooling ages, I observe no significant difference in the reset ages of the AHe, AFT, and ZHe ages in the sample(s) closest to the Jackson A dike segment (all reset cooling ages are between 14.6 ± 0.4 Ma and 16 ± 1.3 Ma). This is expected when rocks rapidly (<1 Ma) cool below thermochronometer closure temperatures and suggests that these samples rapidly cooled to below AHe partial-retention temperatures (<40 °C) after the CRFB eruptions. Here, I set A_r as 15 Ma for all systems, as this represents the average of all clearly reset cooling ages close to the dike.

3.5.3 Assigning Uncertainties to Input Data

In order to explore each parameter and converge on solutions that fit the data, the Karlstrom et al. (2019) model compares predicted ages to observed ages. This comparison results in a *residual*, which informs the model whether combinations of parameter values result in good or bad fits to the observed cooling ages. Low residuals reflect a good fit to the data, whereas high residuals indicate a bad fit to the data. In this study, I calculate residuals based on how close each predicted age is to each observed mean age. The residual calculations also take into account the uncertainties assigned to each mean age and penalizes predicted ages that are outside the bounds of those uncertainties. Therefore, it is important that the uncertainties assigned to each mean age reflect a geologically meaningful assessment of the data, which for low-temperature thermochronologic data is not always straightforward (e.g., Flowers et al., 2022).

Samples with Ar or He ages that are clearly fully reset or fully unreset have low observed intra-sample age variability (<15% standard deviation on the mean age), which is typical of samples with simple or rapid cooling histories (Flowers et al., 2022). Therefore, for these data inputs, I set ± error bars as 10% of the mean age, which represents common reproducibility for most noble gas thermochronologic systems (Flowers et al., 2022). These error bars are generally overestimates of the amount of single grain age dispersion observed in these fully and unreset samples so that the model does not unfairly penalize these data.

For Ar and He ages with significant intra-sample age variability (>15% standard deviation on the mean age, i.e., samples that are partially reset) using a simple standard deviation is not appropriate because the small number of observed single-crystal ages are likely not identically distributed around the mean (Flowers et al., 2022). Although such dispersed data are typical of partially reset samples—and likely arise because each crystal is a unique chronometer (Gautheron and Zeitler, 2020) with variable temperature sensitivities that manifest during partial resetting—there is no established approach for assigning uncertainties because it depends on the context and intention of doing so. Here, the goal is to permit the model to find good fits to (i.e., low residuals for) a conservatively wide range of predicted ages for the partially reset samples. Therefore, I set the ± error bars as the distance from mean age to the most dispersed age, which represents the range of single grain ages for each sample.

For the AFT data, I set ± error bars as 10% of the pooled age for samples that passed the chi-squared test (i.e., were either fully reset or fully unreset). Two samples (2E8 and 2E9) did not pass the chi-squared test, suggesting a higher level of age dispersion due to partial resetting. For these two samples, I used an uncertainty calculated using the random effects model (Galbraith and Laslett, 1993), which provides the range in which 95% of the population's ages should be found:

$$\pm AFT_{error} = A_c e^{\pm 2d}, (3.3)$$

where A_c is the central age (Ma) and d is age dispersion.

3.5.4 Modeling with Different Datasets

The two main questions addressed in this study require comparisons among models that use different thermochronologic systems. The first question investigates whether the temperature sensitivity of a chronometer affects how the model constrains key dike flow parameters, whereas the second question evaluates the model's ability to fit cooling ages from multiple thermochronologic systems at once (i.e., an intercalibration test of four thermochronometers). To resolve these two main questions, I designed three modeling "scenarios" that use different combinations of thermochronologic data.

To assess the influence of a chronometer's temperature sensitivity on the model results, I compare two model scenarios. In modeling scenario 1, I use only BtAr and ZHe cooling ages (i.e., higher-temperature chronometers; a total of 19 mean cooling ages). In modeling scenario 2, I use only AHe and AFT cooling ages (i.e., lower-temperature chronometers; a total of 20 mean cooling ages). I then compare the results of these two modeling scenarios using Bayesian and Akaike Information Criterion (BIC and AIC, respectively) to see if one of these scenarios provides a better fit to the observed data.

I use a third modeling scenario, Scenario 3, to test whether the model can fit the observed resetting patterns from four different chronometers at once. For this scenario, I use data from lower and higher temperature chronometers together (BtAr, ZHe, AHe, and AFT; a total of 39 mean cooling ages). I explore the full range of published kinetic values for each thermochronologic system in scenario 3 and attempt to reconcile a thermal history that jointly matches each dataset. If the scenario 3 model struggles to fit all four datasets at once, then the kinetics for these systems are not understood well enough to be used for this particular application.

Each modeling scenario explores parameter values related to kinetics (either parameterized activation energy– E_a, or resistance to fission-track annealing– r_{mr0}) for each thermochronologic system, thermal conductivity of the wallrocks (k), background temperature of the wallrocks (T_{BG}), and the two variables that describe magma flow through the dike (τ_c and τ_w; Table 3.3; see also section 3.2). Modeling scenario 1 explored 6 different parameters using 19 mean cooling ages, scenario 2 explored 6 different parameters using 20 mean cooling ages, and scenario 3 explored 8 different parameters using 39 mean cooling ages (Table 3.4). This combination of number of parameters and number of cooling ages for each scenario contributes directly to the AIC and BIC calculations used to evaluate these models.

3.5.5 Duration of the Modeled Time-Temperature History

A minimum simulation duration (i.e., the duration of the modeled time-temperature history in years) must be set for each modeling scenario. The total simulation duration varies as a function of the thermal diffusivity of the wallrock. I calculate thermal diffusivity as:

$$\alpha = \frac{k}{\rho C_p}, \quad (3.4)$$

where k is thermal conductivity, C_p is specific heat capacity, and ρ is density of the wallrock. Because k is one the parameters explored in the inversions, thermal diffusivity changes over every iteration in each model run and, by extension, total simulation duration also changes during each iteration. As such, it is important to ensure all values of *k* produce simulation durations that are above a minimum threshold.

Ideally, the simulation duration should include the time when magma was actively flowing through the dike, plus the time needed for the wallrocks to cool back down to background temperatures following the end of dike activity. If the simulation duration is not long enough for the dike's heat pulse to dissipate, then the predicted ages may be too old (i.e., not reset enough) compared to the observed ages. This problem may be exacerbated in the low-temperature systems, because these chronometers are more sensitive to residual temperature perturbations as the wallrocks return to their initial background temperature. However, longer durations substantially increase the computational time required for each inversion. Here, I walk through two tests used to set appropriate simulation durations for each model scenario.

To test the effect of different simulation durations on the predicted ages, I calculated both AHe and ZHe ages using a range of tT history durations (Figure 3.10). The predicted ZHe ages did not change significantly between the simulation durations tested (100-2000 years), reaffirming that the ZHe system is not affected by transient low-temperature heating. On the other hand, predicted AHe ages were significantly different among the simulation durations that were less than ~680 years. These sensitivity tests suggest that, when modeling low-temperature chronometers, the simulated tT history must be run for >680 years for the heat pulse to diffuse past the farthest sample location.

Although this first sensitivity test suggested that longer simulation durations are needed when modeling low-temperature chronometers compared to high-temperature chronometers, it was less clear what duration should be used when high and low temperature chronometers are modeled jointly. As such, I tested the effect of two different minimum simulation durations on the modeling results of a joint AHe and ZHe inversion. Both models consisted of 20,000 iterations and 24 chains, but one model ran simulations between 480-4,913 years, whereas the other model ran simulations between 998-10,009 years. A comparison of each model's probability density function (PDF) shows little difference between median total flow durations (Figure 3.11), suggesting that shorter simulation durations can be employed when high and low chronometers are jointly modeled.

Because longer simulation durations translate to increased computational time, I varied the simulation durations of each modeling scenario depending on its temperature sensitivity. Scenario 1 models ran for between 122.4 and 1,224 years, scenario 2 models ran for between 680 and 6800 years, and scenario 3 models ran for between 480 and 4,913 years. This range of simulation durations resulted in computational times between 3-10 days.

3.6 Modeling Results

Marginal posterior probability density functions (PDFs) for parameters explored in modeling scenarios 1, 2, and 3 are shown in Figures 3.12, 3.13, and 3.14, respectively. For each distribution, higher peaks correspond to values that the model spent the most time sampling because they fit the data well (i.e., results in low total residuals). Because the MCMC inversion preferentially samples values that give the lowest overall residuals, these peaks also highlight the highest likelihood solution for each parameter. In general, data sets for each scenario are well fit by the median best-fitting parameter values (Figures 3.15, 3.16, 3.17). Bivariate plots for each modeling scenario illustrate the inherent tradeoffs among certain parameters (Figures 3.18, 3.19, 3.20). Inversion results are summarized in Table 3.5.

3.6.1 Scenario 1: Modeling with High-Temperature Chronometers

For the high-temperature inversion, I used the model to fit just BtAr and ZHe ages. I ran 25,000-30,000 iterations per chain for 72 chains and burned 10% of iterations per chain for a total of 1.7 x 10^6 iterations.

Modeling of both high-temperature thermochronometers (BtAr and ZHe) suggests a total flow duration between 2.2 and 7.6 years, with a median best fit of 4.2 years (Figure 3.12A). 68% of solutions for flow unsteadiness (τ_w) fall between 0.14 and 7.3 years, but the median τ_w is 0.98 years, suggesting that unsteady flow conditions are not favored (Figure 3.12C). Background temperature was not well-constrained, with 68% of solutions falling between 30.9 and 78.6 °C, with a median value of 49.6 °C (Figure 3.12D). The lack of a clearly unimodal distribution for background temperature suggests that a wide range of background temperatures are supported by the high-temperature thermochronologic data. Similarly, thermal conductivity also has a monotonically sloped PDF and a 68% confidence interval of 1.5 - 7.6 W/mC, with a median value of 3.4 W/mC, suggesting that the model favors smaller values for *k* (Figure 3.12G). The scenario 1 model result provided no constraints on values for both BtAr and ZHe activation energy (Figure 3.12E and 3.12D). The median best-fit values for each parameter predicted ages that generally fit the observed BtAr and ZHe ages; however, predicted BtAr and ZHe ages are younger than observed ages 5 m from the dike and older than observed ages 20.5 m from the dike (Figure 3.15).

3.6.2 Scenario 2: Modeling with Low-Temperature Chronometers

For the low-temperature inversion, I used the model to fit just AFT and AHe ages. I ran 25,000 iterations per chain for 72 chains and burned 10% of iterations per chain for a total of 1.62 x 10^6 iterations.

Model results for total flow duration were between 3.8 and 11.3 years with a median of 6.3 years (Figure 3.13A). 68% of solutions for flow unsteadiness (τ_w) fall between 0.13 and 15.8 years, but the median τ_w is 1.3 years (Figure 3.13C). The model favored solutions between 29.3 and 59.4 °C for background temperature with a median solution of 40.4 °C (Figure 3.13D). The PDF for background temperature favors lower-temperature values; however, the PDF lacks a clearly peaked distribution, which suggests that background temperature was not well constrained by this model. The PDF for fission-track resistance to annealing (r_{mr0}) has a broad peak between 0.818 and .867, with a median of 0.842 (Figure 3.13E). AHe activation energy and rock thermal conductivity were not well constrained by the model result (Figure 3.13F and 3.13G). The median best-fit values for each parameter provide an excellent fit to both the AHe and AFT datasets, as all predicted ages are within error of the observed AHe and AFT ages (Figure 3.16).

3.6.3 Scenario 3: Modeling with All Chronometers

The all-chronometer inversion attempted to fit input data from four thermochronologic systems, AHe, ZHe, BtAr, and AFT, at once. I ran between 23,000-27,000 iterations per chain for 72 chains and burned 10% of iterations per chain for a total of 1.6 x 10^6 iterations.

Joint modeling of all four thermochronologic systems suggests a total magma flow duration of between 2.9-8 years, with a median best fit of 5.5 years (Figure 3.14A). The shape of the total flow duration (τ_f) PDF is bimodal, suggesting that more than one value for τ_f can fit the observed thermochronologic data. The range of τ_w preferred in this inversion result (68% confidence interval: 0.14 -13.2 years) supports the possibility of unsteady flow over the dike's lifetime; however, the median value of 1 year suggests that the emplacement is best described as overall steady flow (Figure 3.14C). Background temperatures were constrained between 62.4 and

75.8 °C, with a median of 69.9 °C (Figure 3.14F). The 68% confidence interval for thermal conductivity is between 1.3 and 7.7 W/mC, but the model favored solutions with lower values of k (median: 2.3 W/mC; Figure 3.14E). Although all activation energies explored for AHe, ZHe, and BtAr produced equally good fits (i.e., PDFs for these parameters are not peaked; Figures 3.14G, 3.14H, and 3.14I), the kinetic parameter for AFT did show preference to certain solutions. In particular, r_{mr0} for AFT is between 0.85 and 0.88, with a median best fit of 0.87 (Figure 3.14D).

The median best-fit values for each parameter provide generally good fits to all four datasets (Figure 3.17). AFT ages predicted by the model are within error of all observed AFT ages. As in scenario 1, predicted ages deviate from the observed ZHe and BtAr ages most significantly close to the dike; however, the predicted ages deviate from the observed AHe ages only at the sample 215 m from the dike.

3.7 Discussion

3.7.1 Model Comparison

One of the main goals of this study is to determine which thermochronometers (or combination of thermochronometers) most effectively measures key dike flow parameters, such as magma flow duration, in order to further establish thermochronology as a tool for studying timescales of dike emplacement. In general, each modeling scenario independently supports a similar magma flow duration for the Jackson A dike segment; median values for each modeling scenario's magma flow duration are within the 68% confidence intervals of the other modeling scenarios (Figure 3.21). Additionally, each model's median total flow duration is within the 95% confidence interval (1-10 years) reported by Karlstrom et al. (2019) for this same dike.

Although there is general consistency across these modeling approaches, each scenario produced slightly different solutions for each parameter. The model predicted relatively long flow durations (median: 5.5 years; Figure 3.14A) and warmer background temperatures (median: 69.9 °C; Figure 3.14F) when jointly modeling all chronometers at once (scenario 3), whereas joint modeling of the high-temperature chronometers (scenario 1) yielded the shortest predicted flow durations (median: 4.2 years; Figure 3.12A) and colder background temperatures (median: 49.6 °C; Figure 3.12D). In contrast, models using only low-temperature chronometers (scenario 2) predicted the longest flow durations (median: 6.3 years; Figure 3.13A), but also the coldest background temperatures (median: 40.4 °C; Figure 3.13D)

In order to further compare these model results, I employ both Akaike and Bayesian Information Criteria (AIC and BIC, respectively). Because each model uses a different amount of data and explores a different number of parameters, I cannot compare residuals directly between models (i.e., models that are trying to fit more data will, as a consequence, have higher total residuals). Here, I calculate AIC and BIC using equations 3.4 and 3.5 (Akaike, 1974; Schwarz, 1978):

$$AIC = -2 \ln L(\theta) + 2p, \quad (3.4)$$

and

$$BIC = -2 \ln L(\theta) + p \ln n, \quad (3.5)$$

where $L(\theta)$ is the maximum likelihood function, p is the number of parameters, and n is the number of data points (i.e., cooling ages). For the natural log of the likelihood function, I use the total residual associated with the median best fitting values for each parameter. AIC takes into account that each model may use different numbers of parameters, and provides a more consistent tool for comparing maximum likelihood between two models. In contrast, BIC acknowledges different amounts of data, as well as different numbers of parameters between models. Small values for both AIC and BIC indicate the best fitting model, whereas larger values for AIC and BIC suggest less effective models.

Based on these model selection techniques, scenario 2 (low-temperature chronometers) is the most effective model for inferring dike emplacement parameters, as it had the lowest value for both AIC and BIC between the three scenarios (34.3 and 40.3, respectively). In contrast, scenario 1 (high-temperature chronometers) had an AIC of 84.7 and a BIC of 90.4 and scenario 3 (all chronometers) had an AIC of 149.2 and a BIC of 162.4.

3.7.2 Scenario 3 Intercalibration Test

The second goal of this study was to use this large thermochronologic dataset from the Jackson A dike segment to perform an intercalibration test of four thermochronometers. Results from this intercalibration test demonstrate that key dike parameters, and therefore a distinct thermal history, can be resolved when modeling cooling ages from multiple chronometers at once. This is supported by the relatively narrow 68% confidence intervals and unimodal peaks shown in the scenario 3 PDFs (Figure 3.14A and 3.14F). If the model struggled to fit cooling ages from all four chronometers, a possible outcome would be relatively unconstrained PDFs (i.e., flat profile) for each parameter, as all parameter values might produce similar, and not necessarily good, fits to the data.

Using the median value for each parameter's PDF as a best-fit thermal history solution, I can assess how well the model's predicted cooling ages match the observed cooling ages for each thermochronologic system (Figure 3.17). The total residual error across all four thermochronologic systems is 15.2, which is significantly less than the total residual error reported by Karlstrom et al. (2019; 42.7 total residual), despite including residuals for two additional chronometers.

However, even though the MCMC inversion was able to fit ages from all four thermochronologic systems relatively well within the framework of the model, there are still some misfits between the cooling ages predicted by the model and the observed cooling ages. In particular, the observed ZHe age pattern has a wider partially reset zone (25 m) than the age pattern predicted by the model (9.5 m; Figure 3.17). Additionally, the far-field AHe age observed at 215 m is older than the age predicted by the model. These model misfits may arise from the oversimplified conductive heat transfer mechanism used in the model. For example, although there is evidence for an ancient hydrothermal system in the wallrock surrounding this dike (Bindeman et al., 2020), the Karlstrom et al. (2019) approach does not incorporate an advective heat transfer mechanism. Additionally, I do not explicitly model complex thermal histories that would arise from multiple magma injection events, or a changing location of the dike boundary during emplacement (although both processes are mimicked, in some ways, by the flow unsteadiness parameter, τ_w). If these complex processes were operating during emplacement of the Jackson A dike segment, they might explain the model's misfits of the observed ZHe ages close to the dike and/or misfits of the observed AHe ages far from the dike. However, the thermochronologic results reported here do not require these complexities. Additionally, the Karlstrom et al. (2019) approach produces clearly robust model results, so adding additional model complexity is not necessary to answer the questions I am interested in.

Another potential source of misfit between the ages predicted by the model and the ages observed next to the Jackson A dike could be the pre-CRFB cooling history of the Hurricane Divide pluton. In particular, the presence of non-uniform distribution of He in these apatite and zircon crystals (Shuster and Farley, 2004) could result in complicated predicted vs. observed age relationships in partially reset samples. However, although both of the misfit ZHe ages are considered partially reset, the development of a He concentration gradient can only explain one of the misfit samples. If these samples developed a He concentration gradient (i.e., higher concentration at the core and lower concentration at the rim), dike heating would result in minimal He loss because He is preferentially lost from the edges of the diffusion domain. In contrast, the model used here, which assumes a uniform distribution of He within the crystal, would predicted more He loss and, therefore, a younger age. Although the ZHe age 5 m from the dike follows this expected pattern, the ZHe age 20.5 m from the dike is younger than the age predicted by the model and, therefore, does not follow this pattern.

In modeling scenario 3, the model explores a wide range of activation energies for ZHe, AHe, and BtAr because these systems have variable kinetics in nature. The model did not resolve a best fit to the activation energy parameters for any of the chronometers, which suggests that the range of values explored produce equally good fits to the data (Figures 3.14G, 3.14H, and 3.14I). In contrast, the model did resolve a best fitting value for the AFT kinetic parameter (resistance to fission-track annealing or r_{mr0}; Figure 3.14D). A range of r_{mr0} values was explored to account for natural variations in other empirically fitted kinetic constants in the fission-track systems; as such, I do not interpret the best fitting r_{mr0} value (median: 0.87) as the true resistance to annealing for the AFT system sampled. This r_{mr0} value is higher than the r_{mr0} expected for a "typical" apatite crystal (usually 0.83-0.84; R. Ketcham, personal comm.).

3.7.3 Eruption Durations and Eruptive Rates for the Jackson A Dike Segment

The Jackson A dike segment has been correlated geochemically with the Meyer Ridge member of the Grande Ronde eruptive phase of the CRFBs based on a supervised machine learning classification model of the stratigraphy and the measured magnetic polarity of the dike segments (Rachel Hampton, in prep; Biasi and Karlstrom, 2021). This member is made up of 2-4 flows and approximately 620 km^3 of basalt, suggesting individual flow volumes between 155-310 km^3. Based on my inversion results from all three modeling scenarios, I constrain total duration of magma flow through the Jackson A dike segment to between 2.2-8 years. If the Jackson A dike segment fed one individual flow from the Meyer Ridge member, the average flow rate would be between 0.05-0.39 km^3/day. The low-end of this calculated rate is comparable to the average eruption rate of the second largest basaltic eruption documented in human history: the 1783 Laki eruption in Iceland, which erupted 14.7 km^3 of basalt at a rate of 0.06 km^3/day over a period of 8 months (Thordarson and Self, 2003; Thordarson and Larsen, 2007).

Firsthand accounts of the environmental impact of the 1783 Laki eruption (summarized in Thordarson and Self, 2003) and the geochemistry of Icelandic lavas (Thorsdarson et al., 1996) can be used to better understand how CRFB eruptions may have impacted the Miocene climate and biosphere. In particular, over the span of 8 months, the Laki eruption contributed ~122 megatons of SO_2 to the atmosphere, which led to months of volcanic pollution and acid rain over the Northern Hemisphere and more than a year of extreme weather (Thordarson and Self, 2003). Previous research on sulfur content in glass inclusions show similar pre-eruptive compositions between the Roza member (CRFB) and Laki eruption, with 1965 ± 110 ppm (Thordarson and Self, 1996) and 1677 ± 225 ppm (Thordarson et al., 1996), respectively. Additionally, the eruption of the Roza member (~1,300 km^3) is estimated to have released ~12 Gt of SO_2 over its ~10-year eruption duration (Thordarson and Self, 1996). Based on the similar sulfur concentrations for the Laki and CRFB magmas, the Jackson A feeder dike could have easily produced >1Gt SO_2 over its 2.2-8 year lifespan. I expect that such a large release of sulfur aerosols would have triggered severe weather anomalies, similar to those observed during and after the Laki eruption, that lasted at least the duration of the eruption and possibly 2-3 years longer (Self et al., 2005; Bond and Wignall, 2014).

In addition to elucidating the environmental impacts of one eruptive member, the eruptive rate calculated for the Meyer Ridge member in this study can also be used to better understand the eruptive tempo of the main eruptive phase of the CRFBs. Previous geochronology from Kasbohm and Schoene (2018) suggested that Grande Ronde members within the R2 magnetostratigraphic unit (Mount Horrible, Wapshilla Ridge, Grouse Creek, and Meyer Ridge) erupted over a span of 160,000 years. These four members contain a combined total of ~31 lava flows. If each of these flows were fed by a dike that was active for 2.2-8 years, then the average periodicity for the R2 magnetostratigraphic unit would be 645-2,346 years between individual flows, with only 65-250 years total eruptive time. However, these estimates represent average eruptive hiatuses, and it is more likely that the hiatuses between these eruptions were irregular throughout the eruption of the Grande Ronde members.

3.8 Conclusions

Building on the numerical modeling approach of Karlstrom et al. (2019), I used zircon and apatite (U-Th)/He (ZHe and AHe), biotite $^{40}Ar/^{39}Ar$ (BtAr), and apatite fission track (AFT) cooling ages in the wallrock next to the Jackson A dike segment to quantify how long magma flowed through the Jackson A dike segment. The goals of this chapter were to (1) determine which chronometers most effectively measure key dike flow parameters, such as magma flow duration, and (2) perform an intercalibration test of multiple thermochronometers, in order to determine whether or not laboratory observations of chronometer kinetics hold true in nature. To address these goals, I compared three different scenarios for modeling cooling ages next to the Jackson A dike segment using different combinations of datasets: ZHe and BtAr (scenario 1, high-temperature chronometers), AHe and AFT (scenario 2, low-temperature chronometers), and ZHe, BtAr, AHe, and AFT (scenario 3, all chronometers).

Based on Akaike and Bayesian Information Criteria, scenario 2 was the best modeling scenario that was explored. This suggests that low-temperature thermochronometers (AHe and AFT) are more effective than high-temperature thermochronometers (ZHe and BtAr) at constraining dike flow parameters. Both scenario 1 and 2 were unable to provide clear constraints on background temperature, activation energy, and thermal conductivity (Figures 3.12 and 3.13); however, scenario 3 was able to constrain background temperature (Figure 3.14), which suggests that this numerical method requires cooling ages from both high-temperature and low-temperature thermochronometers to resolve background temperatures during dike emplacement.

In modeling scenario 3, the AHe, ZHe, BtAr, and AFT systems were intercalibrated using the range of kinetics accepted by the thermochronology community. The numerical model was able to reproduce cooling ages from all four systems simultaneously with minimal misfit (total residual 15.2). Activation energy was not constrained for either the AHe, ZHe, or BtAr systems, which means that any of the values within the prior distribution for activation energy provide acceptable fits to the cooling ages observed in these systems. The modeling results did, however, constrain the AFT kinetic parameter, resistance to annealing (r_{mr0}), which suggests that the empirically derived kinetic constants assumed in the annealing model (Ketcham et al., 1999) may not reflect the kinetics of the apatite population used in this study.

To better constrain the kinetics of these systems, future work could assume constant values for magma flow, background temperature, and thermal conductivity parameters (using the median value predicted by previous modeling) and focus instead on exploring parameters related to activation energy, diffusivity, and resistance to fission-track annealing instead. Reducing the number of parameters explored by the model would place more pressure on the model to resolve acceptable kinetic values that fit the observed ages for each system.

Finally, modeling results from this study were able to reproduce total magma flow durations of the same magnitude as those predicted by Karlstrom et al. (2019), and within overlapping confidence intervals (Figure 3.21). These findings suggests that any combination of thermochronometers can be used to model magma flow duration next to a dike, regardless of temperature sensitivity. Additionally, because median best-fitting results from each modeling scenario independently support a similar magma flow duration, the 2.2-8 year magma flow duration suggested in this study represents a robust estimate of magma flow through the Jackson A dike and is supported by previous estimates of magma flow (Karlstrom et al., 2019; Biasi and Karlstrom, 2021)

Chapter 3 Figures and Tables

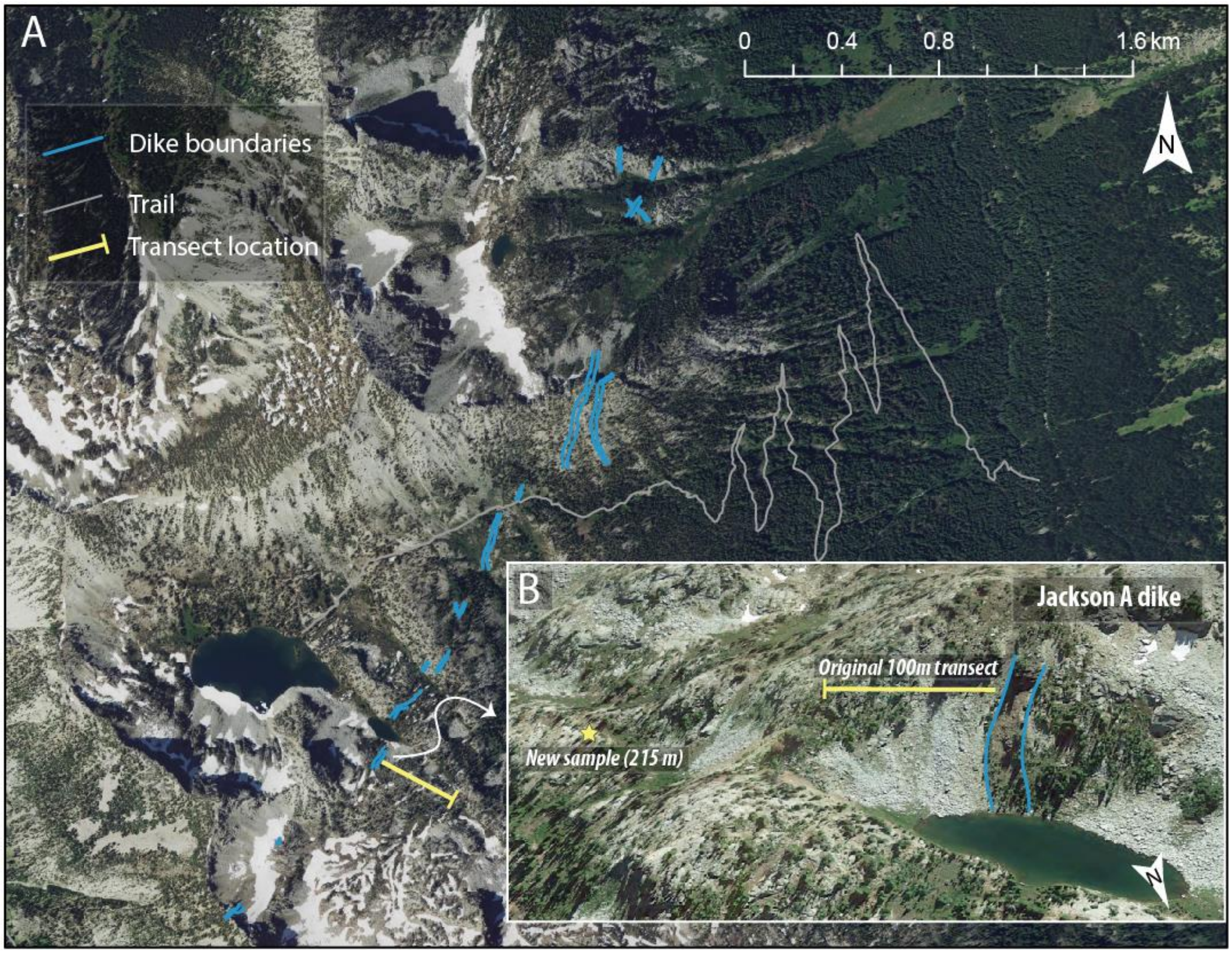

Figure 3.1– (A) Map of the Maxwell Lake Dike complex, after Hampton (in prep). (B) Annotated Google Earth image of the Jackson A dike segment. The original 100 m transect was collected by Karlstrom et al. (2019) and the new sample at 215 m was collected for this study in 2020.

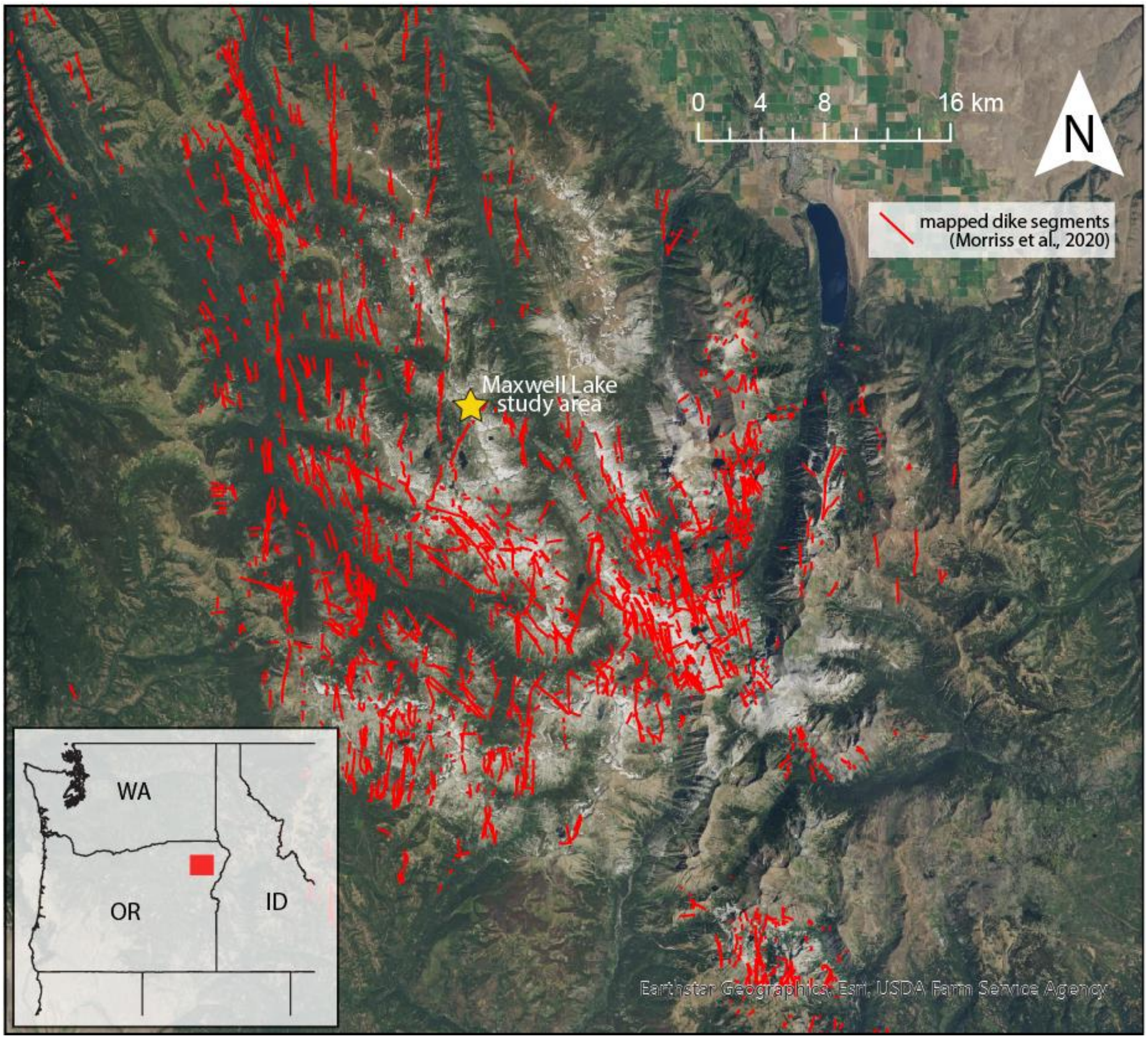

Figure 3.2– Map of Chief Joseph dike swarm. Star shows location of the Maxwell Lake study area. Dikes digitized by Morriss et al. (2020).

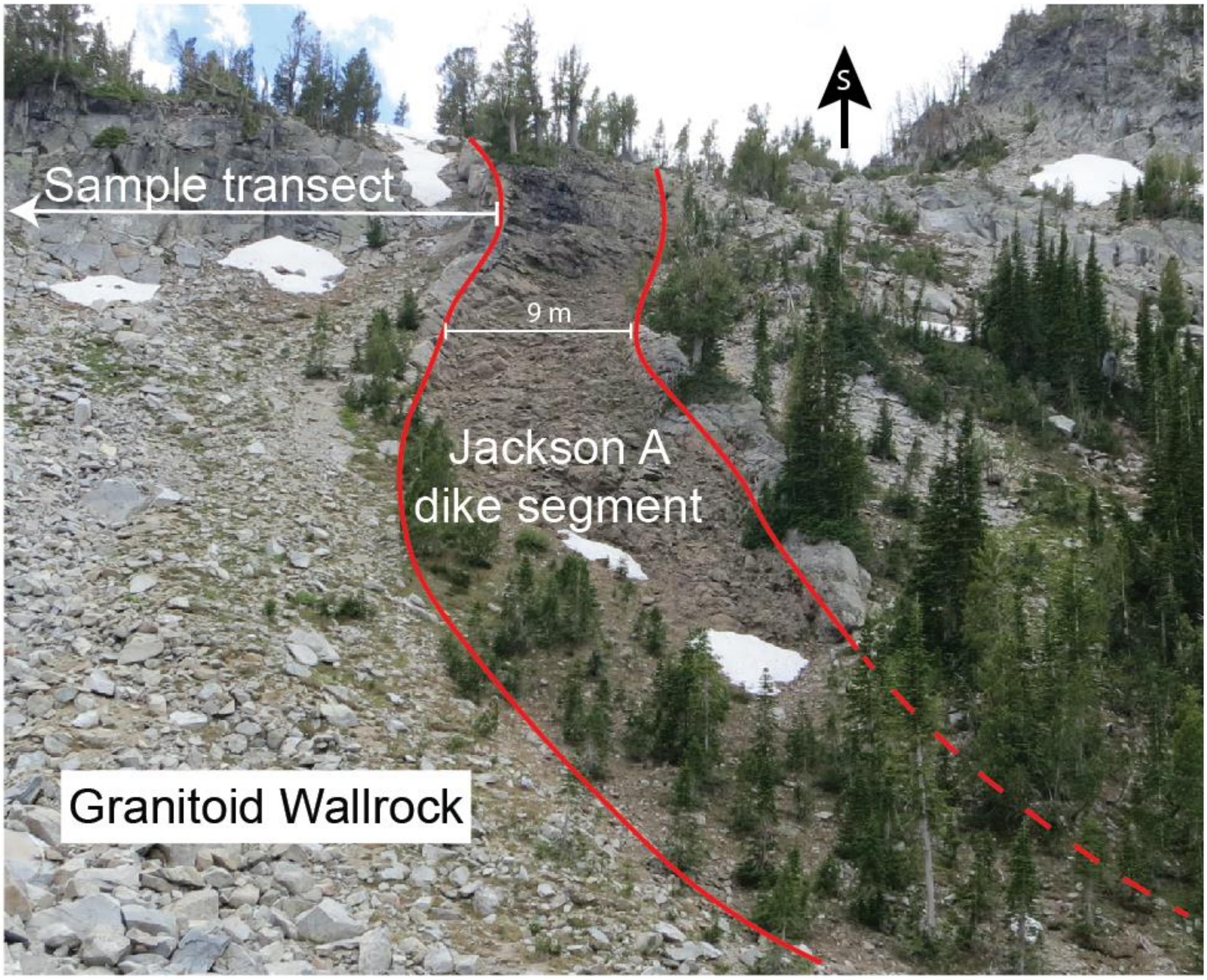

Figure 3.3– Annotated view of the dike/wallrock contact and sampling transect at the Jackson A dike segment.

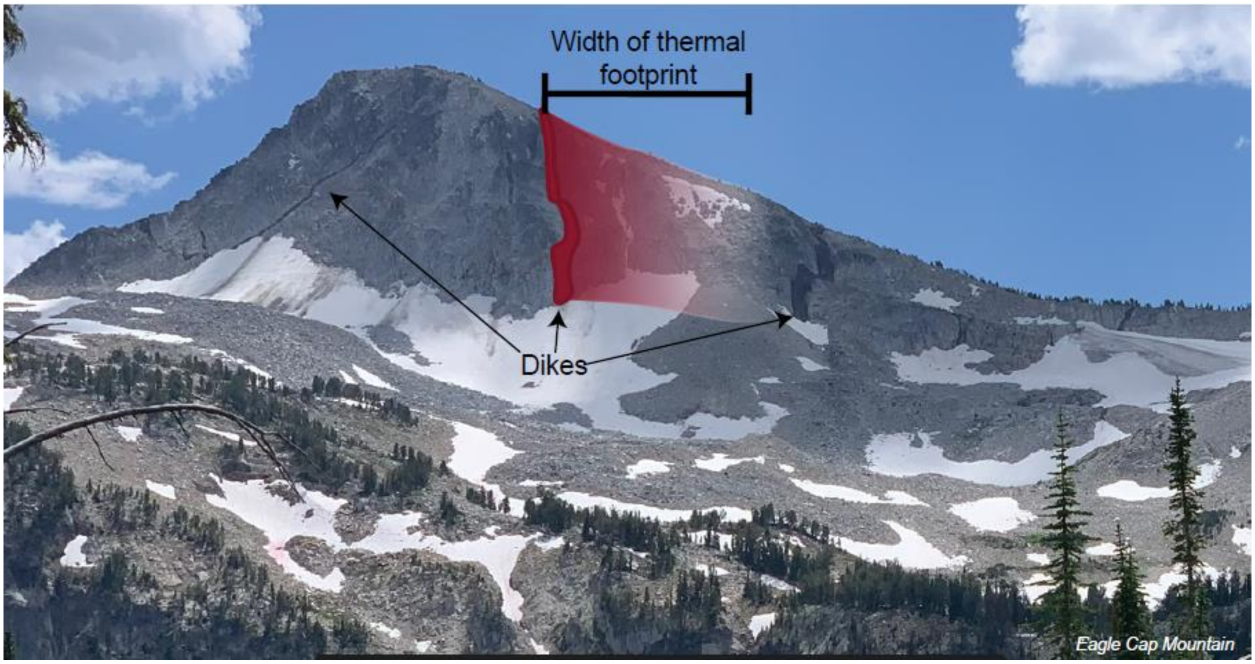

Figure 3.4– Schematic representation of a dike's thermal footprint. Width of thermal footprint is proportional to the duration of magma flow through the dike.

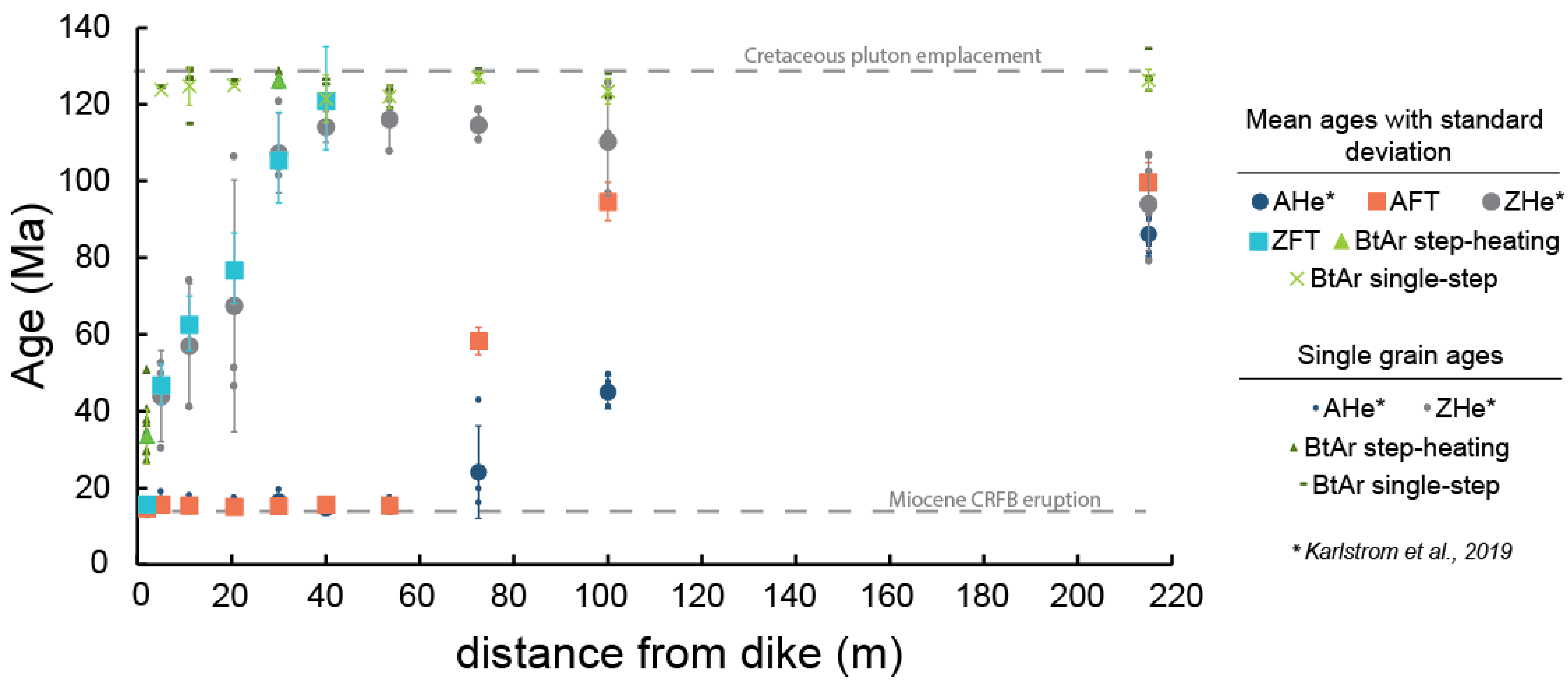

Figure 3.5– Mean and single grain ages for Jackson A dike thermochronology transect. AFT and ZFT data are pooled ages with 95% confidence intervals. Age of Cretaceous batholith emplacement is the age of the Hurricane Divide pluton (130.2 ± 1.0 Ma; Žák et al., 2015), and the age of Miocene CRFB eruption is ~16 Ma (Reidel et al., 2013).

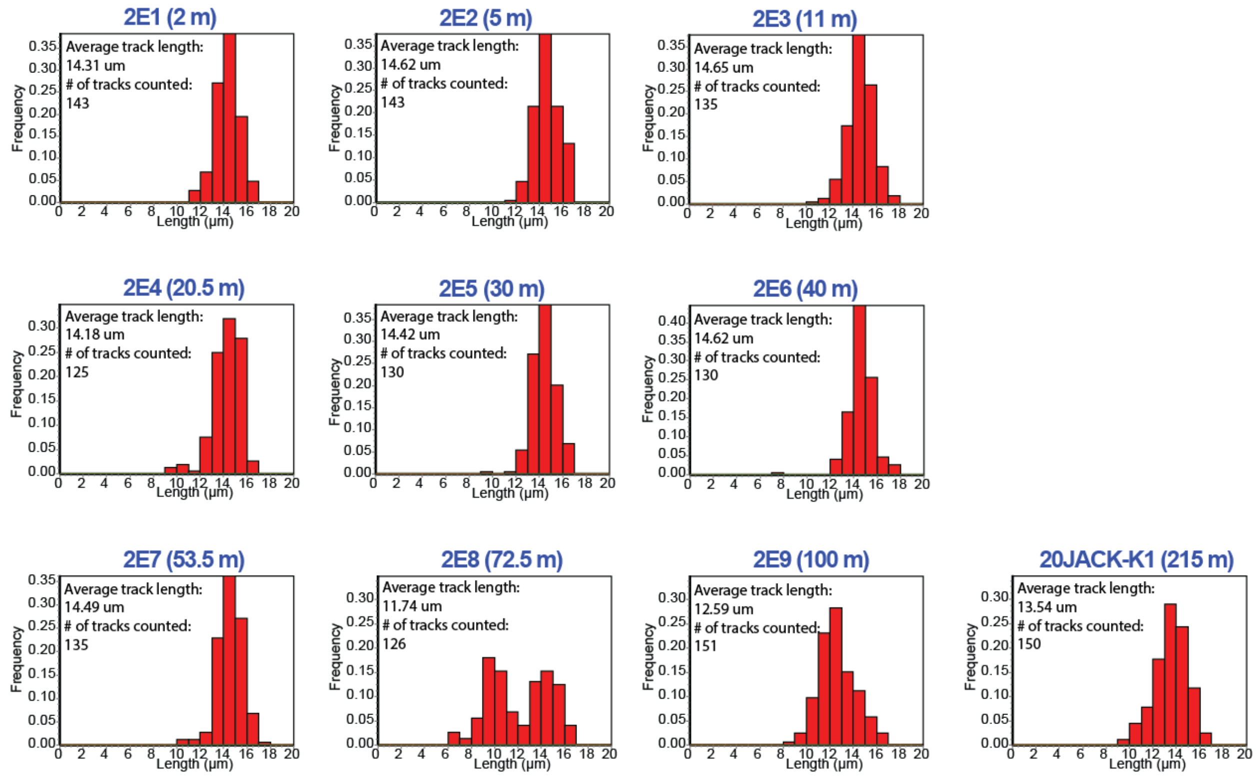

Figure 3.6– Apatite fission track length distributions from Jackson A dike transect samples. Samples 2E1-2E7 show fully reset ages, 2E8 is partially reset, and 2E9-2E10 are non-reset. Note the bimodal distribution of track lengths in 2E8.

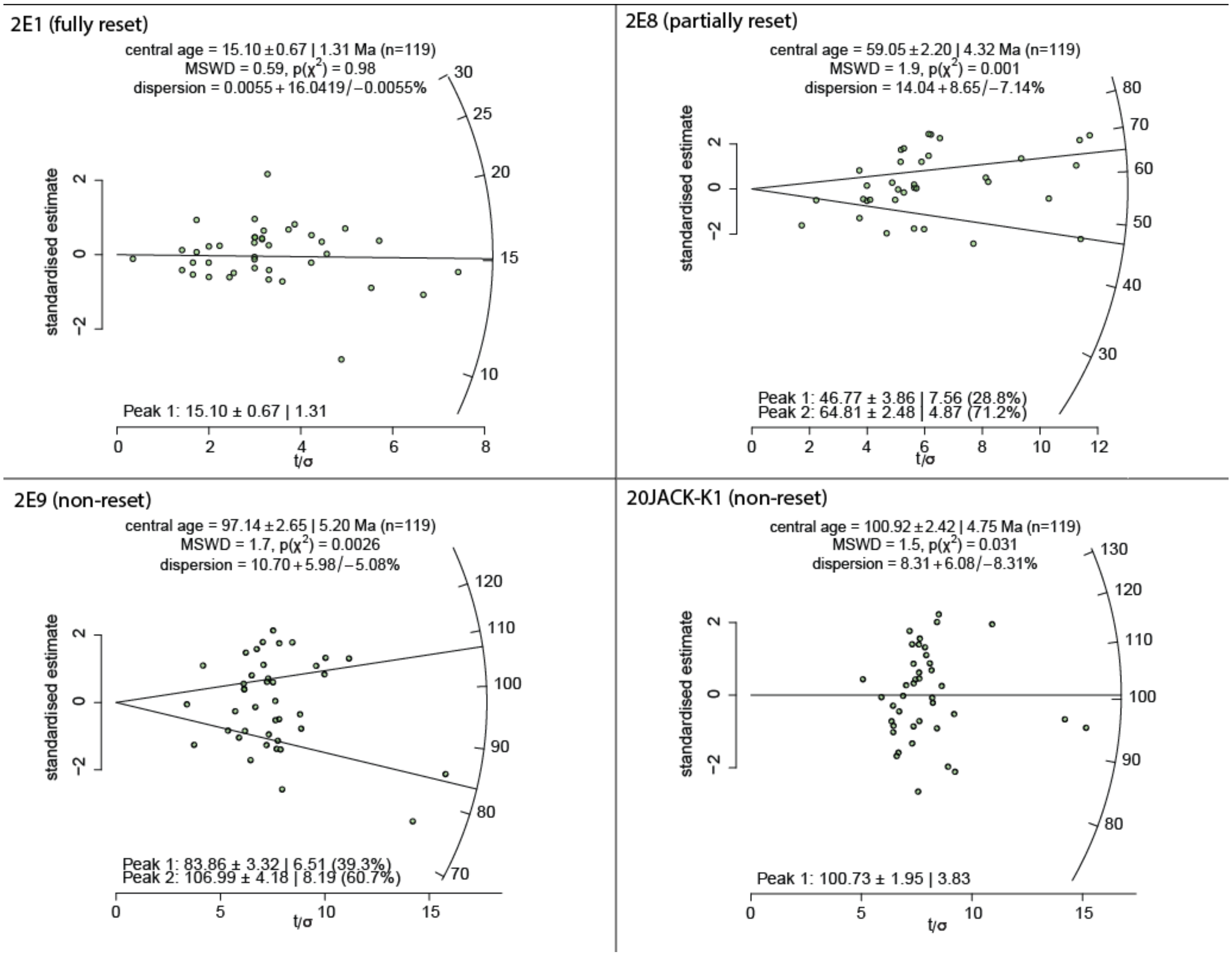

Figure 3.7– Apatite fission track radial plots for four samples in the Jackson A dike transect. Samples chosen to show “open jaw” behavior of samples 2E8 and 2E9 in comparison to other samples in the transect (flat line).

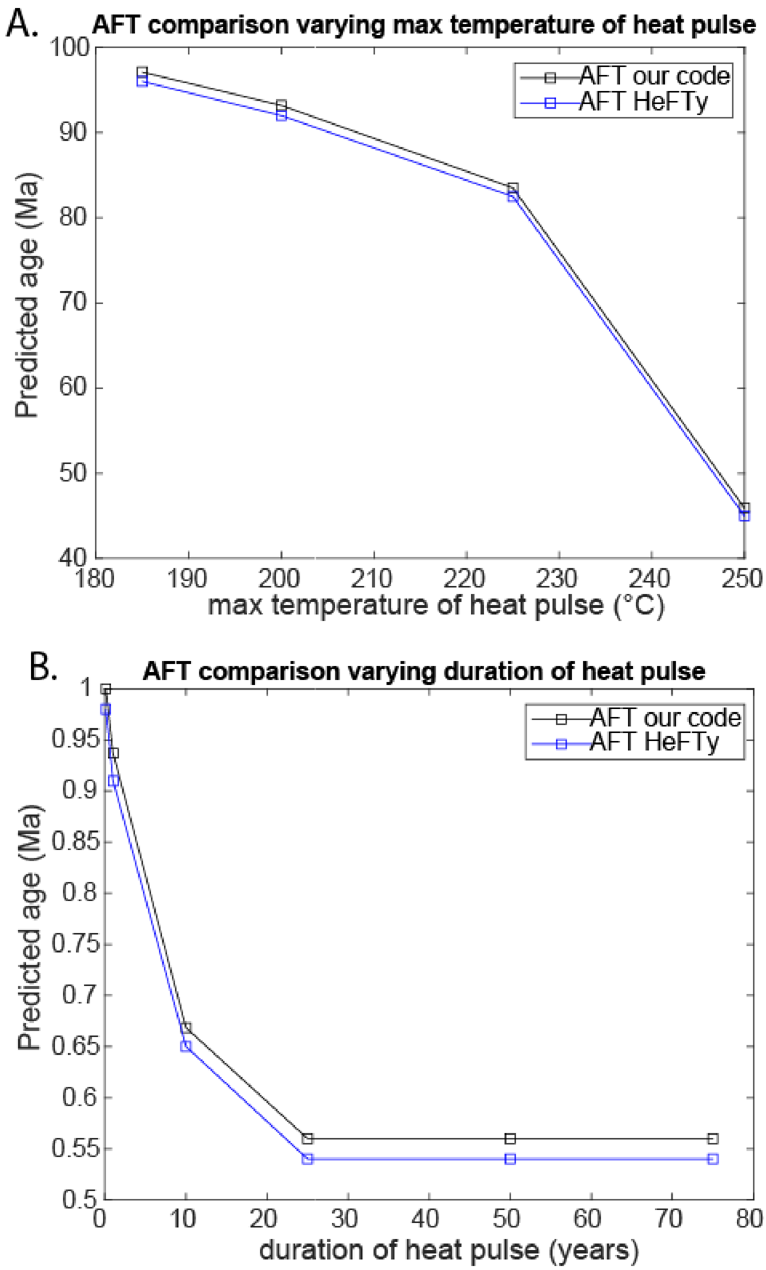

Figure 3.8– Results from apatite fission track (AFT) sensitivity testing with HeFTy (Ketcham, 2005). (A) Comparison between AFT ages calculated by HeFTy and ages calculated by the model used in this study while varying max temperature of the heat pulse. Comparison used an initial age of 100 Ma, a reset age of 16 Ma, and a heating duration of 3 years. (B) Comparison between AFT ages calculated by HeFTy and ages calculated by the model used in this study while varying the duration of the heat pulse. Comparison used an initial age of 1 Ma, a reset age of 0.5 Ma, and a max temperature of 235°C.

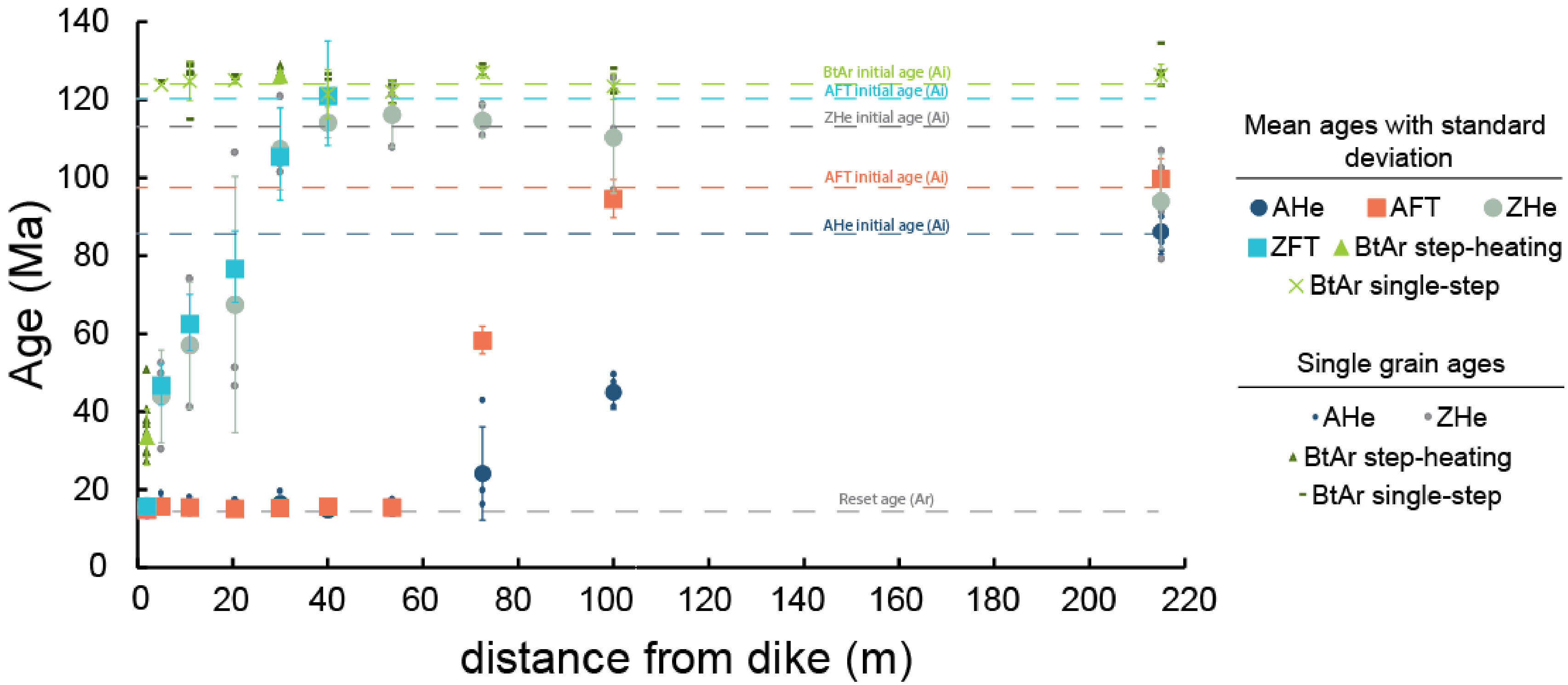

Figure 3.9– Thermochronologic ages from the Jackson A transect and corresponding A_r (reset age) and A_i (initial ages) for each system.

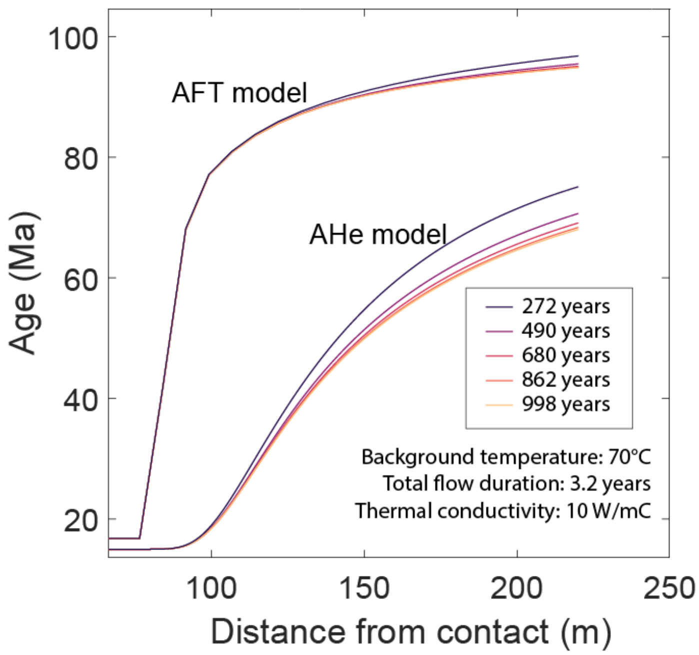

Figure 3.10– Comparison of model ages for apatite (U-Th)/He and apatite fission track for different simulation durations. Note that durations >680 years are within standard error for apatite (U-Th)/He ages.

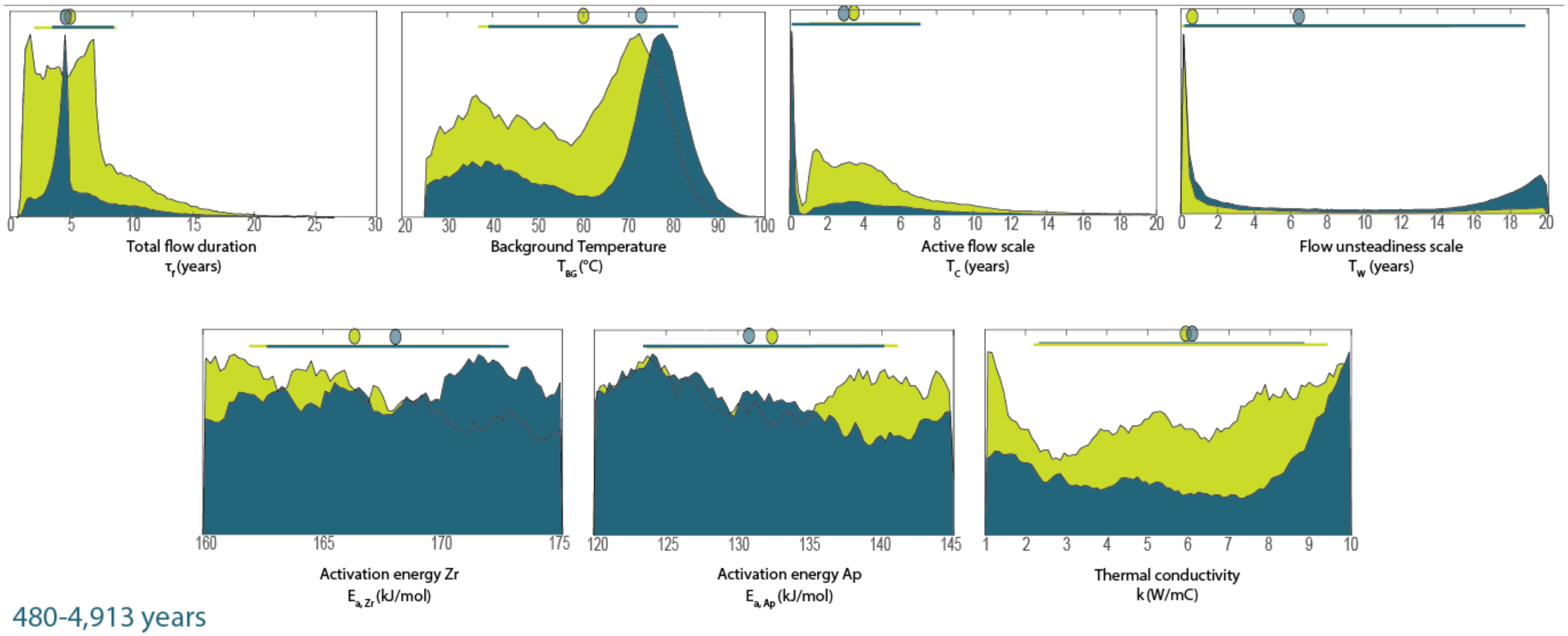

Figure 3.11– Comparison of posterior probability density functions using two different simulation durations. MCMC inversion used apatite and zircon (U-Th)/He ages. Results from model simulation durations between 480-4,913 years is shown in blue, and results from durations between 998-10,009 years is shown in light green. Circle shows the median value for each distribution and the colored bar shows 68% confidence intervals for each distribution.

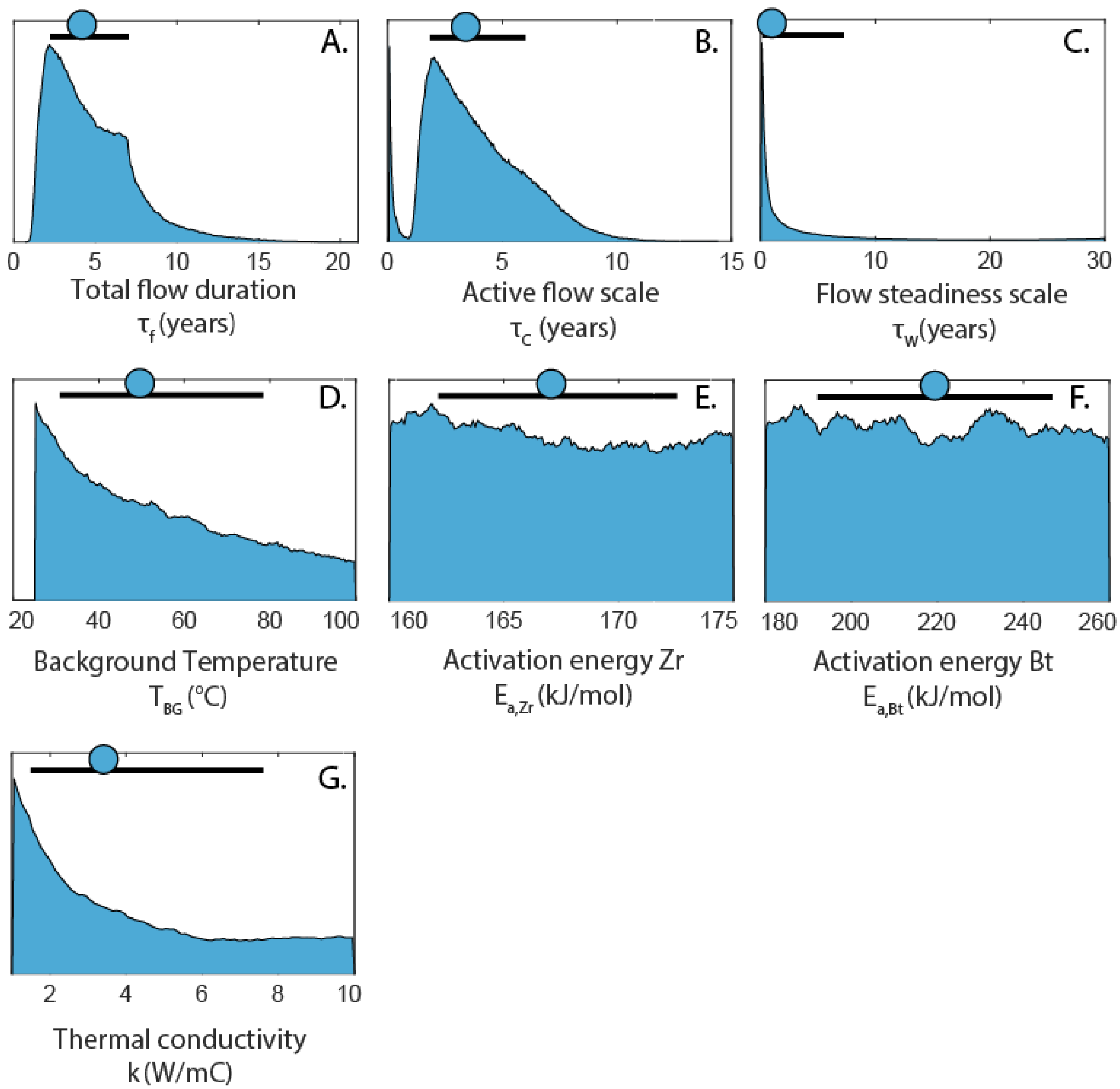

Figure 3.12– Marginal posterior probability density functions for scenario 1 (high-temperature) model parameters. τ_f is derived from τ_c and τ_w (see Karlstrom et al., 2019). Blue circle corresponds to the median of the distribution, while the black bar represents the 68% confidence interval.

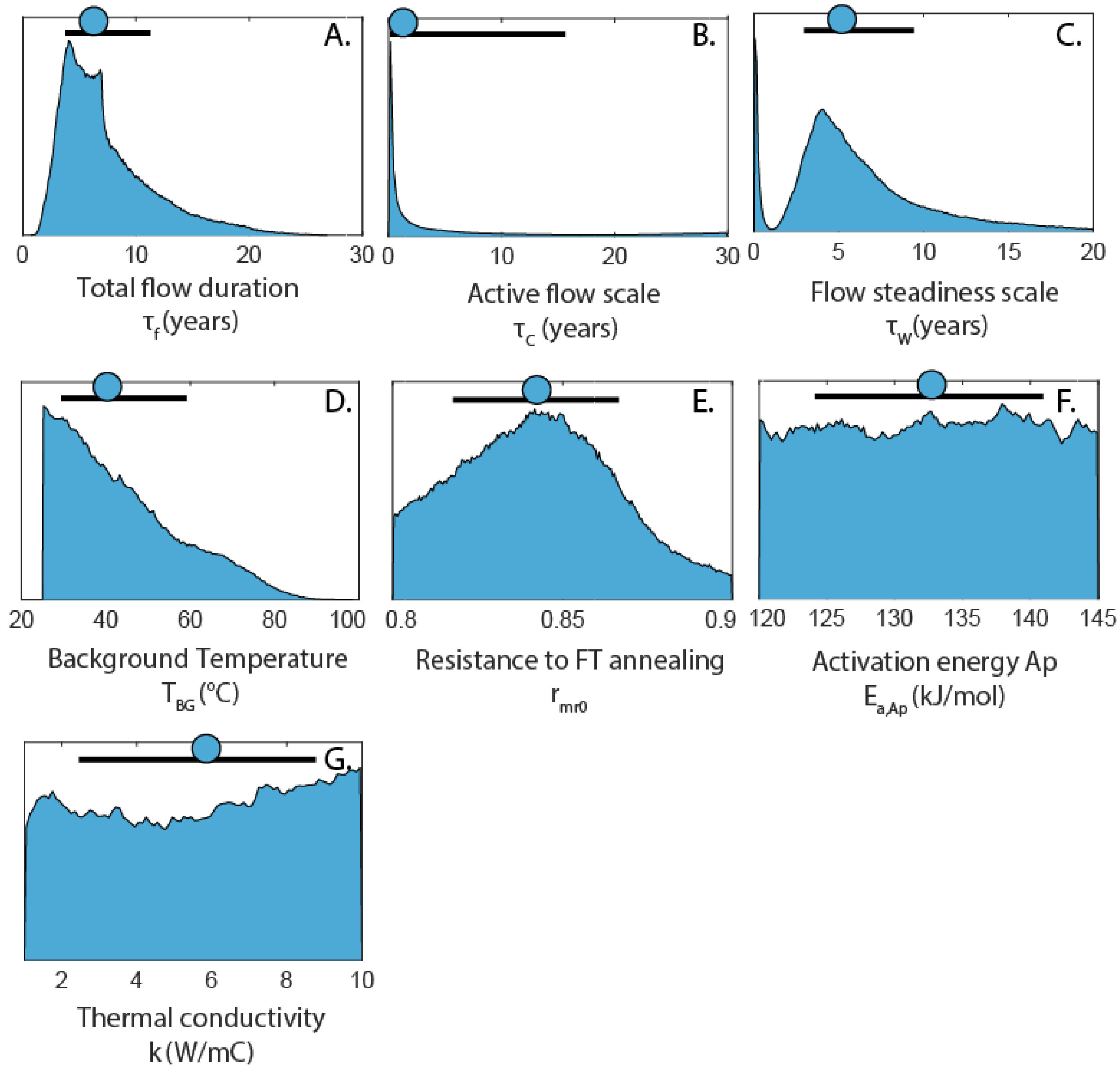

Figure 3.13– Marginal posterior probability density functions for scenario 2 (low-temperature) model parameters. τ_f is derived from τ_c and τ_w (see Karlstrom et al., 2019). Blue circle corresponds to the median of the distribution, while the black bar represents the 68% confidence interval.

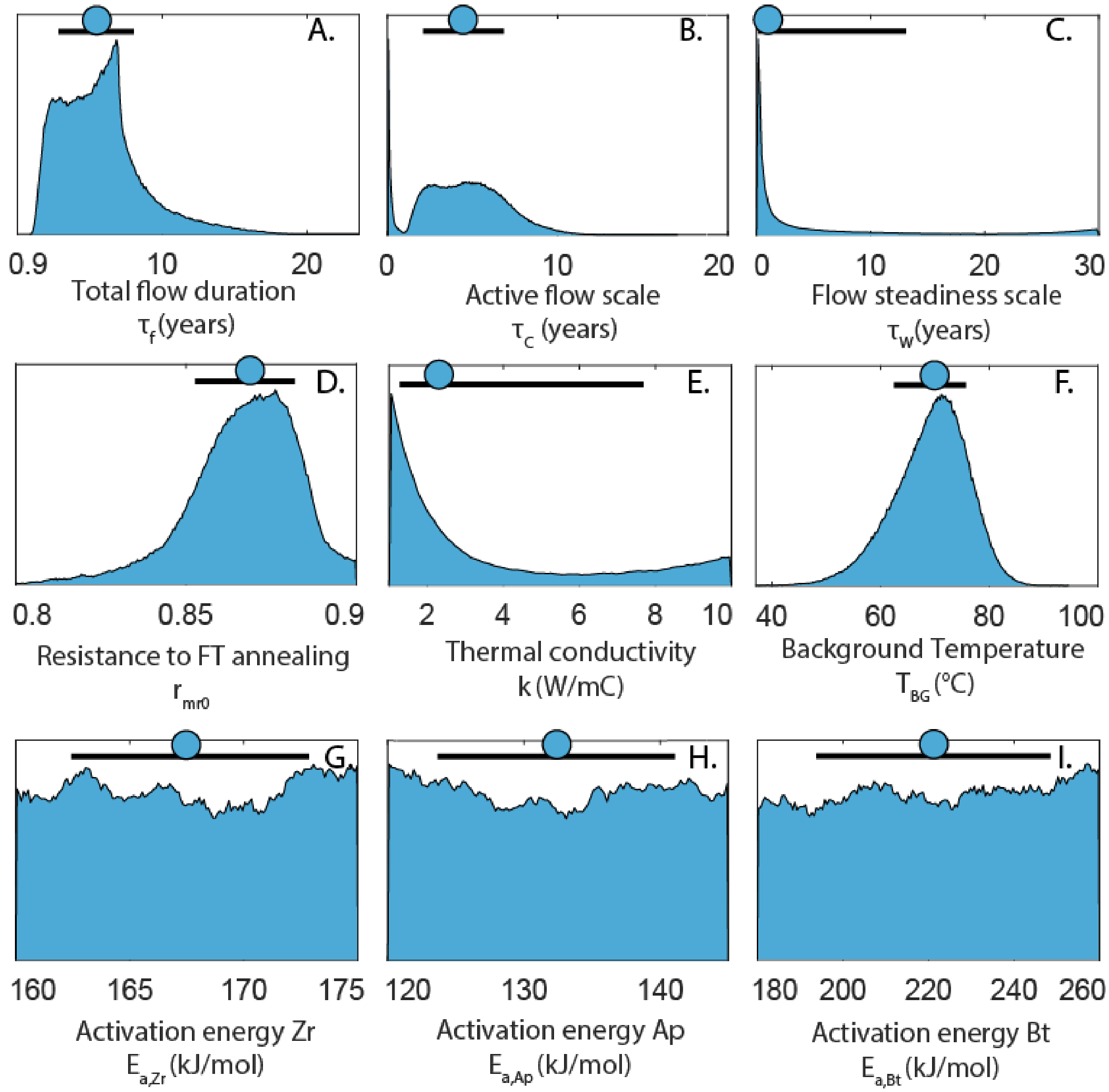

Figure 3.14– Marginal posterior probability density functions for scenario 3 (all chronometers) model parameters. τ_f is derived from τ_c and τ_w (see Karlstrom et al., 2019). Blue circle corresponds to the median of the distribution, while the black bar represents the 68% confidence interval.

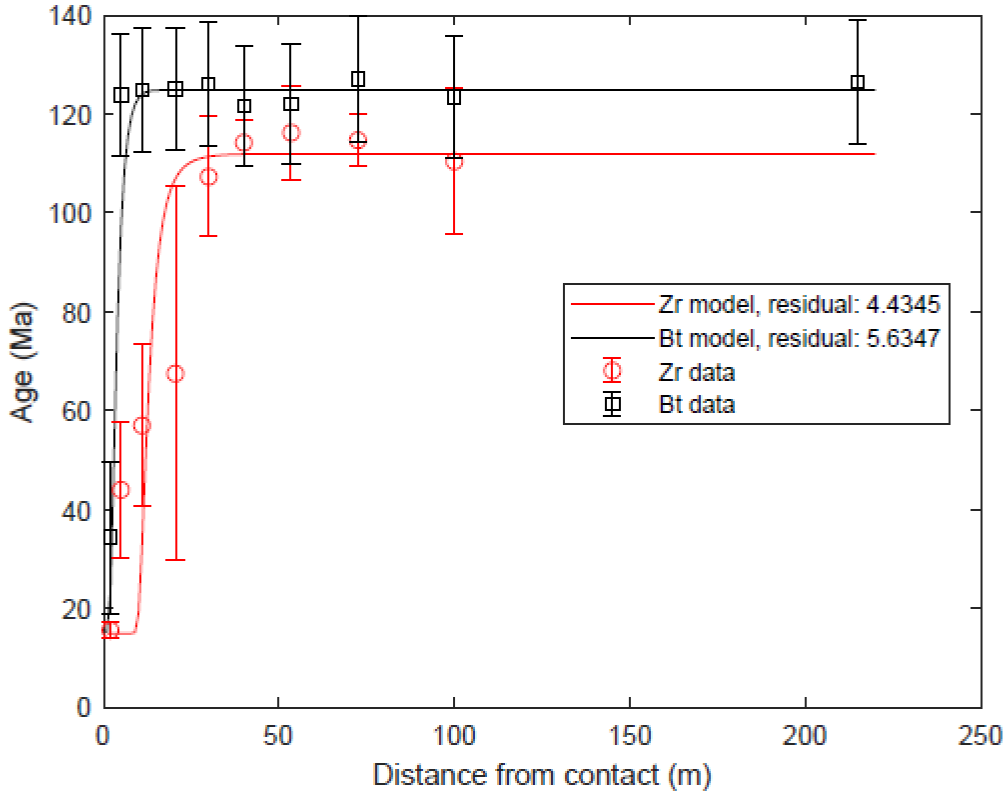

Figure 3.15– Predicted ages (colored lines) from scenario 1 (high temperature) median best fitting values compared to observed biotite $^{40}Ar/^{39}Ar$ (black) and zircon (U-Th)/He (red) cooling ages. Error bars are set specifically for modeling purposes and do not reflect standard deviation here (see section 3.5.3). Residuals calculated based on misfit to observed data.

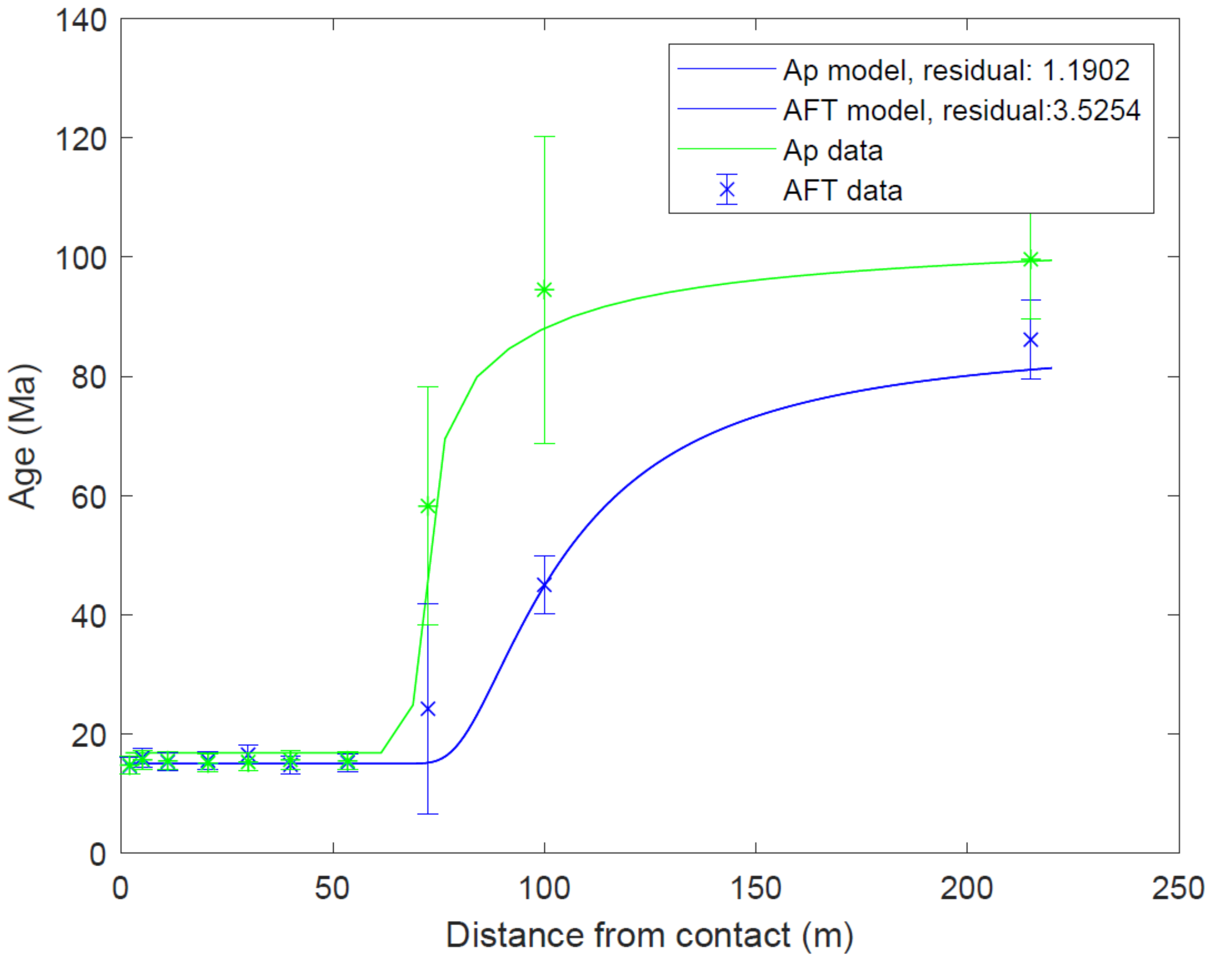

Figure 3.16– Predicted ages (colored lines) from scenario 2 (low temperature) median best fitting values compared to observed apatite fission track (green) and apatite (U-Th)/He (blue) coling ages. Error bars are set specifically for modeling purposes and do not reflect standard deviation here (see section 3.5.3). Residuals calculated based on misfit to observed data.

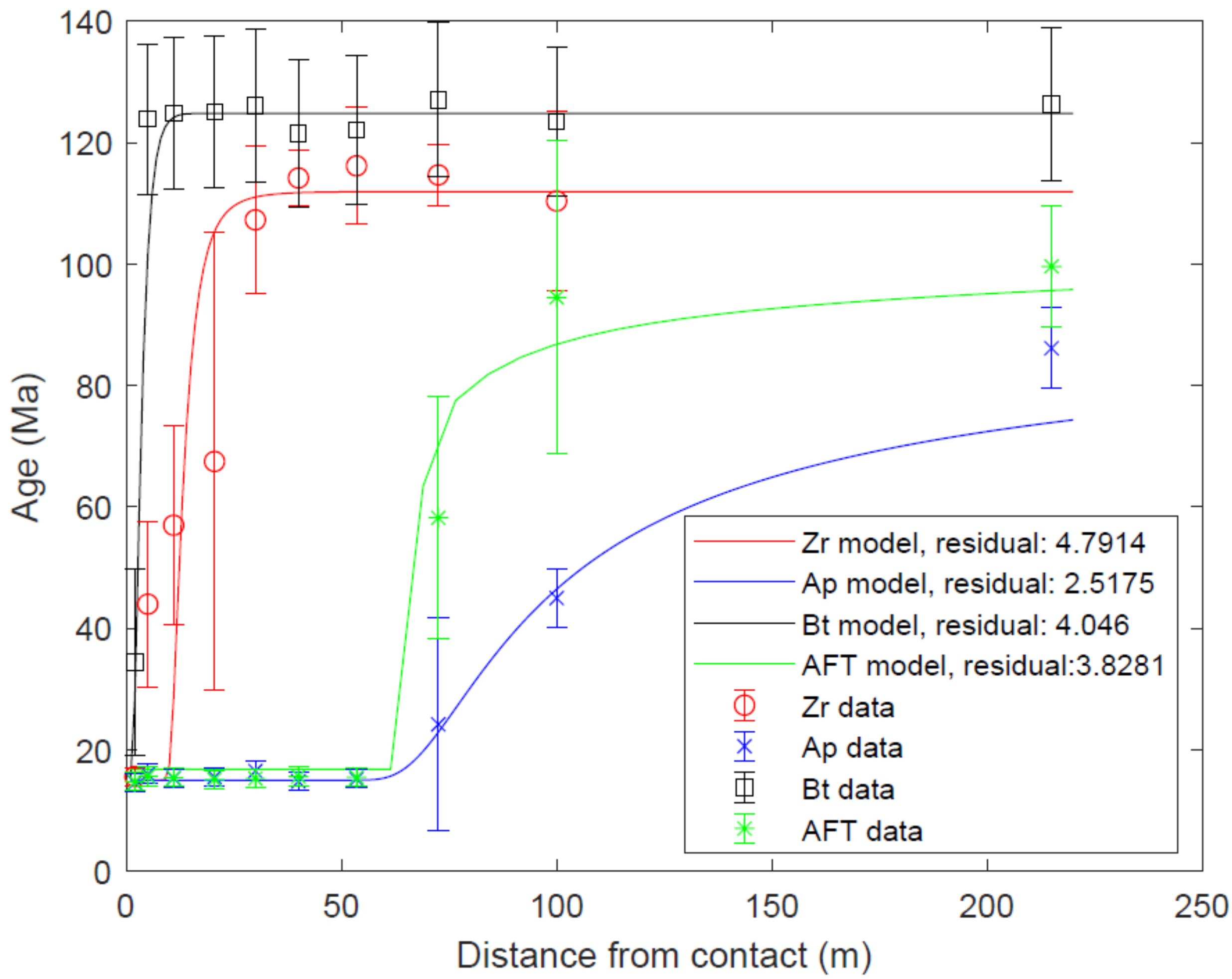

Figure 3.17– Predicted ages (colored lines) from median best fitting values for inverted parameters compared to observed biotite $^{40}Ar/^{39}Ar$ (black), zircon (U-Th)/He (red), apatite fission track (green), and apatite (U-Th)/He (blue) cooling ages. Error bars are set specifically for modeling purposes and do not reflect standard deviation here (see section 3.5.3). Residuals calculated based on misfit to observed data.

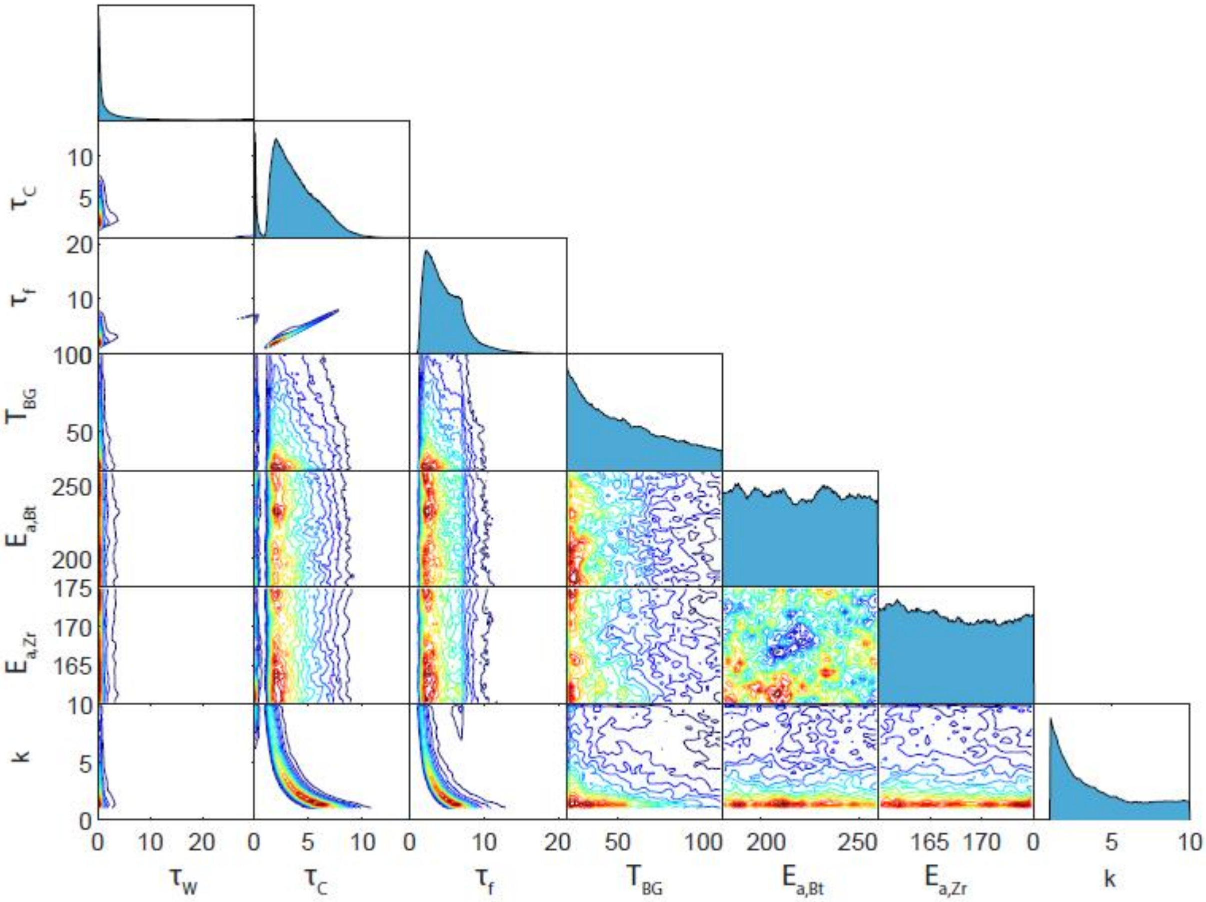

Figure 3.18– Bivariate plot for parameters explored during scenario 1 (high temperature) MCMC inversion. τ_w– flow unsteadiness scale, τ_c– active flow scale, τ_f– total flow duration (derived), T_{BG}– background temperature, *k*– thermal conductivity, E_a– activation energy for zircon (U-Th)/He and biotite $^{40}Ar/^{39}Ar$.

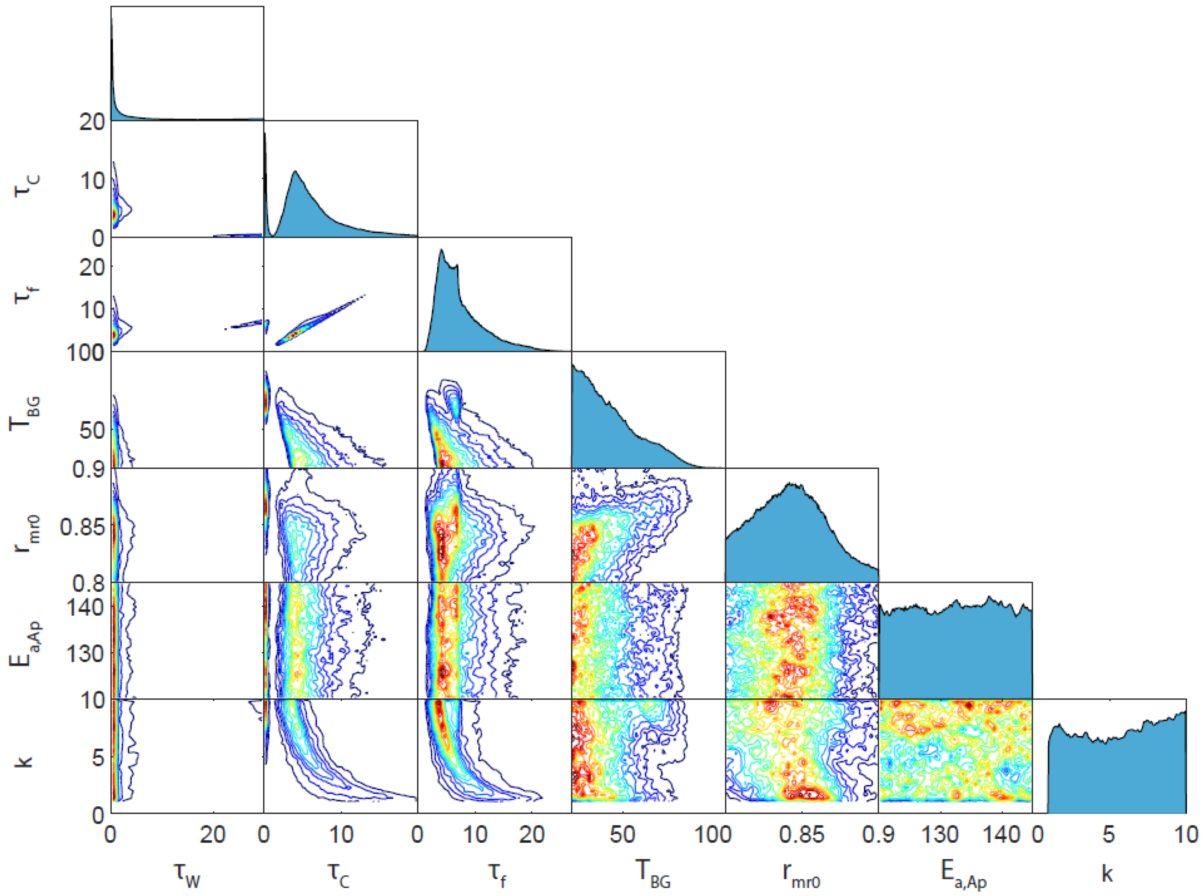

Figure 3.19– Bivariate plot for parameters explored during scenario 2 (low temperature) MCMC inversion. τ_w– flow unsteadiness scale, τ_c– active flow scale, τ_f– total flow duration (derived), T_{BG}– background temperature, k– thermal conductivity, E_a– activation energy for apatite (U-Th)/He, r_{mr0}– kinetic parameter for apatite fission track.

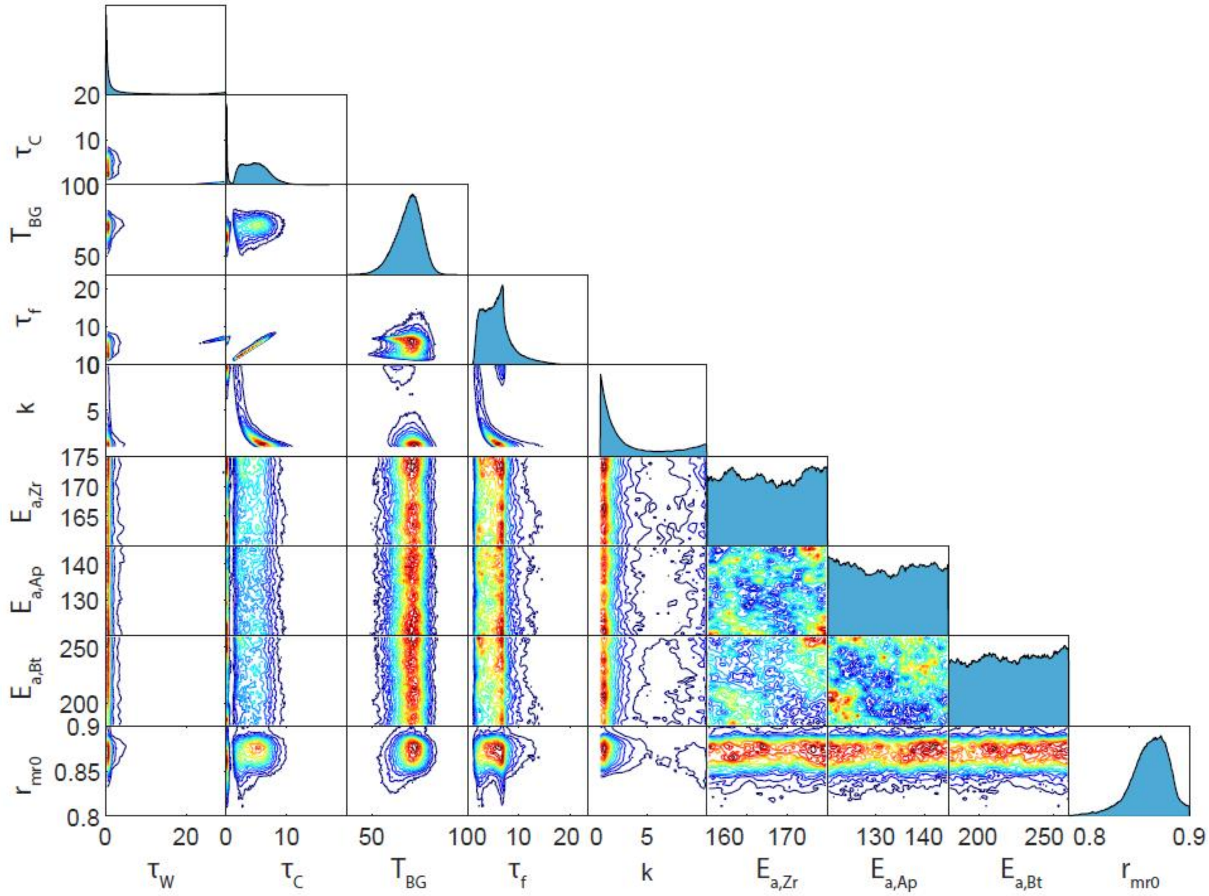

Figure 3.20– Bivariate plot for parameters explored during scenario 3 (all chronometers) MCMC inversion. τ_w– flow unsteadiness scale, τ_c– active flow scale, τ_f– total flow duration (derived), T_{BG}– background temperature, k– thermal conductivity, E_a– activation energy for zircon and apatite (U-Th)/He and biotite $^{40}Ar/^{39}Ar$, r_{mr0}– AFT kinetic parameter.

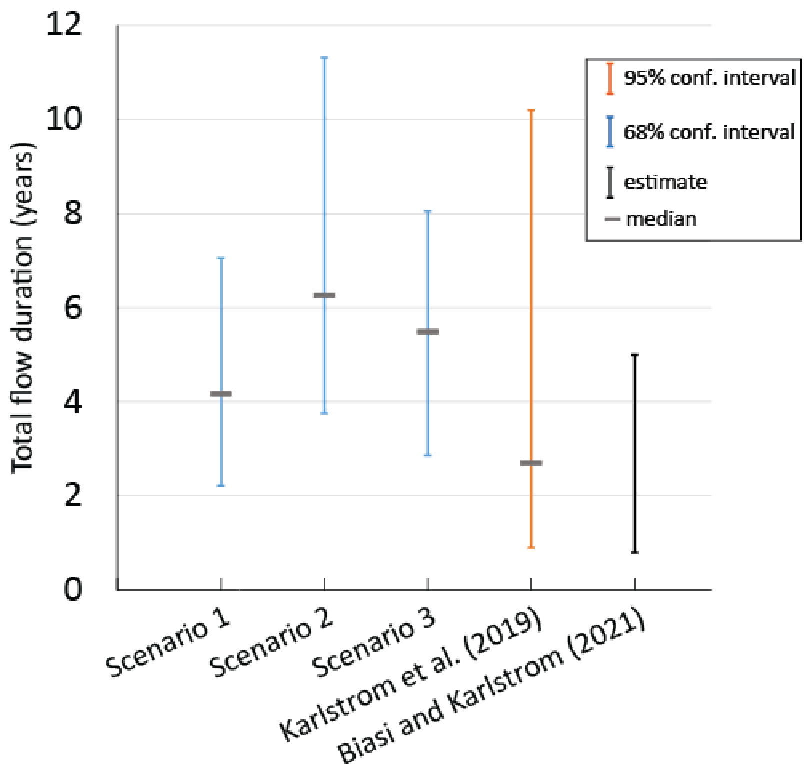

Figure 3.21—Comparison of modeling results from this study, Karlstrom et al. (2019), and Biasi and Karlstrom (2021) for the total magma flow duration parameter (τ_f). Scenario 1 modeled cooling ages from high-temperature chronometers, scenario 2 modeled cooling ages from low-temperature chronometers, and scenario 3 modeled cooling ages from all chronometers.

Table 3.1—Thermochronology at Jackson A dike segment.

	Apatite (U-Th)/He					Zircon (U-Th)/He			
Sample ID	distance from dike	# of apatites analyzed	Avg. AHe Age	SD	AHe Age Dispersion	# of zircons analyzed	Avg. ZHe Age	SD	ZHe Age Dispersion
	m		*Ma*	*Ma*	*SD/Avg (Ma)*		*Ma*	*Ma*	*SD/Avg (Ma)*
2E1	2	4	14.6	0.4	0.03	3	15.6	0.3	0.02
2E2	5	4	16	1.3	0.08	3	44.0	11.9	0.27
2E3	11	4	15	1.0	0.07	3	57.0	16.2	0.28
2E4	20.5	4	15.5	0.7	0.05	3	67.5	32.8	0.49
2E5	30	4	16	1.3	0.08	3	107.3	10.5	0.10
2E6	40	3	14.8	0.6	0.04	3	114.2	4.0	0.04
2E7	53.5	4	15.2	0.8	0.05	3	116.2	8.4	0.07
2E8	72.5	4	24	12.0	0.50	3	114.7	4.4	0.04
2E9	100	3	45	4.4	0.10	3	110.4	14.3	0.13
20JACK-K1	215	4	86	5.8	0.07	4	94.0	12.2	0.13

Table 3.1—Thermochronology at Jackson A dike segment (continued).

	Biotite Ar/Ar					Apatite fission track					Zircon fission track		
Sample ID	type of analysis	# of analysis	Avg. BtAr Age	SD	BtAr Age Dispersion	Pooled Age	95% (-)	95% (+)	MTL	SD	Pooled Age	95% (-)	95% (+)
			Ma	*Ma*	*SD/Avg (Ma)*	*Ma*	*Ma*	*Ma*	*µm*	*µm*	*Ma*	*Ma*	*Ma*
2E1	SH	10	34	6.8	0.20	15	1.6	1.7	15	1.1	16	1.9	2.2
2E2	SSF	2	123.9	0.3	0.00	15	1.6	1.8	15	1.2	47	5.0	5.6
2E3	SSF	6	125	5.0	0.04	15	1.6	1.8	15	1.2	63	6.8	7.6
2E4	SSF	3	125.0	0.5	0.00	15	1.5	1.7	14	1.3	77	8.6	9.7
2E5	SH	7	126	1.2	0.01	15	1.4	1.5	14	1.1	105	11.2	12.5
2E6	SSF	3	122	6.2	0.05	16	1.5	1.7	15	1.2	121	12.7	14.1
2E7	SSF	3	122	3.0	0.02	15	1.1	1.2	14	1.2			
2E8	SSF	3	127	1.3	0.01	58	3.4	3.6	12	2.6			
2E9	SSF	3	123	3.3	0.03	95	4.8	5.1	13	1.6			
20JACK-K1	SSF	9	126	2.8	0.02	100	5.0	5.2	14	1.5			

SH- step heating
SSF- single step fusion

MTL- mean track length

Table 3.2—Reset (A_r) and unreset ages (A_i) chosen for modeling Jackson A dike segment.

	A_i (unreset/initial age)	A_r (reset age)
Biotite $^{40}Ar/^{39}Ar$	125 Ma	15 Ma
Zircon (U-Th)/He	112 Ma	15 Ma
Apatite fission track	97 Ma	15 Ma
Apatite (U-Th)/He	86 Ma	15 Ma

Table 3.3—Summary of parameters explored in the numerical model.

	Parameter name (units)	Description
E_a	Activation energy (kJ/mol)	Controls how quickly noble gas daughter products can escape from apatite, zircon, or biotite. I vary these parameters between commonly accepted experimental values of activation energy for each system.
r_{mr0}	Resistance to fission-track annealing	Controls how quickly fission-tracks anneal in the apatite fission track system. Other kinetics terms in the AFT system can also vary between crystals, but those values are poorly understood. To avoid having too many AFT kinetic parameters in this model, I opt to vary only r_{mr0} as a catch all for variable AFT kinetics (R. Ketcham, personal comm.)
k	Thermal conductivity (W/m°C)	Controls how quickly heat is conducted through the wallrocks. Typical granite values are between 2-4 W/m°C, but I explore a wider range (1-10 W/m°C) to account for the possibility of an additional advective heat component.
T_{BG}	Background temperature (°C)	The ambient temperature of the wallrocks prior to dike emplacement, and ultimately the temperature that the wallrocks will return to after the dike's thermal perturbation. Because our thermal model is not integrated over the entire thermal history of the Wallowa batholith, but rather just the timeframe associated with dike emplacement and dike cooling, T_{BG} can represent a transient background temperature that may have only been active for the span of 10^2-10^3 years.
τ_c	Active flow scale (years)	The duration of active magma flow through the dike, assuming that dike flow stops and magma cools instantaneously.
τ_w	Flow unsteadiness scale (years)	Physically controls how quickly magma temperature cools down towards the end of a dike's lifetime. This behavior is meant to mimic waning magma flow and the growth of a thermal boundary layer. If this parameter is very large, it may also reflect reactivation of a dike segment over time.
τ_f	Total flow duration (years)	Derived from both τ_c and τ_w using the relationship outlined in equation 3.1. This parameter is the total duration that magma was flowing through a dike, and is used to interpret magma flow rates.

Table 3.4—Summary of modeling scenarios. BtAr- biotite $^{40}Ar/^{39}Ar$, ZHe- zircon (U-Th)/He, AFT- apatite fission track, AHe- apatite (U-Th)/He, r_{mr0}- resistance to fission-track annealing E_a- activation energy, k- thermal conductivity, T_{BG}- background temperature, τ_c- active flow scale, τ_w- unsteadiness flow scale.

	Scenario 1 High-Temperature	Scenario 2 Low-Temperature	Scenario 3 All Chronometers
Datasets used	BtAr ZHe	AFT AHe	BtAr ZHe AFT AHe
Parameters explored	E_a (BtAr) E_a (ZHe) k T_{BG} τ_c τ_w	r_{mr0} (AFT) E_a (AHe) k T_{BG} τ_c τ_w	E_a (BtAr) E_a (ZHe) rmr0 (AFT) E_a (AHe) k T_{BG} τ_c τ_w
# cooling ages	19	20	39
Purpose of model	Test which datasets better constrains certain parameters	Test which datasets better constrains certain parameters	Intercalibration of all chronometers

Table 3.5—Parameters, uniform prior parameter ranges, and MCMC inversion results. r_{mr0}- resistance to fission-track annealing E_a- activation energy, k- thermal conductivity, T_{BG}- background temperature, τ_c- active flow scale, τ_w- unsteadiness flow scale, and τ_f— total flow duration.

Parameter	T_{BG} °C	T_c (years)	T_w (years)	k (W/mC)	$E_{a,zr}$ (kJ/mol)	$E_{a,bt}$ (kJ/mol)	$E_{a,ap}$ (kJ/mol)	r_{mr0}	T_f (years)	AIC	BIC
Prior lower bound	25	0.05	0.05	1	160	180	120	0.8			
Prior upper bound	100	20	30	10	175	260	145	0.9			
High Temperature										84.7	90.4
Median best fit	49.61	3.41	0.98	3.41	167.06	219.39			4.17		
68% conf. interval	[30.87, 78.61]	[1.85, 6.03]	[0.14, 7.34]	[1.49, 7.62]	[162.13, 172.56]	[192.07, 246.85]			[2.22, 7.05]		
95% conf. interval	[25.75, 96.32]	[0.17, 8.53]	[0.06, 27.64]	[1.06, 9.66]	[160.32, 174.66]	[181.79,258.04]			[1.44, 11.42]		
Low Temperature										34.3	40.3
Median best fit	40.36	5.18	1.29	5.85			132.72	0.842	6.26		
68% conf. interval	[29.33, 59.35]	[2.95, 9.46]	[0.13, 15.77]	[2.44, 8.78]			[124.08, 140.95]	[0.818, 0.867]	[3.76, 11.31]		
95% conf. interval	[25.59, 75.98]	[0.09, 16.15]	[0.06, 28.64]	[1.23, 9.89]			[120.56, 144.41]	[0.803, 0.891]	[2.32, 18.51]		
All Chronometers										149.2	162.5
Median best fit	69.90	4.45	1.01	2.30	167.48	221.23	132.41	0.869	5.49		
68% conf. interval	[62.37, 75.75]	[2.09, 6.85]	[0.14, 13.24]	[1.26, 7.72]	[162.43, 172.87]	[193.64, 248.55]	[123.61, 141.10]	[0.853, 0.882]	[2.86, 8.05]		
95% conf. interval	[53.85, 80.95]	[0.09, 9.30]	[0.06, 29.14]	[1.03, 9.76	[160.35, 174.70]	[181.94, 258.40]	[120.49, 144.44]	[0.828, 0.894]	[1.70, 13.29]		

Chapter 4: Extending the Story to the Maxwell Lake Dike Complex

4.1 Introduction

In the previous chapter, I used the Jackson A dike segment as a case study for refining low-temperature thermochronology as a tool for quantifying the duration of magma flow through a dike. In this chapter, I use thermochronology next to other dike segments in the Maxwell Lake area of the Wallowa Mountains, OR as a qualitative tool for comparing the relative thermal impacts of each dike segment. This approach provides preliminary insight as to how the emplacement history of these dike segments may, or may not, be related, and it lays the foundation for future numerical modeling at each dike segment. Due to a lack of modern, volcanic analogues to LIP-scale eruptions, as well as limited exposures of LIP intrusive components, the processes governing shallow-crustal magma transport are poorly understood. By using thermochronology to investigate multiple dike segments in the Wallowa Mountains, I further elucidate how long eruptions in the main phase of the Columbia River Flood Basalts (CRFBs) were active.

A recent study (Biasi and Karlstrom, 2021) mapped dike segments in the Maxwell Lake area and interpreted that each segment is likely part of a larger, interconnected dike complex (hereafter the Maxwell Dike Complex, or MDC; Figure 4.1). Although these dike segments appear to be en échelon sections of a single dike, it is unclear whether magma flow was temporally continuous and/or spatially homogenous across the MDC. In other words, were all segments emplaced during the same eruptive event, or was there reactivation of an already existing dike system in this area? Or, if the dike segments were emplaced at the same time, was there magma focusing at a central, vent-feeding segment? Here, I present new geochemical data and thermochronologic transects next to two dike segments in the MDC, and integrate this data with existing data from the Jackson A dike segment (see Chapter 3) in order to assess local variations in magma flow and composition within the MDC.

4.2 Methods

4.2.1 Sampling Strategy

Within the MDC, I sampled two dike segments east of the Jackson A dike: the Jackson E dike segment and the Maxwell A dike segment (Table 2.1; Figure 4.1). All three dike segments share the general N10E strike of the Chief Joseph dike swarm, with undulations in strike up to ~20° along each segment. Additionally, each dike segment has ~2 m partial melt zones at their margins, suggesting that each was a relatively long-lived conduit (Petcovic and Grunder, 2003; Morriss et al., 2020).

Jackson E dike is northeast of Jackson A dike (Figure 4.1). I took five samples in a 100 m transect to the west of the Jackson E dike-wallrock contact. The transect began with the first sample at 2.7 m from the dike margin, outside the partial melt zone in the wallrock.

The Maxwell A dike segment (previously studied by Petcovic and Grunder, 2004 and Petcovic and Dufek, 2005) is exposed ~0.83 km northeast of Jackson A dike (Figure 4.1). Due to limitations in wallrock exposure, I took three samples in a short, 22.5 m transect on the western side of the dike-wallrock contact. The transect began with the first sample 3.1 m away from the dike contact, outside of the partial melt zone.

We collected approximately 2 kg of wallrock for each sample in the thermochronologic transects. Samples were processed for thermochronologic analysis using standard procedures as outlined in Chapter 2.3. I generated apatite and zircon (U-Th)/He ages from samples collected next to both dikes. Additionally, biotite $^{40}Ar/^{39}Ar$ ages were generated from the wallrock samples collected next to the Maxwell A dike. Samples were also collected at each dike segment by Rachel Hampton (in prep.) for major element, trace element analysis, and isotope analysis.

4.3 Thermochronology Results

Apatite and zircon (U-Th)/He (AHe and ZHe) and biotite $^{40}Ar/^{39}Ar$ (BtAr) data for the Jackson A, Maxwell A, and Jackson E dike transects can be found in Tables 4.1, 4.2, and 4.3, respectively. The general trend in thermochronologic ages next to both the Maxwell A and Jackson E dike segments (Figures 4.2 and 4.3, respectively) is similar to that of the Jackson A dike segment (Figure 3.5), following the expected younger to older trend and "nested" resetting behavior that reflects each chronometer's temperature sensitivity (see Figure 3.9).

4.3.1 Maxwell A Dike Segment

Thermochronology results for the Maxwell A dike transect are shown in Figure 4.2. Average AHe ages in the samples collected at 3.1 m and 15 m from the dike-wallrock contact are 17.9 ± 0.3 Ma and 17.4 ± 0.3 Ma (respectively), whereas the sample collected at 22.5 m has an average AHe age of 91 ± 4.5 Ma (Table 4.1). The average ZHe age in the sample collected at 3.1 m from the dike is 16 ± 1.6, and the ZHe ages from samples collected at 15 m and 22.5 m are 98 ± 5.0 Ma and 105 ± 6.6 Ma (respectively; Table 4.2). The average BtAr single-step fusion age at 3.1 m from the dike is 77 ± 12.0 Ma, whereas the average BtAr ages at 15 m and 22.5 m are 129 ± 2.7 Ma and 133 ± 3.9 Ma (respectively; Table 4.3).

4.3.2 Jackson E Dike Segment

In general, the samples in the Jackson E transect followed expected resetting trends for both AHe and ZHe, with both systems transitioning from younger ages to older ages farther from the dike (Figure 4.3). In this transect, average AHe ages ranged from 16.5 ± 0.3 Ma to 85 ± 1.7 Ma, with a partially reset age of 24 ± 7.2 Ma in the sample collected at 40 m from the dike contact and a non-reset age of 85 ± 1.7 Ma in the sample collected at 100 m from the dike. Average ZHe ages ranged from 24 ± 5.3 Ma to 107 ± 8.5 Ma, with a partially reset age of 24 ± 5.3 Ma at 5.5 m from the dike and a non-reset age of 107 ± 8.5 Ma at 40 m from the dike.

However, the sample closest to the dike (2.7 m) does not have fully reset (ca. 16-17 Ma) AHe and ZHe ages, as I expected based on the transects next to other dikes. Instead, this sample has anomalously old single-grain ZHe (82 ± 1.28 Ma to 102.4 ± 1.3 Ma) and AHe ages (16.6 ± 0.2 Ma to 40.4 ± 0.5 Ma). The problem with this anomalously old age is that the next farthest sample (5.5 m) has young single-grain ZHe (16.3 ± 0.2 Ma to 32.1 ± 0.5 Ma) and AHe ages (16.7 ± 0.3 Ma to 18.6 ± 0.2 Ma), and the expected spatial pattern (young to old ages away from the dike) resumes starting at this 5.5 m sample.

4.4 Discussion

4.4.1 Addressing Complexities in the Jackson E data set

The anomalous sample in the Jackson E transect must be interpreted before I can begin a broader comparison to other MDC segments. First, I consider if there is a geologically feasible explanation for the spatial pattern of resetting in the two samples closest to the dike. Then, I consider the possibility of a problem during sampling in the field. Finally, given these considerations, I describe my preferred approach to interpreting the thermochronologic data in the Jackson E transect.

A 1-D conductive heating model for wallrocks next to a dike will always result in the rocks closest to the dike experiencing the highest peak temperatures and the rocks farther from the dike experiencing lower peak temperatures, because heat is conducted away from the dike (Figure 2.3). A simple conductive heating model precludes the possibility of preserving old cooling ages next to the dike but resetting the same system at distances farther from the dike because the cooling ages are directly representative of both the duration and temperature of heating experienced at each distance away from the dike. Therefore, the anomalous ages observed in the Jackson E transect are not explained using a simple conductive heating model.

The anomalous sample also cannot be explained by transporting heat via an additional advective process without calling upon a complex geometry of permeable zones that may have focused the flow of hot fluids. The circulation of hydrothermal fluids can expedite the transfer of heat away from the dike via advection, but an advective heating mechanism would still be expected to produce a younger to older cooling age trend away from the dike (Bindeman et al., 2020) unless there were conduits that enhanced fluid flow irregularly in space. To generate the anomalous age trends observed in the Jackson E transect, a heating mechanism would need to produce locally hot and locally cold spots along the transect. Although there may be a process in nature that can produce this heating pattern, it is beyond the scope of the numerical approach used in this study to model such a process. As such, I turn to alternative explanations for this age trend.

Assuming that the rocks did experience heating consistent with the conductive heat transfer model, the anomalous age trend next to the Jackson E segment could hypothetically be due to variations in apatite and zircon crystal size or chemistry. However, there are no significant trends in age vs. eU or age vs. grain size (Figure 4.4). Additionally, since both the AHe and ZHe ages are older than expected in this closest sample and because the ZHe ages are reproducible at the two closest samples, it appears that the ages generated are accurate; however, given the position of this closest sample relative to the dike and the other ages in this transect, the AHe and ZHe ages from this sample do not appear to be geologically reasonable.

Because it is unlikely that the sample closest to the dike reflects the true age 2.7 m from the Jackson E dike segment based on the current understanding of heat flow near dikes, I now explore the possibility of unanticipated complications to my sampling strategy next to the Jackson E dike segment. There are two main explanations for the complex age distribution observed at the Jackson E dike segment: (1) the sample was mixed-up with another sample in the transect due to a labeling error in the field, and (2) the sample was taken from float and is not representative of rocks that are actually 2.7 m from the dike.

A sample mix-up in the field is unlikely because each sample was labeled at its respective outcrop and samples were not gathered together (i.e., mixed up) until all samples were collected, bagged, and labeled. Additionally, if samples 1 and 2 were switched, then switching the samples back should correct the anomalous age trend next to the dike; however, even if samples 1 and 2 were switched, there would still be older than expected single grain AHe ages 5.5 m from the dike followed by younger single grain AHe ages 16.9 m from the dike, which is considered geologically improbable given the conductive heating model used here. Ultimately, I argue that this explanation is unlikely and does not completely resolve the anomalous age trend observed next to the Jackson E dike segment.

The second explanation, that the material I collected 2.7 m from the dike contact was not in place, is more plausible: although special care was used to ensure that all samples in each transect were taken from in situ wallrock, the wallrocks close to the contact of the Jackson E dike segment were more weathered than in other sample locations (Figure 4.5), which made it difficult to discern which wallrocks were truly in place. At the time, I believed I was sampling in situ wallrock; however, it is possible that I sampled from a very large float block instead. This sampling error could result in the age being representative of wallrock that traveled from farther away from the dike (i.e., out of context from Jackson E dike heating). If this is the case, I can omit this sample and interpret the resetting trends using only the other four samples in the transect.

In order to make comparisons between all three dike segments in the MDC, I interpret that the anomalous age measured 2.7 m from the dike is from wallrock float, and is therefore excluded in my interpretations.

4.4.2 Comparison to Jackson Main Dike

In this section, I compare each dike segment's thermal impact using the extent of thermochronologic resetting next to the dike as a qualitative proxy for magma flow duration. Both the Maxwell A dike and Jackson E dike have considerably narrower thermochronologic resetting zones than the Jackson A dike (Figure 4.6). In terms of distance alone, the Jackson A dike has the widest resetting zone (215 m to first non-reset AHe age), the Jackson E dike has the second-widest resetting zone (100 m to first non-reset AHe age), and the Maxwell A dike has the narrowest resetting zone (22.5 m to first non-reset AHe age). However, simply comparing the distance from the dike margin to the first non-reset sample is insufficient, as it does not take into account the width of each dike, a length scale that may influence the total amount of heat emitted by an intrusive body and thus the pattern of thermochronometer resetting in the wallrocks (Murray et al., 2018). To better compare the resetting zones around these dike segments, I normalize the distance to the first non-reset sample to the width of the dike. I call this new dimensionless term the dike's *thermal imprint*, where larger values reflect larger thermal imprints (Figure 4.7). For the ZHe system, the Jackson A, Jackson E, and Maxwell A segments have thermal imprints of 3.3, 3.9, and 2.5, respectively. For the AHe system, the Jackson A, Jackson E, and Maxwell A segments have thermal imprints of 23.9, 23.2, and 3.8. These thermal imprints suggest that the Jackson A and Jackson E dike segments had similar thermal impacts on their surroundings, and that the Maxwell A dike segment did not heat adjacent wallrocks as significantly as either the Jackson A or Jackson E dike segments.

Based on recent geochemical analysis and preliminary model classification of segments in the MDC, the composition of the Jackson A dike segment basalt is significantly different than that of both the Maxwell A and Jackson E segments (Hampton, in prep.). In particular, this new data suggests that the Jackson E and Maxwell A segments are associated with flows from the Wapshilla Ridge member, whereas the Jackson A segment has a distinctly non-Wapshilla composition. Preliminary assessments suggest that the Jackson A segment may be associated with the Meyer Ridge member (see Figure 2.1 for list of members), but this connection is not definite. If this geochemical correlation holds true, then the Jackson E and Maxwell A segments were emplaced first and followed by the emplacement of the Jackson A segment.

Despite being emplaced during the same eruptive event and despite being spatially close (~0.6 km apart), the Jackson E dike segment has a considerably wider thermal imprint than the Maxwell A dike. In this section, I explore two explanations for the apparently different thermal imprints between the Jackson E and Maxwell A segments: (1) magma focusing along strike, and (2) variations in heat advection due to different amounts of hydrothermal activity along strike.

Magma focusing. Magma focusing has been observed during modern effusive eruptions of basalt, where fissures begin as linear features, but eventually experience flow localization to a single point source (e.g. Mauna Ulu in Hawaii, Jones et al., 2017; 1973 eruption on Heimaey, Iceland, Thorarinsson et al., 1973). This focusing behavior occurs when a dike's convective flow regime shifts from chaotic mingling to viscosity-dependent fingering (Jones and Llewellin, 2021). In the viscosity-dependent fingering flow regime, temperature gradients develop along the strike of the dike. In the cooler sections of the dike, viscosity increases and drag forces develop, which causes magma flow to wane; in the higher temperature sections of the dike, viscosity decreases and magma flow is localized to the upwelling fingers (Helfrich, 1995; Wylie et al., 1999; Jones and Llewellin, 2021). For modern fissure eruptions, localization of magma flow usually occurs over the span of hours and is followed by sustained flow at the main fissure for months (Wylie et al., 1999; Jones et al., 2017).

Although the flow localization studies mentioned above focused on smaller, modern dikes (0.1-3 m wide), these processes may still be relevant for larger, flood basalt dikes. For example, eruptions in the CRFBs are interpreted to be "Hawaiian" style, with vent fissures erupting lava fountains and then inflated pahoehoe flows (Reidel and Tolan, 1992). Additionally, the Roza vent system of the CRFBs is estimated at 180 km in length (Brown et al., 2014), but the high estimated eruptive rates for the Roza member (~1000 m^3/s) suggests that only part of the 180 m long fissure were active at a time (i.e., magma focusing along strike; Thordarson and Self, 1998). However, there is no consensus on the timescale of magma focusing for a typical LIP vent system, such as the Roza vents.

Now, considering just the Jackson E and Maxwell A dike segments, the difference between thermal imprints at these two segments may be indicative of vastly different magma flow durations, thus suggesting an element of magma focusing at the Jackson E segment. However, according to Bruce and Huppert (1990), either solidification or partial melting at a dikes' margin contributes to a positive feedback that results in either dike blocking or sustained flow, respectively. However, because both the Jackson E and Maxwell A segments have partially melted granite at their margins, I would interpret that both segments were likely the sites of magma focusing. As such, the magma focusing hypothesis may be insufficient to explain the variable thermal imprints recorded by thermochronology next to these two segments.

Hydrothermal interaction. Another possible explanation for differences in thermal imprints next to the Jackson E and Maxwell A segments is the circulation of hydrothermal fluids. The isotopic exchange of rocks with meteoric fluids has been documented across Earth's history; for example, the Eocene Idaho batholith (Criss and Taylor, 1983), Archean rocks from North China Craton (Wan et al., 2013), Tertiary plutons from Isle of Skye, Scotland (Forester and Taylor, 1977; Gilliam and Valley, 1997) and Paleoproterozoic Belomorian Belt rocks from Karelia, Russia (Bindeman and Serebryakov, 2011) have all been noted for their extreme oxygen isotope ($\delta^{18}O$) signatures, which are characteristic of interaction with groundwater.

During dike emplacement, transient high temperatures can drive convective cells in meteoric fluids in the surrounding wallrocks. This increased mobility of water and heat facilitates isotopic exchange between the lower $\delta^{18}O$ fluids and the higher $\delta^{18}O$ wallrocks (Bickle and McKenzie, 1987). This isotopic phenomenon was documented next to Jackson A dike by Bindeman et al. (2020), and used to model heat transfer next to the dike. This study demonstrated that the advective heat component, in addition to conductive heating, results in higher predicted peak temperatures at farther distances from the dike. As such, more hydrothermal interaction during dike emplacement should result in wider zones of reset thermochronologic ages.

The different thermal imprints next to the Jackson E and Maxwell A segments may be the result of spatially variable fracture patterns (and therefore permeability) in the surrounding wallrock granites. Larger fracture networks next to a dike should result in a significant hydrothermal component and increased heat advection, which would ultimately contribute to wider zones of resetting next to the dike. Recent oxygen isotope analysis (Hampton, in prep) at these dike segments shows that the Jackson E segment is severely depleted in $\delta^{18}O$ (VSMOW), with average $\delta^{18}O$ values of 2.5‰ in the dike and values of 1.8‰ in the partially melted granite. In comparison, the Maxwell A segment showed less depleted average $\delta^{18}O$ values of 6.3‰ and 6.1‰ for the dike interior and partial melt, respectively. These analyses suggest that the Jackson E segment had more interaction with hydrothermal fluids during emplacement, and the circulation of these fluids may have contributed to increased heat flow through advection and, ultimately, a larger thermal imprint as recorded by thermochronometers in the wallrocks.

Future work can test these oxygen isotope observations using the modeling approach outlined in Ch. 3. A closer focus on the thermal conductivity parameter (k) could help differentiate whether wider reset zones are truly the result of different dike longevities or hydrothermal interaction, where values for k that are greater than those of typical dry upper-crustal rock can be used as a proxy for increased heat flow due to advection of fluids.

4.5 Conclusions

We measured thermochronologic resetting next to three dikes in the Maxwell Lake area of the Wallowa Mountains in order to compare their dike emplacement histories. Once normalized to dike width, the Jackson A and Jackson E segments have similar widths of thermal imprints, and the Maxwell A dike segment has a very narrow thermal imprint. These relationships suggest that either the Maxwell A dike segment did not heat rocks as significantly as the Jackson A or Jackson E dike segments, or that the adjacent wallrocks did not conduct heat as efficiently as the Jackson A and Jackson E dike segments. Geochemical analysis (Hampton, in prep) shows that the Jackson A segment likely fed the Meyer Ridge member of the Grande Ronde eruptive phase, whereas the Jackson E and Maxwell A segments fed the Wapshilla Ridge member. These differences between thermal imprints for the Jackson E and Maxwell A segments suggest that either differing magma flow durations (due to magma focusing) or differing levels of hydrothermal interaction during emplacement were the main influences on fractional resetting next to these dikes.

Chapter 4 Figures and Tables

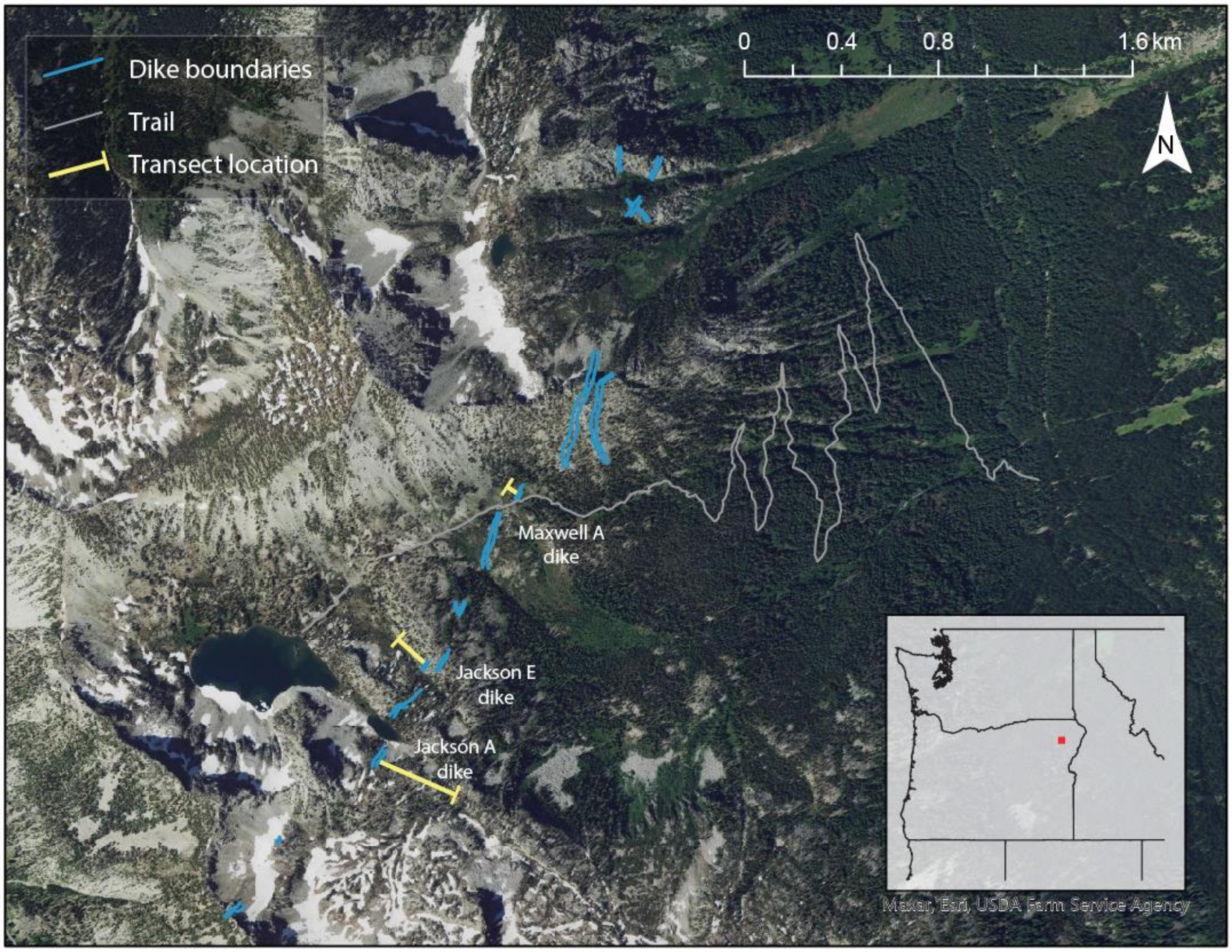

Figure 4.1– Map of dike segments exposed in the Maxwell Lake area. Yellow lines show thermochronology transects for the three segments studied here. Mapped dikes after Hampton (in prep).

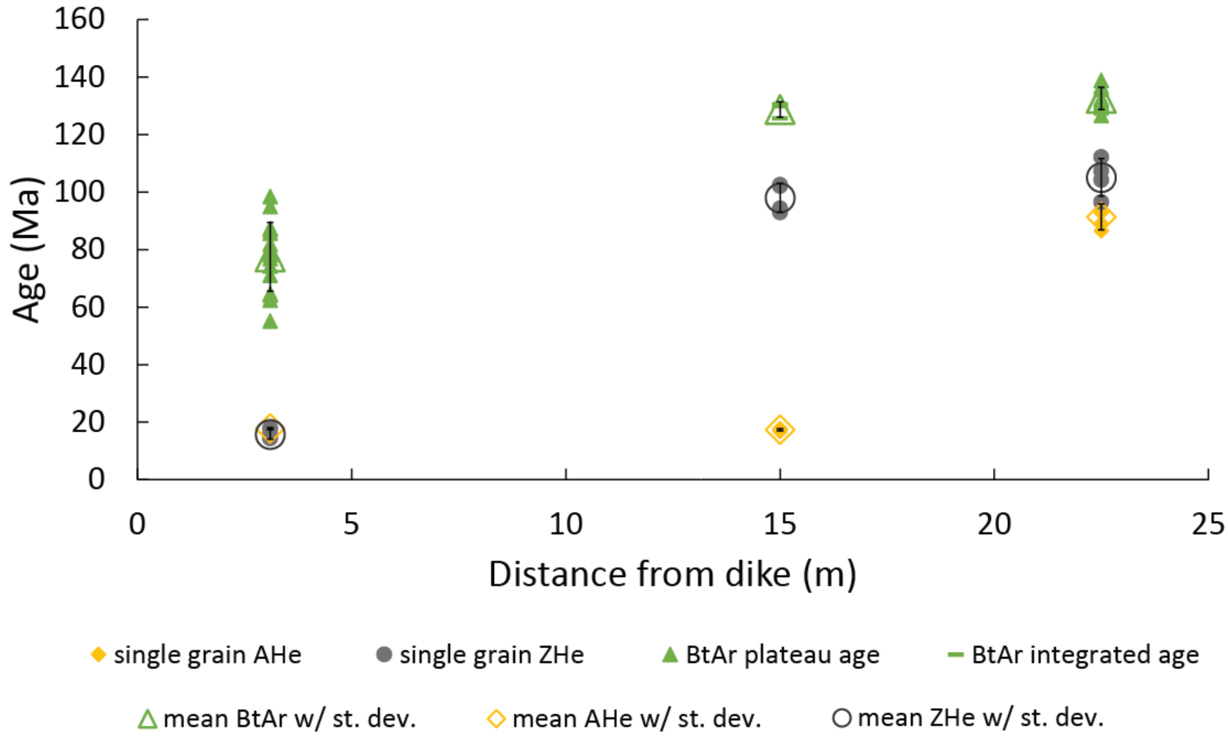

Figure 4.2– Cooling ages for Maxwell A dike transect. AHe– apatite (U-Th)/He, ZHe– zircon (U-Th)/He, BtAr– biotite $^{40}Ar/^{39}Ar$.

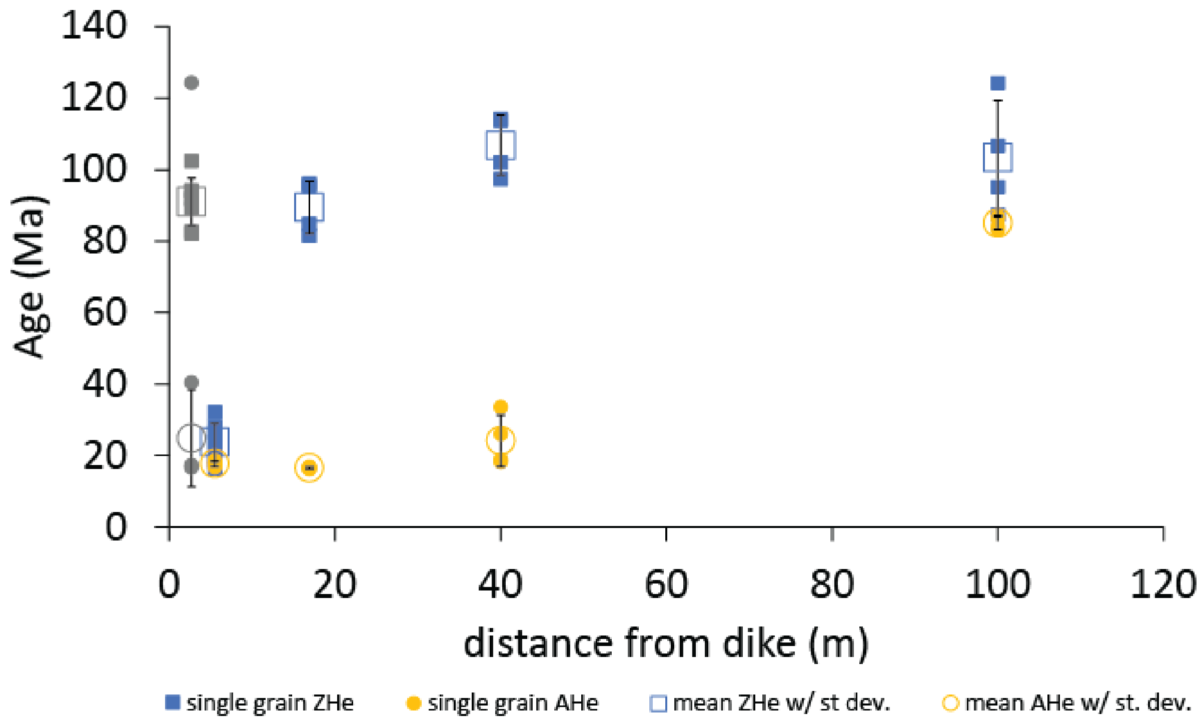

Figure 4.3– Cooling ages for Jackson E dike transect. Grayed out samples are considered “float” and are excluded during analysis. AHe– apatite (U-Th)/He and ZHe– zircon (U-Th)/He.

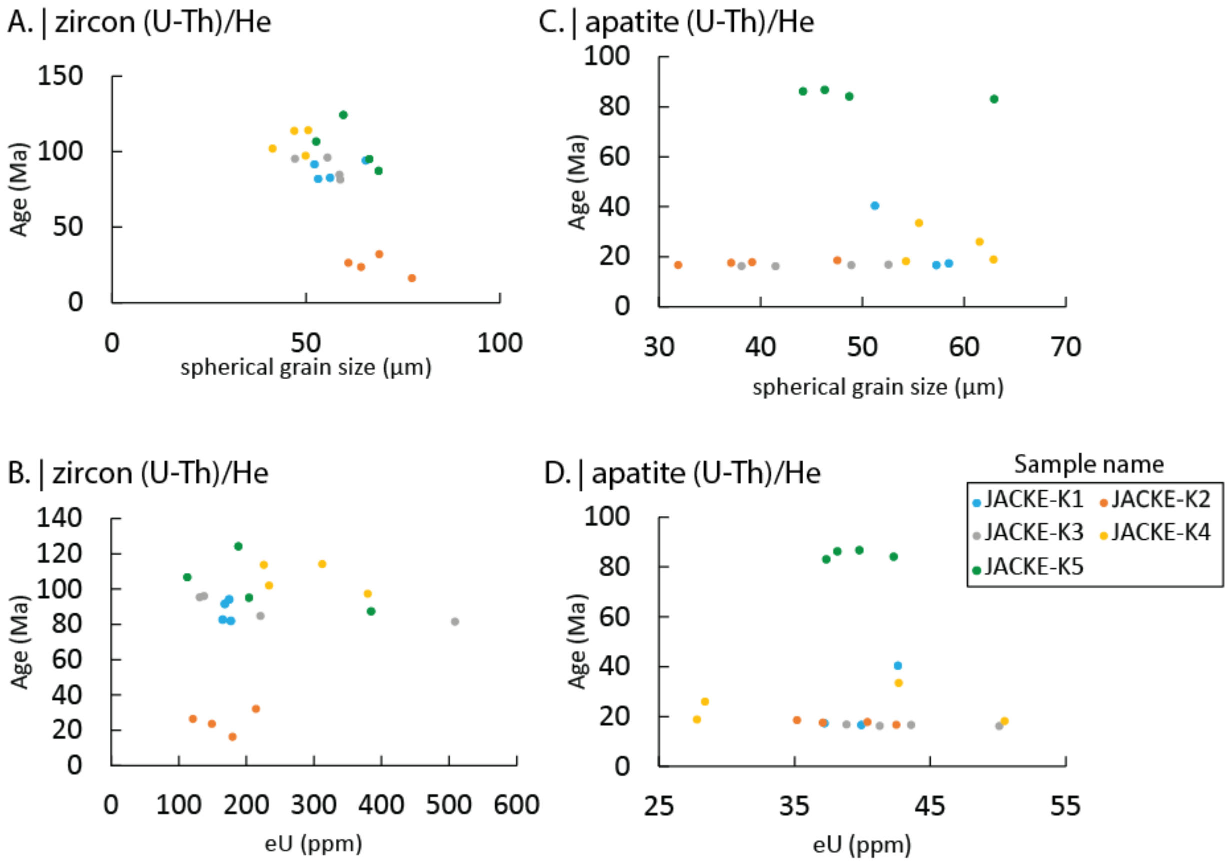

Figure 4.4– Age vs. eU and age vs. grain size graphs for the Jackson E transect: (A) age vs. grain size graph for zircon (U-Th)/He, (B) age vs. eU for zircon (U-Th)/He, (C) age vs. grain size graph for apatite (U-Th)/He, (D) age vs. eU for apatite (U-Th)/He.

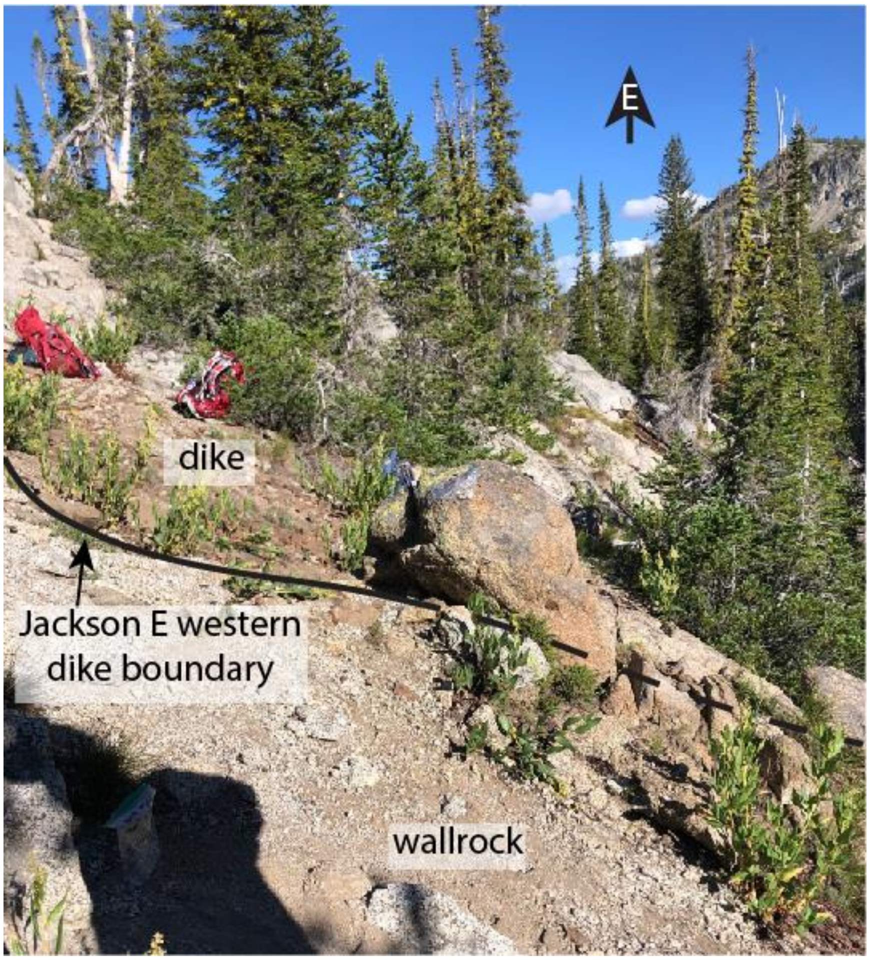

Figure 4.5—Photo of the western side of the Jackson E dike-wallrock contact where the thermochronologic transect was taken. View is looking towards the East. Photo taken by R. Hampton 2020.

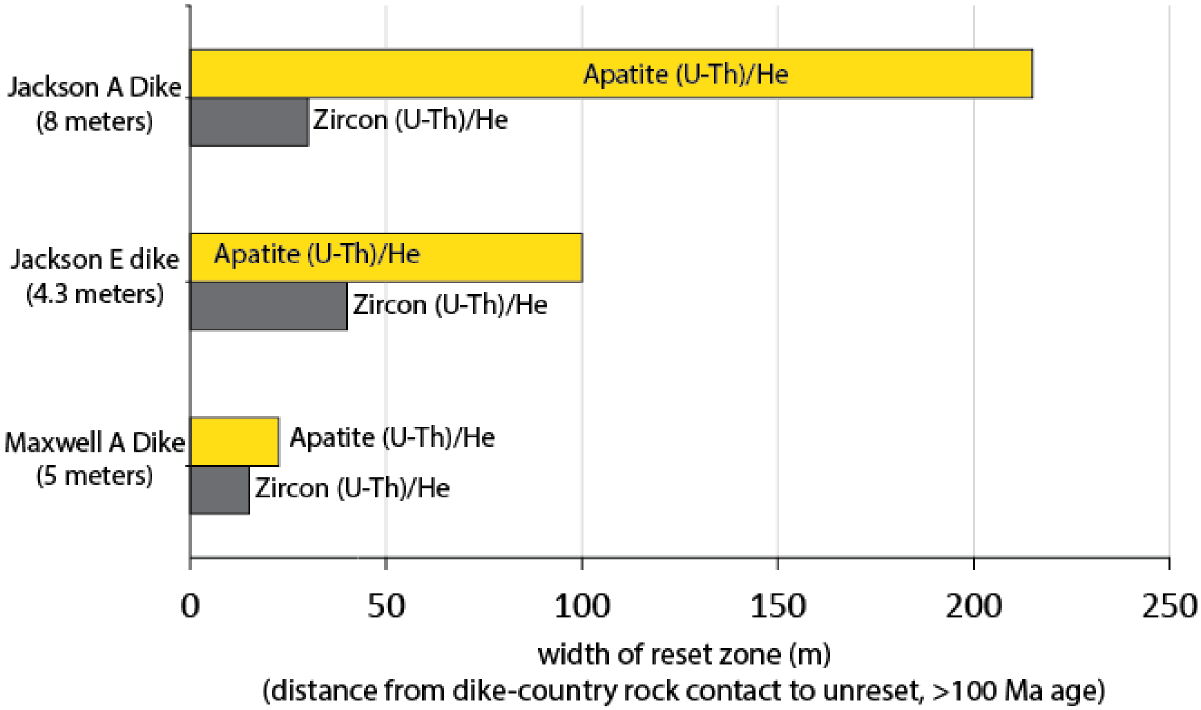

Figure 4.6– Comparison of resetting widths for apatite and zircon (U-Th)/He between the Jackson A, Jackson E, and Maxwell A dike segments. Resetting width is defined as the distance from the dike boundary to the first unreset age. Dike thickness listed in parentheses below dike name.

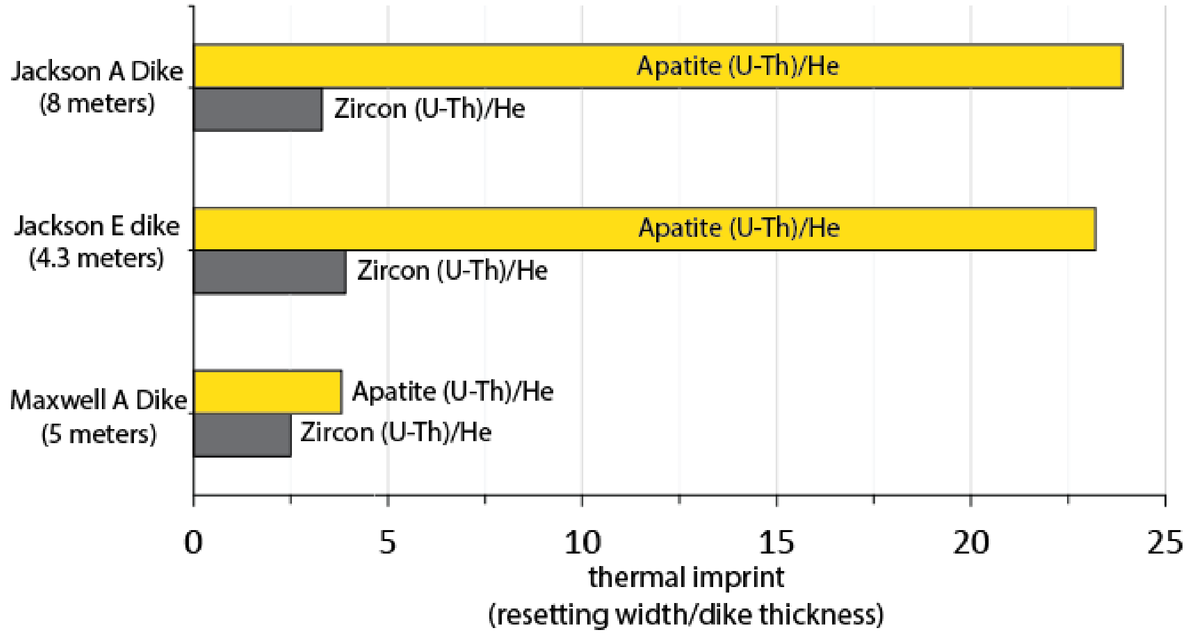

Figure 4.7– Comparison of thermal imprints (resetting width/dike thickness) for apatite and zircon (U-Th)/He between Jackson A, Jackson E, Maxwell A dike segments. Dike thickness listed in parentheses below dike name.

Table 4.1—Apatite He data from the Maxwell Lake Area.

Sample ID	distance from dike	# of apatites analyzed	Avg. AHe Corrected Age	SD	AHe Age Dispersion	dike segment
	m		*Ma*	*Ma*	*SD/Avg (Ma)*	
2E1	2	4	14.6	0.4	0.03	Jackson A
2E2	5	4	16	1.3	0.08	Jackson A
2E3	11	4	15	1.0	0.07	Jackson A
2E4	20.5	4	15.5	0.7	0.05	Jackson A
2E5	30	4	16	1.3	0.08	Jackson A
2E6	40	3	14.8	0.6	0.04	Jackson A
2E7	53.5	4	15.2	0.8	0.05	Jackson A
2E8	72.5	4	24	12.0	0.50	Jackson A
2E9	100	3	45	4.4	0.10	Jackson A
20JACK-K1	215	4	86	5.8	0.07	Jackson A
20JACKE-K1	2.7	3	25	13.5	0.55	Jackson E
20JACKE-K2	5.5	4	17.7	0.8	0.04	Jackson E
20JACKE-K3	16.9	4	16.5	0.3	0.02	Jackson E
20JACKE-K4	40	4	24	7.2	0.30	Jackson E
20JACKE-K5	100	4	85	1.7	0.02	Jackson E
20MAX-K1	3.1	4	17.9	0.3	0.02	Maxwell A
20MAX-K2	15	4	17.4	0.4	0.02	Maxwell A
20MAX-K3	22.5	4	91	4.5	0.05	Maxwell A

SD- standard deviation (1s)

Table 4.2—Zircon He data from the Maxwell Lake Area.

Sample ID	distance from dike	# of zircons analyzed	Avg. ZHe Age	SD	ZHe Age Dispersion	dike segment
	m		*Ma*	*Ma*	*SD/Avg (Ma)*	
2E1	2	3	15.6	0.3	0.02	Jackson A
2E2	5	3	44	11.9	0.27	Jackson A
2E3	11	3	57	16.2	0.28	Jackson A
2E4	20.5	3	67	32.8	0.49	Jackson A
2E5	30	3	107	10.5	0.10	Jackson A
2E6	40	3	114	4.0	0.04	Jackson A
2E7	53.5	3	116	8.4	0.07	Jackson A
2E8	72.5	3	115	4.4	0.04	Jackson A
2E9	100	3	110	14.3	0.13	Jackson A
20JACK-K1	215	4	94	12.2	0.13	Jackson A
20JACKE-K1	2.7	8	91	6.6	0.07	Jackson E
20JACKE-K2	5.5	8	24	5.2	0.22	Jackson E
20JACKE-K3	16.9	4	89	7.4	0.08	Jackson E
20JACKE-K4	40	4	107	8.4	0.08	Jackson E
20JACKE-K5	100	4	103	16.0	0.16	Jackson E
20MAX-K1	3.1	4	16	1.6	0.10	Maxwell A
20MAX-K2	15	4	98	5.0	0.05	Maxwell A
20MAX-K3	22.5	4	105	6.6	0.06	Maxwell A

SD- standard deviation (1s)

Table 4.3—Biotite $^{40}Ar/^{39}Ar$ data from the Maxwell Lake Area.

Sample ID	distance from dike *m*	type of analysis	number of analyses	Avg. BtAr Age *Ma*	SD *Ma*	BtAr Age Dispersion *SD/Avg (Ma)*	dike segment
2E1	2	step-heating	10	34	6.8	0.20	Jackson A
2E2	5	single step fusion	2	123.9	0.3	0.00	Jackson A
2E3	11	single step fusion	6	125	5.0	0.04	Jackson A
2E4	20.5	single step fusion	3	125.0	0.5	0.00	Jackson A
2E5	30	step-heating	7	126	1.2	0.01	Jackson A
2E6	40	single step fusion	3	122	6.2	0.05	Jackson A
2E7	53.5	single step fusion	3	122	3.0	0.02	Jackson A
2E8	72.5	single step fusion	3	127	1.3	0.01	Jackson A
2E9	100	single step fusion	3	123	3.3	0.03	Jackson A
20JACK-K1	215	single step fusion	9	126	2.8	0.02	Jackson A
20MAX-K1	3.1	step-heating	16	78	11.9	0.15	Maxwell A
20MAX-K2	15	single step fusion	3	129	2.7	0.02	Maxwell A
20MAX-K3	22.5	step-heating	9	133	3.9	0.03	Maxwell A

SD- standard deviation (1s)

Chapter 5: Hydrogen Isotopes in Apatite as a Potential Tool for Documenting Dike-Generated Hydrothermal Circulation

5.1 Introduction

As discussed in Chapter 4, the circulation of hydrothermal fluids during dike emplacement may result in wider zones of resetting next to dikes. Although most studies use oxygen isotopes ($\delta^{18}O$) as a proxy for fluid flow in igneous rocks (Criss and Taylor, 1983; Forester and Taylor, 1977; Gilliam and Valley, 1997; Bindeman and Serebryakov, 2011; Wan et al., 2013), here I attempt to use hydrogen isotopes (δD) in apatite (Greenwood, 2018) to measure fluid flow next to Columbia River Flood Basalt (CRFB) feeder dikes. Apatite is a phosphate mineral that can substitute a F^-, Cl^-, or OH^- ion into its crystal lattice. Varieties that substitute an OH group, called hydroxyapatites, should record magmatic hydrogen isotopic signatures if they have not been altered after magmatic hydration. However, increases in rock temperature can mobilize meteoric waters and initiate the exchange of ions between bedrock minerals and the circulating low-δD waters, thus resulting in low-δD signatures in apatite crystals. To test the efficacy of an apatite δD proxy for hydrothermal circulation, I measured apatite δD values along the Karlstrom et al. (2019) thermochronology transect and attempt to match isotopic patterns from my analyses to existing $\delta^{18}O$ data from Bindeman et al. (2020) next to the Jackson A dike segment.

Bindeman et al. (2020) took 23 samples in a transect across both sides of the Jackson A dike segment and analyzed $\delta^{18}O$ in materials susceptible to fluid alteration (plagioclase, magnetite, biotite, and quenched melt) and materials resistant to alteration (quartz, pyroxene, and amphibole). Next to the Jackson A segment, quartz had unaltered $\delta^{18}O$ values of 8.5-9‰, whereas plagioclase had very low $\delta^{18}O$ values (~2.5- 4‰) up to 25 m from the dike and moderately low $\delta^{18}O$ values (6.5-7‰) between 25 and 100 m away from the dike. Bindeman et al. (2020) then used this oxygen isotope data to model heat transfer during dike emplacement, which suggests hydrothermal circulation of fluids up for ~150 years following magma flow shut off.

The primary goal of this study is to be able to use apatite δD to determine the extent of hydrothermal interaction next to dikes. Because apatite is already widely used as a low-temperature thermochronometer, this additional isotopic application would increase access to information regarding thermally mobilized groundwater—information that has previously been limited to quartz and plagioclase $\delta^{18}O$ proxies. In particular, thermochronologic applications that use perpendicular-to-dike transects to model dike emplacement histories (e.g., Karlstrom et al., 2019; this study) will be able to generate both thermochronologic ages and δD signatures from the same set of apatite mineral separates. This dual application of apatite geochemistry will provide important context for thermal models by determining the significance of a convective heat transfer mechanism during dike emplacement.

5.2 Methods

I measured δD in apatite at nine locations next to the Jackson A dike segment.
I used the same mineral separates that were used for apatite (U-Th)/He analysis by Karlstrom et al. (2019) and the same samples that were used for $\delta^{18}O$ analysis by Bindeman et al. (2020) for my δD measurements. All δD values have a standard deviation of 3‰. The method for measuring apatite δD published by Greenwood (2018) recommends using ~40 mg of bulk apatite to produce a sufficient isotopic signal during mass spectrometer analysis; however, due to a limited supply of apatite crystals for each sample and the need for replicate measurements, I used only half of the suggested mass of apatite (A. Abbey, personal comm.). As such, I packaged ~20

mg of bulk apatite for each sample into silver sample packets. For samples with larger apatite yields, I packaged duplicate and triplicate packets. My methodology also differed from that of Greenwood (2018) in that I did not crush and sieve my bulk apatite crystals, in order to preserve the limited quantity of material. In order to ensure evaporation of excess surface water, all packets were stored in a desiccator before being held in a 400°C furnace for an hour immediately prior to analysis.

After cooling in a glass desiccator for 20 minutes, all samples and standards were loaded into a Zero Blank autosampler and purged with helium for 30 minutes. I used several international and lab standards, including Linopolis and Durango RR apatites from Greenwood (2018) and ISU kaolinite for size correction. All samples and standards were analyzed using a High Temperature Conversion Elemental Analyzer reactor set at 1450°C.

5.3 Results

The 20 mg sample size used for analysis was not sufficient for generating a strong mV signal. Ideally, signals are >1000 mV, whereas the 20 mg samples produced signals between 425-769 mV. However, using the kaolinite size correction, I was able to correct for the small sample size. Compared to the δD value for typical igneous rocks (-85‰; Taylor, 1978), all samples in this transect were depleted, with values ranging from -124‰ to -111‰ (Figure 5.1). I exclude analysis of sample 2E9-2 from my interpretation, as this sample generated the smallest signal (425 mV) and produced an anomalously low δD value (-130‰). Average values for each sample show a pattern of extremely depleted (-123‰ to -121‰) δD values <20 m from the dike, and moderately depleted (-114‰ to -111‰) values >20 m from the dike (Table 5.1).

5.4 Discussion and Further Work

Based on the small sample sizes used and the lack of triplicate measurements at all samples, I provide only preliminary interpretations here. The observed pattern of δD depletion mirrors the pattern of $\delta^{18}O$ depletion measured by Bindeman et al. (2020). $\delta^{18}O$ values next to the Jackson A dike reach peak depletion <15 m from the dike and then stabilize at moderately depleted values up to 100 m from the dike (Figure 5.1). The congruence of δD values measured in this study with the $\delta^{18}O$ dataset suggests a shared secondary hydrothermal origin for the depletion of both systems. Figure 5.2 shows how δD values compare to apatite and zircon (U-Th)/He ages next to the Jackson A dike.

Although these data suggest that the numerical model used in Ch. 3 may be incomplete in that it lacks an advective heat transport component during dike emplacement, the parameterization of thermal conductivity helps mitigate this issue. In particular, results from numerical modeling of thermochronologic cooling ages in Ch. 3 did not constrain wallrock thermal conductivity, but rather suggested that thermochronometer resetting patterns could be fit by a wide range of thermal conductivities (1.26-8.78 W/m°C; Table 3.3). Although some of these predicted thermal conductivities are higher than normal thermal conductivities for dry granites (2-4 W/m°C; Dalla Santa et al., 2020), it is still unclear to what extent this added heat transport mechanism influences the resetting of thermochronometers next to a dike. Further investigation of fluid flow proxies next to Jackson E and Maxwell A dike will elucidate whether shorter resetting widths can be solely explained through increased hydrothermal interaction, or if they truly require longer magma flow durations.

Chapter 5 Figures and Tables

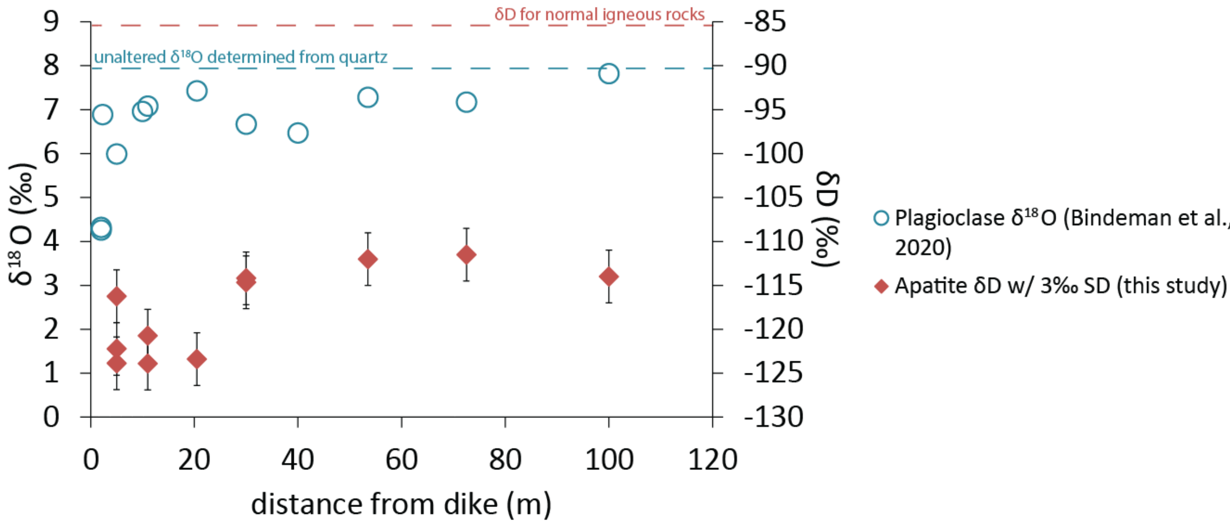

Figure 5.1—Apatite δD data (red; this study) compared to plagioclase $\delta^{18}O$ data (Bindeman et al., 2020) measured next to the Jackson A dike segment. Standard deviation for $\delta^{18}O$ is smaller than the symbols used here (0.1‰). Standard deviation is 3‰ for δD.

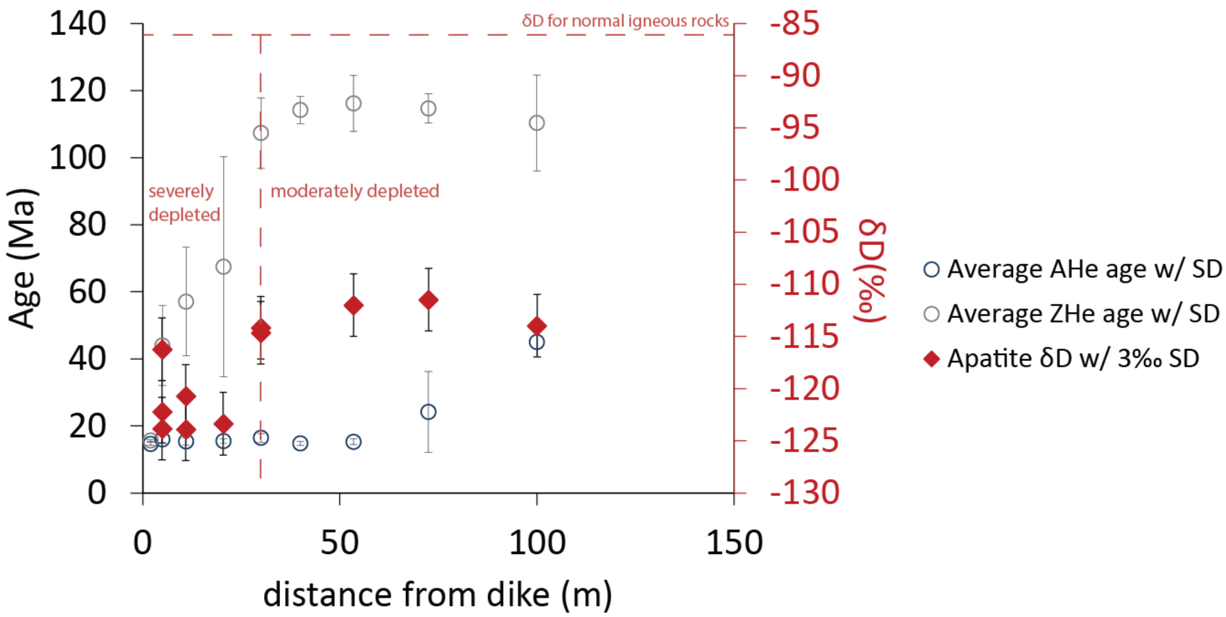

Figure 5.2— Apatite δD data (red) compared to average apatite and zircon (U-Th)/He (AHe, ZHe) data from the Jackson A transect. Standard deviation for δD is 3‰.

Table 5.1—Apatite δD values for Jackson A transect

Sample ID	distance from dike	Weight	Ampl 2	δD VSMOW	Amt%	Delta area	δD VSMOW (size corrected)
	m	*mg*	*mV*	‰			‰
2E2-1	5	20.039	542	-118.43	0.02	-23.215	**-122.23**
2E2-2	5	19.919	528	-119.97	0.02	-23.355	**-123.86**
2E2-3	5	38.502	1314	-117.18	0.02	-6.382	**-116.26**
2E3-1	11	20.023	476	-116.16	0.02	-24.459	**-120.73**
2E3-2	11	20.043	500	-119.50	0.02	-24.209	**-123.92**
2E4	20.5	20.299	769	-121.53	0.02	-19.475	**-123.39**
2E5-1	30	19.58	630	-111.75	0.02	-21.621	**-114.66**
2E5-2	30	19.623	618	-111.22	0.02	-21.715	**-114.19**
2E7-1	53.5	20.058	712	-109.84	0.02	-20.173	**-112.03**
2E8-1	72.5	20.254	772	-109.22	0.02	-20.382	**-111.51**
2E9-1	100	19.857	544	-111.09	0.02	-21.602	**-114.00**
2E9-2	100	19.773	425	-127.44	0.02	-22.707	**-130.95**

Chapter 6: Conclusions

The overarching goal of this study was to determine how long individual Columbia River Flood Basalt (CRFB) lava flows were active. To address this goal, I interrogated the wallrocks that host the magmatic conduits (i.e., dikes) that fed CRFB lava flows using fractional resetting of thermochronometers and hydrogen isotopic signatures to measure the thermal imprints of these magmatic intrusions. In particular, I collected 22.5-215 m sample transects next to three different dikes in the Maxwell Lake area of the Wallowa Mountains, OR in order to assess the spatial distribution of biotite $^{40}Ar/^{39}Ar$ (BtAr), zircon (U-Th)/He (ZHe), apatite (U-Th)/He (AHe), and apatite fission track (AFT) and hydrogen isotope depletion in the mineral apatite.

First, I use a conductive heating model paired to a fractional resetting model (Karlstrom et al., 2019) to run a Bayesian MCMC inversion of dike emplacement parameters and thermochronologic kinetics based on BtAr, ZHe, AHe, and ZHe ages sampled next to the Jackson A dike, which may have supplied magma to the Meyer Ridge member (~620 km^3) of the Grande Ronde Formation (Ch. 3). The questions motivating my modeling were twofold: (1) which thermochronologic system(s) are most useful for modeling the duration of magma flow through a dike? (2) can the model resolve a single thermal history while trying to fit four different thermochronologic datasets at once? This first question was answered using Akaike and Bayesian Information Criteria to compare three different scenarios for modeling thermochronologic data (high-temperature chronometers—BtAr and ZHe, low-temperature chronometers—AHe and AFT, and all chronometers—ZHe, BtAr, AHe, and AFT). Using the AIC/BIC index, I determined that modeling dike emplacement using scenario 2 (low-temperature chronometers) most effectively characterized magma flow duration at the Jackson A dike. The scenario 2 model predicted total flow durations between 3.8-11.3 years, with a median of 6.3

years (Figure 3.13A). To answer the second question motivating my research, I jointly modeled all four chronometers at once (scenario 3), so that the model would need to fit each dataset simultaneously. I determined that this approach is successful in producing a good fit to the observed data, despite complexities in the kinetics of those systems. In general, the results of the modeling scenarios independently supports each other, as the median best fit values for each scenario are within the 68% confidence intervals of each other scenario (Figure 3.21).

Next, I used thermochronology to compare thermal imprints between three different dike segments in the Maxwell Lake area of the Wallowa Mountains (Ch. 4). These three dike segments (the Jackson A, Jackson E, and Maxwell A segments) are aligned along strike (~N20°E), but only the Jackson E and Maxwell A dikes are interpreted to be related, as both of those segments have geochemical compositions associated with the Wapshilla Ridge member of the Grande Ronde Formation. To compare the widths of each dikes' thermal imprint, I measured distance from the dike margin to the first non-reset age, and then normalize that distance to the width of the dike segment. Because the Jackson E and Maxwell A dike segments both fed the Wapshilla Ridge member, and these two segments are only 500 m away from each other, it was hypothesized that the thermal imprint around each segment would be similar; however, the Jackson E and Maxwell A segments do not have similar thermal imprints. The Jackson A and Jackson E segments showed similar widths of thermal imprints (ZHe: 3.3 and 3.9; AHe: 23.9 23.2, respectively), but the thermal imprint around the Maxwell A segment was considerably narrower (ZHe: 2.5; AHe: 3.8). I hypothesize two processes to explain the different widths of thermal imprints between the Jackson E and Maxwell A segments: (1) magma focusing at the Jackson E segment, and (2) increased interaction with hydrothermal fluids next to the Jackson E segment. Further research should attempt to model the duration of magma flow next to more dike segments in the Maxwell Lake area, in order to better characterize surface flow eruption durations.

Finally, I measured apatite hydrogen isotopes (δD) in a transect away from the Jackson A dike to identify the extent of hydrothermal circulation during dike emplacement. Apatite δD ranged from -124‰ to -111‰, which is depleted relative to unaffected igneous rocks (-85‰; Taylor, 1978). Additionally, values were lowest within 20 m of the dike, which corroborates with oxygen isotope values from the same samples measured by Bindeman et al. (2020). These depletions suggest that there was an element of hydrothermal circulation operating during dike emplacement; however, it is unclear to what extent this fluid interaction contributed to advective heat transport, and how that additional heat transfer mechanism might affect thermochronologic ages observed next to a dike.

References

Akaike, H., 1974, A new look at the statistical model identification: IEEE Transactions on Automatic Control, v. AC-19, doi:10.1007/978-1-4612-1694-0_16.

Anderson, K.R., and Poland, M.P., 2016, Bayesian estimation of magma supply, storage, and eruption rates using a multiphysical volcano model: Kīlauea Volcano, 2000–2012: Earth and Planetary Science Letters, v. 447, p. 161–171, doi:10.1016/J.EPSL.2016.04.029.

Biasi, J., and Karlstrom, L., 2021, Timescales of magma transport in the Columbia River flood basalts, determined by paleomagnetic data: Earth and Planetary Science Letters, v. 576, doi:10.1016/J.EPSL.2021.117169.

Bickle, M.J., and McKenzie, D., 1987, The transport of heat and matter by fluids during metamorphism: Contributions to Mineralogy and Petrology, v. 95, p. 384–392, doi:10.1007/BF00371852.

Bindeman, I.N., Greber, N.D., Melnik, O.E., Artyomova, A.S., Utkin, I.S., Karlstrom, L., and Colón, D.P., 2020, Pervasive hydrothermal events associated with large igneous provinces documented by the Columbia River Basaltic Province: Scientific Reports, v. 10, p. 1–9, doi:10.1038/s41598-020-67226-9.

Bindeman, I.N., and Serebryakov, N.S., 2011, Geology, Petrology and O and H isotope geochemistry of remarkably 18O depleted Paleoproterozoic rocks of the Belomorian Belt, Karelia, Russia, attributed to global glaciation 2.4 Ga: Earth and Planetary Science Letters, v. 306, p. 163–174, doi:10.1016/J.EPSL.2011.03.031.

Black, B.A., Karlstrom, L., and Mather, T.A., 2021, The life cycle of large igneous provinces: Nature Reviews Earth and Environment, v. 2, p. 840–857, doi:10.1038/S43017-021-00221-4.

Bond, D.P.G., and Wignall, P.B., 2014, Large igneous provinces and mass extinctions: An update, *in* Keller, G. and Kerr, A.C. eds., Volcanism, Impacts, and Mass Extinctions: Causes and Effect: Geological Society of America Special Paper 505, doi:10.1130/2014.2505(02).

Brown, R.J., Blake, S., Thordarson, T., and Self, S., 2014, Pyroclastic edifices record vigorous lava fountains during the emplacement of a flood basalt flow field, Roza Member, Columbia River Basalt Province, USA: GSA Bulletin, v. 126, doi:10.1130/B30857.1.

Bruce, P., and Huppert, H., 1990, Solidification and melting along dykes by the laminar flow of basaltic magma, *in* Ryan, M.P. ed., Magma Transport and Storage, John Wiley & Sons, Ltd.

Bruce, P.M., and Huppert, H.E., 1989, Thermal control of basaltic fissure eruptions: Nature 1989 342:6250, v. 342, p. 665–667, doi:10.1038/342665a0.

Bryan, S.E., and Ernst, R.E., 2008, Revised definition of Large Igneous Provinces (LIPs): Earth-Science Reviews, v. 86, p. 175–202, doi:10.1016/j.earscirev.2007.08.008.

Burgess, S.D., and Bowring, S.A., 2015, High-precision geochronology confirms voluminous magmatism before, during, and after Earth's most severe extinction: Science Advances, v. 1, doi:10.1126/sciadv.1500470.

Calk, L.C., and Naeser, C.W., 1973, The thermal effect of a basalt intrusion on fission tracks in quartz monzonite:, doi:10.1086/627834.

Chew, D.M., and Donelick, R.A., 2012, Combined apatite fission track and U-Pb dating by LA-ICPMS and its application in apatite provenance analysis, *in* Sylvester, P. ed., Quantitative Mineralogy and Microanalysis of Sediments and Sedimentary Rocks, Mineralogical Association of Canada Short Course.

Criss, R., and Taylor, H.J., 1983, An 18O/16O and D/H study of Tertiary hydrothermal systems in the southern half of the Idaho batholith: GSA Bulletin, v. 94.

Dalla Santa, G. et al., 2020, An updated ground thermal properties database for GSHP applications: Geothermics, v. 85, p. 101758, doi:10.1016/J.GEOTHERMICS.2019.101758.

Dalrymple, G.B., Clague, D.A., Garcia, M.O., and Bright, S.W., 1981, Petrology and K-Ar ages of dredged samples from Laysan Island and Northampton Bank volcanoes, Hawaiian Ridge, and evolution of the Hawaiian-Emperor chain: GSA Bulletin, v. 92, p. 884–933, doi:10.1130/GSAB-P2-92-884.

Dodson, M., 1973, Closure temperature in cooling geochronological and petrological systems: Contributions to Mineralogy and Petrology, v. 40, p. 259–274.

Ehlers, T.A. et al., 2005, Computational tools for low-temperature thermochronometer interpretation, *in* Reviews in Mineralogy and Geochemistry, Mineralogical Society of America, v. 58, p. 589–622, doi:10.2138/RMG.2005.58.22.

Flowers, R.M., Ketcham, R.A., Enkelmann, E., Gautheron, C., Reiners, P.W., Metcalf, J.R., Danišík, M., Stockli, D.F., and Brown, R.W., 2022, (U-Th)/He chronology: Part 2. Considerations for evaluating, integrating, and interpreting conventional individual aliquot data: GSA Bulletin, doi:10.1130/B36268.1.

Flowers, R.M., Ketcham, R.A., Shuster, D.L., and Farley, K.A., 2009, Apatite (U–Th)/He thermochronometry using a radiation damage accumulation and annealing model: Geochimica et Cosmochimica Acta, v. 73, p. 2347–2365, doi:10.1016/J.GCA.2009.01.015.

Forester, R.W., and Taylor, H.P., 1977, 18 O/ 16 O, D/H, and 13 C/ 12 C studies of the Tertiary igneous complex of Skye, Scotland: American Journal of Science, v. 277, p. 136–177, doi:10.2475/AJS.277.2.136.

Galbraith, R.F., and Laslett, G.M., 1993, Statistical models for mixed fission track ages: Nuclear Tracks and Radiation Measurements, v. 21, p. 459–470, doi:10.1016/1359-0189(93)90185-C.

Gautheron, C., and Zeitler, P.K., 2020, Noble gases deliver cool dates from hot rocks: Elements, v. 16, p. 303–309, doi:10.2138/GSELEMENTS.16.5.303.

Giletti, B., 1974, Studies in diffusion I: argon in phlogopite mica, *in* Hofmann, A.W. ed., Geochemical transport and kinetics: papers, Washington, Carnegie Institution of Washington, p. 107–115.

Gilliam, C.E., and Valley, J.W., 1997, Low δ18O magma, Isle of Skye, Scotland: Evidence from zircons: Geochimica et Cosmochimica Acta, v. 61, p. 4975–4981, doi:10.1016/S0016-7037(97)00297-4.

Greenwood, J.P., 2018, Hydrogen and D/H analysis of apatite by Elemental Analyzer-Chromium/High-Temperature Conversion-Isotope Ratio Mass Spectrometry (EA-Cr/HTC-IRMS): Chemical Geology, v. 500, p. 175–181, doi:10.1016/j.chemgeo.2018.09.029.

Hasebe, N., Barbarand, J., Jarvis, K., Carter, A., and Hurford, A.J., 2004, Apatite fission-track chronometry using laser ablation ICP-MS: Chemical Geology, v. 207, p. 135–145, doi:10.1016/J.CHEMGEO.2004.01.007.

Helfrich, K.R., 1995, Thermo-viscous fingering of flow in a thin gap: a model of magma flow in dikes and fissures: Journal of Fluid Mechanics, v. 305, p. 219–238, doi:10.1017/S0022112095004605.

Hurford, A.J., 2019, An historical perspective on fission-track thermochronology, *in* Malusà, M. and Fitzgerald, P. eds., Fission-Track Thermochronology and its Application to Geology, Springer, Cham, p. 3–23, doi:10.1007/978-3-319-89421-8_1.

Johnson, K., Barnes, C.G., and Miller, C.A., 1997, Petrology, geochemistry, and genesis of high-Al tonalite and trondhjemites of the Cornucopia stock, Blue Mountains, northeastern Oregon: Journal of Petrology, v. 38, p. 1585–1611, doi:10.1093/PETROJ/38.11.1585.

Jones, T.J., and Llewellin, E.W., 2021, Convective tipping point initiates localization of basaltic fissure eruptions: Earth and Planetary Science Letters, v. 553, p. 116637, doi:10.1016/J.EPSL.2020.116637.

Jones, T.J., Llewellin, E.W., Houghton, B.F., Brown, R.J., and Vye-Brown, C., 2017, Proximal lava drainage controls on basaltic fissure eruption dynamics: Bulletin of Volcanology, v. 79, p. 1–15, doi:10.1007/S00445-017-1164-2/FIGURES/11.

Kahn, M., Fayon, A.K., and Tikoff, B., 2020, Constraints on the post-orogenic tectonic history along the Salmon River suture zone from low-temperature thermochronology, western Idaho and eastern Oregon: Rocky Mountain Geology, v. 55, p. 27–54, doi:10.24872/RMGJOURNAL.55.1.27.

Karlstrom, L., Murray, K.E., and Reiners, P.W., 2019, Bayesian Markov-Chain Monte Carlo inversion of low-temperature thermochronology around two 8 − 10 m wide Columbia River Flood Basalt dikes: Frontiers in Earth Science, v. 7, doi:10.3389/feart.2019.00090.

Kasbohm, J., and Schoene, B., 2018, Rapid eruption of the Columbia River flood basalt and correlation with the mid-Miocene climate optimum: Science Advances, v. 4, p. 1–8, doi:doi:10.1126/sciadv.aat8223.

Ketcham, R.A., 2005, Forward and inverse modeling of low-temperature thermochronometry data: Reviews in Mineralogy and Geochemistry, v. 58, p. 275–314, doi:10.2138/RMG.2005.58.11.

Ketcham, R.A., Donelick, R.A., and Carlson, W.D., 1999, Variability of apatite fission-track annealing kinetics: III. Extrapolation to geological time scales: American Mineralogist, v. 84, p. 1235–1255, doi:10.2138/AM-1999-0903/MACHINEREADABLECITATION/RIS.

Kuiper, K.F., Deino, A., Hilgen, F.J., Krijgsman, W., Renne, P.R., and Wijbrans, J.R., 2008, Synchronizing rock clocks of earth history: Science, v. 320, p. 500–504, doi:10.1126/SCIENCE.1154339.

Min, K., Mundil, R., Renne, P.R., and Ludwig, K.R., 2000, A test for systematic errors in 40Ar/39Ar geochronology through comparison with U/Pb analysis of a 1.1-Ga rhyolite: Geochimica et Cosmochimica Acta, v. 64, p. 73–98, doi:10.1016/S0016-7037(99)00204-5.

Morriss, M.C., Karlstrom, L., Nasholds, M.W.M., and Wolff, J.A., 2020, The Chief Joseph dike swarm of the Columbia River flood basalts, and the legacy data set of William H . Taubeneck: Geosphere, v. 16, p. 1–25, doi:10.1130/GES02173.1.

Murray, K.E., Braun, J., and Reiners, P.W., 2018, Toward robust interpretation of low-temperature thermochronometers in magmatic terranes: Geochemistry, Geophysics, Geosystems, v. 19, p. 3739–3763, doi:10.1029/2018GC007595.

O’Sullivan, P.B., and Parrish, R.R., 1995, The importance of apatite composition and single-grain ages when interpreting fission track data from plutonic rocks: a case study from the Coast Ranges, British Columbia: Earth and Planetary Science Letters, v. 132, p. 213–224, doi:10.1016/0012-821X(95)00058-K.

Petcovic, H.L., and Dufek, J.D., 2005, Modeling magma flow and cooling in dikes: Implications for emplacement of Columbia River flood basalts: Journal of Geophysical Research, v. 110, doi:10.1029/2004JB003432.

Petcovic, H.L., and Grunder, A.L., 2003, Textural and thermal history of partial melting in tonalitic wallrock at the margin of a basalt dike, Wallowa Mountains, Oregon: Journal of

Petrology, v. 44, p. 2287–2312, doi:10.1093/petrology/egg078.
Reidel, S.P., 1998, Emplacement of Columbia River flood basalt: Journal of Geophysical Research: Solid Earth, v. 103, p. 27393–27410, doi:10.1029/97JB03671.
Reidel, S.P., Camp, V.E., Martin, B.S., and Tolan, T.L., 2013, The Columbia River flood basalt province: Stratigraphy, areal extent, volume, and physical volcanology, *in* Reidel, S.P., Camp, V.E., Ross, M.E., Wolff, J.A., Martin, B.S., Tolan, T.L., and Wells, R.E. eds., The Columbia River Flood Basalt Province: Geological Society of America Special Paper 497, p. 1–43, doi:10.1130/2013.2497(01).
Reidel, S.P., and Tolan, T.L., 1992, Eruption and emplacement of flood basalt: An example from the large-volume Teepee Butte Member, Columbia River Basalt Group: GSA Bulletin, v. 104.
Reidel, S.P., and Tolan, T.L., 2013, The Grande Ronde Basalt, Columbia River Basalt Group, *in* Reidel, S.P., Camp, V.E., Ross, M.E., Wolff, J.A., Martin, B.S., Tolan, T.L., and Wells, R.E. eds., The Columbia River Flood Basalt Province: Geological Society of America Special Paper 497, p. 117–153, doi:10.1130/2013.2497(05).
Reiners, P.W., 2009, Nonmonotonic thermal histories and contrasting kinetics of multiple thermochronometers: Geochimica et Cosmochimica Acta, v. 73, p. 3612–3629, doi:10.1016/j.gca.2009.03.038.
Reiners, P.W., 2005, Zircon (U-Th)/He thermochronometry: Reviews in Mineralogy and Geochemistry, v. 58, p. 151–179, doi:10.2138/RMG.2005.58.6.
Reiners, P.W., and Brandon, M.T., 2006, Using thermochronology to understand orogenic erosion: Annual Review of Earth and Planetary Sciences, v. 34, p. 419–466, doi:10.1146/annurev.earth.34.031405.125202.
Reiners, P.W., and Nicolescu, S., 2006, Measurement of parent nuclides for (U-Th)/He chronometry by solution sector ICP-MS: ARDHL Report 1,.
Renne, P.R., Swisher, C.C., Deino, A.L., Karner, D.B., Owens, T.L., and DePaolo, D.J., 1998, Intercalibration of standards, absolute ages and uncertainties in 40Ar/39Ar dating: Chemical Geology, v. 145, p. 117–152, doi:10.1016/S0009-2541(97)00159-9.
Schoene, B., Eddy, M.P., Samperton, K.M., Keller, C.B., Keller, G., Adatte, T., and Khadri, S.F.R., 2019, U-Pb constraints on pulsed eruption of the Deccan Traps across the end-Cretaceous mass extinction: Science, v. 363, p. 862–866, doi:10.1126/science.aau2422.
Schoettle-Greene, P., Duvall, A.R., and Crowley, P.D., 2022, Multiphase topographic and thermal histories of the Wallowa and Elkhorn Mountains, Blue Mountains Province, Oregon, USA: Tectonics, v. 41, doi:10.1029/2021TC006704.
Schwarz, G., 1978, Estimating the dimension of a model: The Annals of Statistics, v. 6.
Self, S., Thordarson, T., Keszthelyi, L., Walker, G.P.L., Hon, K., Murphy, M.T., Long, P., and Finnemore, S., 1996, A new model for the emplacement of Columbia River basalts as large, inflated Pahoehoe Lava Flow Fields: Geophysical Research Letters, v. 23, p. 2689–2692, doi:10.1029/96GL02450.
Self, S., Thordarson, T., and Widdowson, M., 2005, Gas Fluxes from Flood Basalt Eruptions: Elements, v. 1, p. 283–287, doi:10.2113/GSELEMENTS.1.5.283.
Shaw, H., and Swanson, D., 1970, Eruption and flow rates of flood basalts, *in* Gilmour, E. and Strading, D. eds., Proceedings of the Second Columbia River Basalt Symposium, Cheney, Eastern Washington State College Press, p. 271–299.
Shuster, D.L., and Farley, K.A., 2004, 4He/3He thermochronometry: Earth and Planetary Science Letters, v. 217, p. 1–17, doi:10.1016/S0012-821X(03)00595-8.

Sprain, C.J., Renne, P.R., Vanderkluysen, L., Pande, K., Self, S., and Mittal, T., 2019, The eruptive tempo of Deccan volcanism in relation to the Cretaceous-Paleogene boundary: Science, v. 363, p. 866–870, doi:10.1126/science.aav1446.
Tagami, T., and O'Sullivan, P.B., 2005, Fundamentals of fission-track thermochronology: Reviews in Mineralogy and Geochemistry, v. 58, p. 19–47, doi:10.2138/RMG.2005.58.2.
Taylor, H.P., 1978, Oxygen and hydrogen isotope studies of plutonic granitic rocks: Earth and Planetary Science Letters, v. 38, p. 177–210, doi:10.1016/0012-821X(78)90131-0.
Thorarinsson, S., Steinthórsson, S., Einarsson, T., Kristmannsdóttir, H., and Oskarsson, N., 1973, The eruption on Heimaey, Iceland: Nature, v. 241, p. 372–375, doi:10.1038/241372a0.
Thordarson, T., and Larsen, G., 2007, Volcanism in Iceland in historical time: Volcano types, eruption styles and eruptive history: Journal of Geodynamics, v. 43.
Thordarson, T., and Self, S., 2003, Atmospheric and environmental effects of the 1783–1784 Laki eruption: A review and reassessment: Journal of Geophysical Research: Atmospheres, v. 108, p. AAC 7-1, doi:10.1029/2001JD002042.
Thordarson, T., and Self, S., 1996, Sulfur, chlorine and fluorine degassing and atmospheric loading by the Roza eruption, Columbia River Basalt Group, Washington, USA: Journal of Volcanology and Geothermal Research, v. 74, p. 49–73, doi:10.1016/S0377-0273(96)00054-6.
Thordarson, T., and Self, S., 1998, The Roza Member, Columbia River Basalt Group: A gigantic pahoehoe lava flow field formed by endogenous processes? Journal of Geophysical Research: Solid Earth, v. 103, p. 27411–27445, doi:10.1029/98JB01355.
Thordarson, T., Self, S., Óskarsson, N., and Hulsebosch, T., 1996, Sulfur, chlorine, and fluorine degassing and atmospheric loading by the 1783–1784 AD Laki (Skaftár Fires) eruption in Iceland: Bulletin of Volcanology 1996 58:2, v. 58, p. 205–225, doi:10.1007/S004450050136.
Wan, Y., Zhang, Y., Williams, I., Liu, D., Dong, C., Fan, R., Shi, Y., and Ma, M., 2013, Extreme zircon O isotopic compositions from 3.8 to 2.5 Ga magmatic rocks from the Anshan area, North China Craton: Chemical Geology, v. 352, doi:10.1016/j.chemgeo.2013.06.009.
Wolf, R.A., Farley, K.A., and Silver, L.T., 1996, Helium diffusion and low-temperature thermochronometry of apatite: Geochimica et Cosmochimica Acta, v. 60, p. 4231–4240, doi:10.1016/S0016-7037(96)00192-5.
Wylie, J.J. et al., 1999, Flow localization in fissure eruptions: Bulletin of Volcanology, v. 60, p. 432–440.
Žák, J., Verner, K., Tomek, F., Holub, F. V, Johnson, K., and Schwartz, J.J., 2015, Simultaneous batholith emplacement, terrane/continent collision, and oroclinal bending in the Blue Mountains Province, North American Cordillera:, doi:10.1002/2015TC003859.
Zeitler, P., Ketcham, R., Reiners, P., Shuster, D., and Stockli, D., 2020, Little Devil's Postpile Data Compilation: Harvard Dataverse, doi:10.7910/DVN/TXJGNU.

Appendix A: Detailed Tables for Thermochronologic Analyses

Table A.1—Apatite He details for samples collected in this study

Grain ID	U ppm (Ca)	U SD ppm (Ca)	Th ppm (Ca)	Th SD ppm (Ca)	Sm ppm (Ca)	Sm SD ppm (Ca)	He pmol	He error pmol	He nmol/g (Ca)	Mass mg
21A358_KM21_20Jack_K1_Ap1	29.2	0.93	47	1.5	279	8.9	0.1146	0.000416	14.3	0.0080
21A359_KM21_20Jack_K1_Ap2	27.3	0.91	42	1.4	251	8.4	0.0705	0.000157	14.2	0.0050
21A360_KM21_20Jack_K1_Ap3	30	1.0	48	1.5	256	8.3	0.1050	0.000229	16.5	0.0064
21A361_KM21_20Jack_K1_Ap4	34	1.1	56	1.8	344	11.1	0.1023	0.000233	17.1	0.0060
21A345_KM21_20Max_K1_Ap1	45	2.7	60	3.5	235	13.9	0.0316	0.000115	4.5	6.99E-06
21A346_KM21_20Max_K1_Ap2	45	2.4	64	3.4	228	12.1	0.0215	0.000082	4.5	4.83E-06
21A347_KM21_20Max_K1_Ap3	64	2.1	72	2.3	229	7.5	0.0421	0.000153	6.1	6.88E-06
21A348_KM21_20Max_K1_Ap4	42	2.3	63	3.5	228	12.7	0.0200	0.000080	4.1	4.81E-06
21A349_KM21_20Max_K2_Ap1	50	2.9	65	3.8	223	13.2	0.0288	0.000114	4.8	5.95E-06
21A350_KM21_20Max_K2_Ap2	57	3.7	64	4.1	212	13.7	0.0407	0.000158	5.4	7.55E-06
21A351_KM21_20Max_K2_Ap3	44	2.5	58	3.3	198	11.4	0.0419	0.000152	4.3	9.65E-06
21A352_KM21_20Max_K2_Ap4	56	2.1	68	2.6	292	11.5	0.0955	0.000339	5.6	1.71E-05
21A353_KM21_20Max_K3_Ap1	46	1.6	62	2.1	236	8.0	0.2776	0.001011	25.2	1.10E-05
21A354_KM21_20Max_K3_Ap2	45	2.1	62	2.9	207	9.9	0.1696	0.000608	24.8	6.84E-06
21A355_KM21_20Max_K3_Ap3	65	2.3	79	2.8	269	9.6	0.3787	0.001309	32.6	1.16E-05
21A356_KM21_20Max_K3_Ap4	41	2.8	58	3.9	226	15.2	0.2553	0.000890	22.8	1.12E-05
21B329_20JACKE_K1ap_1	29.2	0.71	41	1.0	246	6.2	0.0086	0.000036	2.6	6.473E-08
21B331_20JACKE_K1ap_3	26.9	0.66	39	1.0	234	5.9	0.0099	0.000039	2.5	7.853E-08
21B332_20JACKE_K1ap_4	31.8	0.80	41	1.0	269	6.9	0.0155	0.000053	6.5	4.902E-08
21B333_20JACKE_K2ap_1	26.8	0.7	38	1.0	297	8.0	0.0020	0.000012	2.1	2.067E-08
21B334_20JACKE_K2ap_2	26.5	0.7	32.5	0.82	238	6.1	0.0050	0.000015	2.4	4.273E-08
21B335_20JACKE_K2ap_3	30.1	0.7	39	1.0	249	6.3	0.0025	0.000011	2.4	2.030E-08
21B336_20JACKE_K2ap_4	31.8	0.83	41	1.1	239	6.4	0.0008	0.000008	2.1	8.407E-09
21B337_20JACKE_K3ap_1	31.4	0.79	47	1.2	268	6.9	0.0068	0.000021	2.7	5.209E-08
21B338_20JACKE_K3ap_2	39	1.0	41	1.0	244	6.1	0.0041	0.000018	2.8	2.906E-08
21B339_20JACKE_K3ap_3	28.5	0.76	39	1.0	264	7.2	0.0058	0.000021	2.5	5.218E-08
21B340_20JACKE_K3ap_4	31.1	0.80	40	1.0	174	4.6	0.0022	0.000009	2.2	2.057E-08
21B383_20JACKE_K4_Ap1_Re-run	19.2	0.40	32.9	0.68	181	3.9	0.0105	0.000062	2.1	4.99E-06
21B384_20JACKE_K4_Ap2	34.1	0.71	33.0	0.69	178	3.8	0.0238	0.000062	5.6	4.25E-06
21B385_20JACKE_K4_Ap3	19.9	0.84	32	1.3	237	10.0	0.0155	0.000058	2.9	5.26E-06
21B386_20JACKE_K4_Ap4	37.2	0.81	50	1.1	329	7.4	0.0162	0.000065	3.5	4.57E-06
21B387_20JACKE_K5_Ap1	28	1.1	36	1.4	220	8.5	0.0726	0.000223	12.6	5.75E-06
21B388_20JACKE_K5_Ap2	29	1.3	36	1.7	238	10.9	0.0203	0.000090	11.8	1.72E-06
21B389_20JACKE_K5_Ap3	31.7	0.66	41.0	0.86	208	4.5	0.0366	0.000142	13.3	2.74E-06
21B390_20JACKE_K5_Ap4	29.4	0.66	40.0	0.90	219	5.1	0.0289	0.000069	12.6	2.29E-06

Table A.1—Apatite He details for samples collected in this study (continued)

Grain ID	FT 238U[1]	FT 235U[1]	FT 232Th[1]	FT 147Sm[1]	Radius µm	Shape[2]	Roundness[3]	length µm	width µm	Uncorr. Age Ma	Corr. Age Ma	Error Ma	eU w/ Sm ppm
21A358_KM21_20Jack_K1_Ap1	0.82	0.79	0.79	0.94	80	1	2	259	128	65.2	80.4	0.92	41
21A359_KM21_20Jack_K1_Ap2	0.79	0.76	0.76	0.93	68	1	2	227	110	69.4	89.1	1.0	38
21A360_KM21_20Jack_K1_Ap3	0.80	0.77	0.77	0.93	71	1	2	242	126	73	93	1.1	42
21A361_KM21_20Jack_K1_Ap4	0.80	0.77	0.77	0.94	74	1	2	222	115	65.6	82.4	0.91	49
21A345_KM21_20Max_K1_Ap1	0.79	0.76	0.76	0.93	70	1	2	220	116	14.2	18.1	0.24	60
21A346_KM21_20Max_K1_Ap2	0.76	0.73	0.73	0.92	61	1	2	204	127	13.6	18.1	0.21	61
21A347_KM21_20Max_K1_Ap3	0.80	0.77	0.77	0.93	71	1	2	266	130	13.9	17.6	0.21	82
21A348_KM21_20Max_K1_Ap4	0.77	0.74	0.74	0.93	63	1	2	210	184	13.5	17.6	0.20	58
21A349_KM21_20Max_K2_Ap1	0.78	0.75	0.75	0.93	65	1	2	247	157	13.7	17.8	0.21	66
21A350_KM21_20Max_K2_Ap2	0.79	0.76	0.76	0.93	68	1	1	258	127	13.8	17.6	0.24	73
21A351_KM21_20Max_K2_Ap3	0.80	0.78	0.78	0.94	74	1	2	289	156	13.8	17.4	0.21	59
21A352_KM21_20Max_K2_Ap4	0.86	0.84	0.84	0.95	103	1	2	373	162	14.4	16.9	0.20	73
21A353_KM21_20Max_K3_Ap1	0.82	0.80	0.80	0.94	82	1	1	280	146	76	93	1.1	62
21A354_KM21_20Max_K3_Ap2	0.80	0.77	0.77	0.93	71	1	2	261	123	76	97	1.1	60
21A355_KM21_20Max_K3_Ap3	0.83	0.81	0.81	0.95	87	1	2	313	129	72	87	1.0	85
21A356_KM21_20Max_K3_Ap4	0.86	0.84	0.84	0.95	105	2	2	268	138	76	89	1.0	56
21B329_20JACKE_K1ap_1	0.75	0.72	0.72	0.92	57	1	1	200	109	12.3	16.6	0.2	40
21B331_20JACKE_K1ap_3	0.75	0.72	0.72	0.92	59	1	1	203	112	12.9	17.3	0.2	37
21B332_20JACKE_K1ap_4	0.72	0.69	0.69	0.91	51	1	1	172	99	28.9	40.4	0.5	43
21B333_20JACKE_K2ap_1	0.63	0.58	0.58	0.88	37	1	1	139	70	10.9	17.6	0.22	37
21B334_20JACKE_K2ap_2	0.70	0.66	0.66	0.90	48	1	1	162	91	12.9	18.6	0.21	35
21B335_20JACKE_K2ap_3	0.65	0.60	0.60	0.88	39	1	2	128	72	11.4	17.8	0.22	40
21B336_20JACKE_K2ap_4	0.58	0.52	0.52	0.86	32	1	1	113	61	9.5	16.7	0.25	43
21B337_20JACKE_K3ap_1	0.71	0.67	0.67	0.91	49	1	1	212	89	11.7	16.6	0.19	44
21B338_20JACKE_K3ap_2	0.66	0.62	0.62	0.89	41	1	2	171	73	10.6	16.2	0.20	50
21B339_20JACKE_K3ap_3	0.73	0.69	0.69	0.91	53	1	1	167	103	12.1	16.8	0.19	39
21B340_20JACKE_K3ap_4	0.64	0.59	0.59	0.88	38	1	2	130	69	10.2	16.3	0.20	41
21B383_20JACKE_K4_Ap1_Re-run	0.77	0.74	0.74	0.93	63	1	2	206	115	14.4	18.8	0.23	28
21B384_20JACKE_K4_Ap2	0.74	0.71	0.71	0.92	56	1	2	195	100	24.7	33.5	0.40	43
21B385_20JACKE_K4_Ap3	0.77	0.73	0.73	0.93	62	1	2	218	110	19.7	26.0	0.29	28
21B386_20JACKE_K4_Ap4	0.74	0.70	0.70	0.92	54	1	2	246	94	13.3	18.2	0.21	50
21B387_20JACKE_K5_Ap1	0.77	0.74	0.74	0.93	63	1	2	207	115	63.5	83.1	0.95	37
21B388_20JACKE_K5_Ap2	0.68	0.64	0.64	0.90	44	1	2	141	81	58	86	1.1	38
21B389_20JACKE_K5_Ap3	0.71	0.67	0.67	0.91	49	1	2	184	87	59.1	84.1	0.99	42
21B390_20JACKE_K5_Ap4	0.70	0.66	0.66	0.90	46	1	2	170	83	60	87	1.0	40

1 alpha-ejection correction (Farley et al., 1996)

2 grain shape nn—whole grain, np—one termination, pp—no terminations

3 roundness: 1— euhedral; 2— somewhat rounded; 3— very rounded

Table A.2—Zircon He details for samples collected during this study

Grain ID	U	U SD	Th	Th SD	He	He error	He	Mass	FT 238U[1]	FT 235U[1]
	ppm (Zr)	ppm (Zr)	ppm (Zr)	ppm (Zr)	pmol	pmol	nmol/g (Zr)	g		
21A478_KM21_20Jack_K1_Zr1	155	3.6	57	1.4	1.086	0.00186	70	1.55E-05	0.849	0.827
21A479_KM21_20Jack_K1_Zr2	276	5.8	83	1.8	2.482	0.00467	109	2.28E-05	0.866	0.845
21A480_KM21_20Jack_K1_Zr3	202	4.3	88	1.9	2.709	0.00234	110	2.45E-05	0.867	0.846
21A481_KM21_20Jack_K1_Zr4	217	5.3	96	2.4	1.726	0.00150	109	1.58E-05	0.830	0.804
21A672_KM21_20Max_K1_Zr6	106	2.4	47	1.1	0.094	0.00073	9	1.01E-05	0.826	0.800
21A467_KM21_20Max_K1_Zr2	110	2.4	52	1.1	0.083	0.00063	9	9.70E-06	0.816	0.789
21A468_KM21_20Max_K1_Zr3	158	3.5	63	1.4	0.182	0.00026	12	1.58E-05	0.858	0.836
21A469_KM21_20Max_K1_Zr4	123	2.6	50	1.1	0.168	0.00020	9	1.84E-05	0.853	0.830
21A470_KM21_20Max_K2_Zr1	131	2.9	58	1.3	0.710	0.00076	60	1.18E-05	0.822	0.795
21A471_KM21_20Max_K2_Zr2	149	3.1	64	1.4	0.706	0.00078	71	9.98E-06	0.842	0.819
21A472_KM21_20Max_K2_Zr3	140	3.0	53	1.2	1.261	0.00110	72	1.76E-05	0.845	0.822
21A473_KM21_20Max_K2_Zr4	199	4.4	71	1.6	1.129	0.00096	100	1.13E-05	0.840	0.816
21A474_KM21_20Max_K3_Zr1	295	6.5	112	2.5	0.812	0.00385	132	6.13E-06	0.790	0.760
21A475_KM21_20Max_K3_Zr2	189	4.3	67	1.6	1.600	0.00758	97	1.65E-05	0.841	0.817
21A476_KM21_20Max_K3_Zr3	118	2.7	53	1.2	1.335	0.00633	68	1.96E-05	0.860	0.839
21A477_KM21_20Max_K3_Zr4	107	2.7	44	1.1	1.805	0.00308	60	3.01E-05	0.881	0.863
21A800_20JACKE_K1_1	161	3.4	56	1.2	0.487	0.00423	72	6.73E-06	0.813	0.785
21A801_20JACKE_K1_2	151	3.2	60	1.3	0.270	0.00235	58	4.68E-06	0.784	0.752
21A802_20JACKE_K1_3	163	3.4	61	1.3	0.257	0.00223	61	4.24E-06	0.772	0.739
21A803_20JACKE_K1_4	154	3.2	61	1.3	0.239	0.00146	64	3.74E-06	0.768	0.735
21B419_20JACKE_K1_Zr5	213	32.1	81	12.1	0.448	0.00197	89	5.01E-06	0.758	0.723
21B420_20JACKE_K1_Zr6	146	22.0	48	7.2	0.295	0.00141	58	5.08E-06	0.766	0.732
21B421_20JACKE_K1_Zr7	119	17.9	52	7.8	0.253	0.00146	49	5.12E-06	0.759	0.724
21B422_20JACKE_K1_Zr8	134	20.1	47	7.1	0.324	0.00075	62	5.25E-06	0.769	0.735
21A804_20JACKE_K2_1	110	2.3	45	1.0	0.086	0.00053	14	6.26E-06	0.800	0.770
21A805_20JACKE_K2_2	196	4.4	79	1.8	0.242	0.00147	30	7.94E-06	0.822	0.795
21A806_20JACKE_K2_3	167	3.8	55	1.3	0.127	0.00040	13	9.56E-06	0.840	0.816
21A807_20JACKE_K2_4	136	2.9	54	1.1	0.083	0.00027	15	5.43E-06	0.809	0.781
21B423_20JACKE_K2_Zr5	110	16.5	68	10.3	0.017	0.00009	9	1.89E-06	0.680	0.636
21B424_20JACKE_K2_Zr6	438	66.0	269	40.6	0.321	0.00152	59	5.45E-06	0.778	0.746
21B425_20JACKE_K2_Zr7	105	15.8	49	7.4	0.065	0.00026	12	5.65E-06	0.764	0.729
21B426_20JACKE_K2_Zr8	203	30.5	89	13.4	0.068	0.00028	16	4.10E-06	0.740	0.703
21A808_20JACKE_K3_1	207	4.4	60	1.3	0.401	0.00126	80	5.00E-06	0.792	0.762
21A809_20JACKE_K3_2	126	2.6	48	1.0	0.275	0.00087	56	4.93E-06	0.781	0.750
21A810_20JACKE_K3_3	119	2.5	52	1.1	0.211	0.00075	50	4.19E-06	0.746	0.709
21A811_20JACKE_K3_4	478	10.0	133	2.8	1.347	0.00234	178	7.58E-06	0.793	0.763
21A812_20JACKE_K4_1	352	7.7	117	2.5	0.443	0.00077	152	2.92E-06	0.759	0.724
21A813_20JACKE_K4_2	215	4.6	80	1.7	0.183	0.00043	92	2.00E-06	0.713	0.673
21A814_20JACKE_K4_3	281	5.9	133	2.8	0.590	0.00104	147	4.02E-06	0.761	0.727
21A815_20JACKE_K4_4	204	4.3	92	2.0	0.442	0.00107	104	4.27E-06	0.745	0.708
21A816_20JACKE_K5_1	365	7.7	85	1.8	1.406	0.00173	149	9.41E-06	0.821	0.795
21A817_20JACKE_K5_2	174	3.7	62	1.3	0.709	0.00088	101	7.02E-06	0.796	0.766
21A818_20JACKE_K5_3	193	4.7	47	1.1	0.815	0.00102	86	9.52E-06	0.815	0.788
21A819_20JACKE_K5_4	103	2.4	41	1.0	0.248	0.00032	50	4.94E-06	0.770	0.737

1 alpha-ejection correction (Farley, 2001)

2 grain shape: 1—whole grain, 1.5—one termination, 2—no terminations

3 abrasion index: 1— pointed tips; 2— one tip abraded; 3— both tips mildly abraded; 4— both tips heavily blunted; 5— no visible tips (completely rounded)

Table A.2—Zircon He details for samples collected during this study (continued)

Grain ID	FT 232Th[1]	FT 147Sm[1]	Radius	Shape[2]	Abrasion Index[3]	average length	average width	Uncorr. Age	Corr. Age	Error	eU (Zr)
			μm			μm	μm	Ma	Ma	Ma	ppm
21A478_KM21_20Jack_K1_Zr1	0.827	0.953	82	1	1	334	132	77	90	1.2	168
21A479_KM21_20Jack_K1_Zr2	0.845	0.958	93	1	1	346	161	68	78	1.0	296
21A480_KM21_20Jack_K1_Zr3	0.846	0.958	93	1	1	402	146	91	106	1.3	222
21A481_KM21_20Jack_K1_Zr4	0.804	0.947	72	1	1	405	109	84	101	1.3	239
21A672_KM21_20Max_K1_Zr6	0.800	0.946	71	1	1	275	115	14.8	18.0	0.27	117
21A467_KM21_20Max_K1_Zr2	0.789	0.942	67	1	1	326	101	13.0	16.0	0.24	122
21A468_KM21_20Max_K1_Zr3	0.836	0.956	87	1	1	471	135	12.3	14.4	0.19	173
21A469_KM21_20Max_K1_Zr4	0.830	0.954	84	1	1	331	135	12.5	14.7	0.19	135
21A470_KM21_20Max_K2_Zr1	0.795	0.944	69	1	1	329	107	76	93	1.2	145
21A471_KM21_20Max_K2_Zr2	0.819	0.951	78	1	1	283	129	79	94	1.2	164
21A472_KM21_20Max_K2_Zr3	0.822	0.952	80	1	2	336	127	87	103	1.3	152
21A473_KM21_20Max_K2_Zr4	0.816	0.950	77	1	2	307	123	86	102	1.3	215
21A474_KM21_20Max_K3_Zr1	0.760	0.934	58	1	2	307	89	76	97	1.3	321
21A475_KM21_20Max_K3_Zr2	0.817	0.950	77	1	1	371	119	87	104	1.4	205
21A476_KM21_20Max_K3_Zr3	0.839	0.956	89	1	1	344	142	96	112	1.5	130
21A477_KM21_20Max_K3_Zr4	0.863	0.963	105	1	1	362	175	94	107	1.4	117
21A800_20JACKE_K1_1	0.785	0.941	65	1	1	232	108	76	94	1.5	174
21A801_20JACKE_K1_2	0.752	0.932	56	1	1	204	93	65	83	1.3	165
21A802_20JACKE_K1_3	0.739	0.928	53	1	1	206	86	63	82	1.3	177
21A803_20JACKE_K1_4	0.735	0.927	52	1	1	213	83	70	92	1.3	168
21B419_20JACKE_K1_Zr5	0.723	0.923	50	1	2	281	76	71	94	1.3	232
21B420_20JACKE_K1_Zr6	0.732	0.926	52	1	2	221	82	68	89	1.2	157
21B421_20JACKE_K1_Zr7	0.724	0.923	50	1	2	250	77	69	92	1.3	131
21B422_20JACKE_K1_Zr8	0.735	0.927	52	1	2	240	82	78	102	1.3	145
21A804_20JACKE_K2_1	0.770	0.937	61	1	1	261	95	21.1	26.5	0.37	121
21A805_20JACKE_K2_2	0.795	0.944	69	1	1	224	117	26.3	32.1	0.46	214
21A806_20JACKE_K2_3	0.816	0.950	77	1	1	242	133	13.7	16.3	0.22	180
21A807_20JACKE_K2_4	0.781	0.940	64	1	1	204	110	19.1	23.7	0.32	149
21B423_20JACKE_K2_Zr5	0.636	0.897	37	1	1	150	60	13.5	20.0	0.27	126
21B424_20JACKE_K2_Zr6	0.746	0.930	55	1	2	199	91	21.8	28.1	0.37	502
21B425_20JACKE_K2_Zr7	0.729	0.925	51	1	2	263	78	18.3	24.1	0.32	117
21B426_20JACKE_K2_Zr8	0.703	0.917	46	1	1	247	69	13.6	18.5	0.2	224
21A808_20JACKE_K3_1	0.762	0.934	59	1	1	211	99	67	85	1.1	221
21A809_20JACKE_K3_2	0.750	0.931	56	1	1	238	88	75	96	1.3	137
21A810_20JACKE_K3_3	0.709	0.919	47	1	1	279	72	71	95	1.3	131
21A811_20JACKE_K3_4	0.763	0.935	59	1	2	303	89	64	82	1.1	509
21A812_20JACKE_K4_1	0.724	0.923	50	1	1	182	82	74	97	1.3	380
21A813_20JACKE_K4_2	0.673	0.908	41	1	1	134	72	72	102	1.4	234
21A814_20JACKE_K4_3	0.727	0.924	51	1	1	248	78	87	114	1.5	312
21A815_20JACKE_K4_4	0.708	0.919	47	1	1	279	70	84	114	1.5	226
21A816_20JACKE_K5_1	0.795	0.944	69	1	2	208	121	72	87	1.2	385
21A817_20JACKE_K5_2	0.766	0.935	60	1	1	253	95	99	124	1.6	188
21A818_20JACKE_K5_3	0.788	0.942	66	1	1	289	107	77	95	1.3	204
21A819_20JACKE_K5_4	0.737	0.927	53	1	1	276	81	82	107	1.5	113

1 alpha-ejection correction (Farley, 2001)

2 grain shape: 1—whole grain, 1.5—one termination, 2—no terminations

3 abrasion index: 1— pointed tips; 2— one tip abraded; 3— both tips mildly abraded; 4— both tips heavily blunted; 5— no visible tips (completely rounded)

Table A.3— Apatite fission track details for Jackson A dike segment

	2E1	2E2	2E3	2E4	2E5	2E6	2E7	2E8	2E9	20JACK-K1
Pooled age (Ma)	15	16	15	15	15	16	15	58	95	100
95%-CI (Ma)	1.6	1.8	1.6	1.5	1.4	1.5	1.1	3.4	4.8	5.0
95%+CI (Ma)	1.7	2.0	1.8	1.7	1.5	1.7	1.2	3.6	5.1	5.2
wmean pz:sz Uca	0.5362	0.5273	0.5189	0.5111	0.5057	0.5469	0.5382	0.5312	0.5218	0.5133
wmean pz:unk Ca	1.0181	1.0182	1.0181	1.0181	1.0181	1.0181	1.0181	1.0181	1.0181	1.0181
relerr pz:sz	0.0143	0.0143	0.0143	0.0143	0.0143	0.0135	0.0135	0.0135	0.0135	0.0135
relerr analyst	0	0	0	0	0	0	0	0	0	0
relerr deficit	0	0	0	0	0	0	0	0.085	0.057	0.027
relerr Ca apfu	0	0	0	0	0	0	0	0	0	0
Primary Zeta	8.2727	8.2727	8.2727	8.2727	8.2727	8.2727	8.2727	8.2727	8.2727	8.2727
1s (+/-)	0.1407	0.1407	0.1407	0.1407	0.1407	0.1407	0.1407	0.1407	0.1407	0.1407
Number of Spots	40	40	40	40	40	40	40	35	40	40
Number of Tracks	526	344	372	465	527	436	934	1607	2592	2742
Rho	0.000295	0.000182	0.000199	0.000254	0.000285	0.000231	0.000499	0.000227	0.000225	0.000226
1s (+/-)	0.00000877	0.000004	0.00000241	0.00000488	0.00000178	0.000000799	0.00000349	0.000000927	0.000000862	0.000000781
Sample	2E1	2E2	2E3	2E4	2E5	2E6	2E7	2E8	2E9	20JACK-K1
Cation Isotope	43Ca	43Ca	43Ca	43Ca	43Ca	43Ca	43Ca	43Ca	43Ca	43Ca
chi-squared	23.3133	9.1039	21.6502	28.1928	46.328	18.9551	42.5136	65.2737	67.8873	57.1016
Q(chi-squared)	0.978	1	0.9889	0.9001	0.1956	0.9972	0.3222	0.001	0.0028	0.0307
Mean Dpar (µm)	2.01	2.11	2.09	2.06	2.08	2.27	2.18	2.11	2.08	2.17
Mean Dper (µm)	0.4	0.46	0.42	0.45	0.45	0.5	0.49	0.46	0.46	0.49
Mean [U] (ppm)	38.3	35.61	28.98	37.87	49.94	28.09	62.83	37.33	29.47	25.42
Mean [Th] (ppm)	86.51	62.1	66.13	91.88	117.06	103.19	136.65	99.89	93.78	96.17
Mean [Sm] (ppm)	224.37	169.46	170.61	200.69	235.2	180.99	235.52	243.76	224.64	225.1
Sample	2E1	2E2	2E3	2E4	2E5	2E6	2E7	2E8	2E9	20JACK-K1
Mean track length (µm)	14.3	14.6	14.7	14.2	14.4	14.6	14.5	11.7	12.6	13.5
Std. error (µm)	0.09	0.09	0.1	0.12	0.1	0.1	0.1	0.23	0.13	0.12
Std. dev (µm)	1.1	1.1	1.2	1.3	1.1	1.2	1.2	2.6	1.6	1.5
Skewness	-0.3638	-0.1419	-0.5112	-1.1547	-0.5587	-1.5765	-0.7064	0.1321	0.3385	-0.3682
Kurtosis	0.096	-0.1235	1.025	2.1084	1.8177	9.425	1.6075	-1.1597	-0.0877	-0.024
Number tracks	143	143	135	125	130	130	135	126	151	150
Mean Dpar (µm)	2.04	2.07	2.19	2.18	2.18	2.24	2.35	2.17	2.16	2.16
Mean Dper (µm)	0.38	0.38	0.47	0.51	0.48	0.49	0.49	0.5	0.44	0.42
Analyst Initials	pos	pos	pos	pos	pos	pos	pos	pos	pos	pos

Table A.4— Zircon fission track details for Jackson A dike segment

	2E1	2E2	2E3	2E4	2E5	2E6
Pooled age (Ma)	16	47	63	77	105	121
95%-CI (Ma)	1.9	5.0	6.8	8.6	11.2	12.7
95%+CI (Ma)	2.2	5.6	7.6	9.7	12.5	14.1
wmean pz:sz UCa	0.0052	0.0052	0.0051	0.005	0.0049	0.0048
wmean pz:unk Ca	1	1	1	1	1	1
relerr pz:sz	0.1417	0.1417	0.1417	0.1417	0.1417	0.1417
relerr analyst	0.175	0.175	0.175	0.175	0.175	0.175
relerr deficit	0	0	0	0	0	0
relerr Ca apfu	0	0	0	0	0	0
Primary Zeta	0.0401	0.0401	0.0401	0.0401	0.0401	0.0401
1s (+/-)	0.0005	0.0005	0.0005	0.0005	0.0005	0.0005
Number of Spots	20	20	20	20	20	20
Number of Tracks	1545	3098	3406	3435	3247	3360
Rho	0.00000394	0.00000265	0.00000217	0.00000179	0.00000122	0.0000011
1s (+/-)	0.000000227	0.000000139	0.000000116	9.99E-08	6.37E-08	5.66E-08
Cation Isotope	28Si	28Si	28Si	28Si	28Si	28Si
chi-squared	8.652	20.6176	17.8378	13.0792	4.0472	3.8956
Q(chi-squared)	0.9788	0.3583	0.5333	0.8345	0.9999	0.9999
Analyst Initials	pos	pos	pos	pos	pos	pos

Table A.5—Biotite $^{40}Ar/^{39}Ar$ single step fusion data for Maxwell A and Jackson A dike segments

Identifier	Sample	sample material	distance from dike *(m)*	N	Power *W*	Age *(Ma)*	±1σ *(Ma)*	K/Ca	±1σ	%40Ar *(%)*	40Ar*/39ArK
100741	2E1	0.4A	2	1	12	-16	13.6	2.4	0.33	-6.97	-2.44
				01A	15	0.0	0.0	-0.2	0.53	-38.57	-827.31
				2	12	14.2	2.0	19	4.4	5.53	2.15
				3	12	125.1	0.87	153	146.7	92.57	19.61
100743	2E2	0.4A	5	1	12	123.6	1.2	88	29.9	52.99	19.37
				2	12	94	185.1	0.5	0.28	17.91	14.59
				3	12	124.1	0.61	99	35.3	68.74	19.44
100745	2E3	light fraction	11	1	12	115	1.8	10.4	0.62	37.27	17.95
				2	12	126.4	0.54	-346	1594.0	90.21	19.81
				3	12	127.8	0.20	33	4.2	96.25	20.04
100744	2E3	0.4A	11	1	12	128	3.9	2.7	0.09	54.60	20.15
				2	12	125.6	0.67	494	1256.3	93.58	19.69
				3	12	126	1.0	158	174.2	91.84	19.73
100746	2E4	0.4A	20.5	1	12	125	1.0	42	5.8	76.41	19.54
				2	12	125.6	0.87	18	1.1	88.54	19.69
				3	12	124.8	0.61	13.4	0.58	93.00	19.55
100747	2E5	0.4A	30	1	12	124	1.6	22	2.6	58.60	19.35
				2	12	115.7	0.54	18.2	0.82	86.00	18.08
				3	12	105	6.8	16	3.5	5.67	16.37
100748	2E6	0.4A	40	1	12	125	2.0	26	4.4	75.14	19.51
				2	12	114	2.6	6.4	0.53	76.65	17.88
				3	12	126	1.6	23	3.6	85.52	19.71

Table A.5—Biotite $^{40}Ar/^{39}Ar$ single step fusion data for Maxwell A and Jackson A dike segments (continued).

Identifier	Sample	sample material	distance from dike *(m)*	N	Power *W*	Age *(Ma)*	±1σ *(Ma)*	K/Ca	±1σ	%40Ar *(%)*	40Ar*/39ArK
				1	12	123	2.3	57	21.1	41.05	19.32
100749	2E7	0.4A	53.5	2	12	124	11.9	24	11.4	3.76	19.46
				3	12	119	3.0	129	239.2	64.35	18.56
				1	12	125.6	0.75	44	6.1	92.77	19.69
100750	2E8	0.4A	72.5	2	12	128	1.4	17	2.1	84.84	20.12
				3	12	127	2.0	150	223.5	87.43	19.96
				1	12	121	4.0	69	83.9	78.35	18.96
100751	2E9	0.4A	100	2	12	127	3.9	51	59.0	87.17	19.95
				3	12	122	6.6	-9	2.8	35.14	19.11
				1	12	126	1.2	21	2.8	76.77	19.74
100752	20JACK-K1	coarse fraction	215	2	12	125.7	0.40	293	180.9	76.32	19.70
				3	12	126.4	0.35	61	6.1	80.67	19.82
				1	12	133.3	0.69	11.0	0.33	59.03	20.93
100753	20JACK-K1	0.5A	215	2	12	123	2.0	15	2.0	26.96	19.26
				3	12	126.0	0.22	15.0	0.30	83.05	19.75
				1	12	126	1.2	52	13.1	86.83	19.70
100754	20JACK-K1	light fraction	215	2	12	125.8	0.38	39	3.1	96.01	19.72
				3	12	125.6	0.72	26	3.4	83.69	19.68

Table A.5—Biotite $^{40}Ar/^{39}Ar$ single step fusion data for Maxwell A and Jackson A dike segments (continued).

Identifier	Sample	sample material	distance from dike *(m)*	N	Power *W*	Age *(Ma)*	±1σ *(Ma)*	K/Ca	±1σ	%40Ar *(%)*	40Ar*/39ArK
				1	12	53	1.5	51	14.2	18.49	8.17
100755	20MAX-K1	light fraction	3.1	2	12	72.0	0.71	29	2.8	35.26	11.12
				3	12	86.3	0.54	126	55.5	82.50	13.37
				1	12	126	1.0	28	2.6	42.24	19.70
100757	20MAX-K3A	light fraction	15	2	12	129.9	0.46	3.9	0.04	64.99	20.39
				3	12	130.6	0.62	49	10.6	86.07	20.49
				1	12	133.9	0.72	30	3.1	79.70	21.03
100758	20MAX-K3B	light fraction	22.5	2	12	130.1	0.24	34	1.8	85.61	20.42
				3	12	135.7	0.76	28	4.2	74.92	21.32

Table A.6—Biotite $^{40}Ar/^{39}Ar$ step heating data for Maxwell A and Jackson A dike segments.

Sample	Identifier	Material	N	$\%^{39}Ar$	MSWD	K/Ca	±1σ	Age (Ma)	±1σ	$(^{40}Ar/^{36}Ar)_i$	±1σ
20MAX-K3	100758-04	lights	7/8	93.7	14.30	-0.434	0.301	132.5	0.62	268	6.0
20MAX-K3	100758-05	lights	3/8	95.2	2.90	2.456	1.699	130.4	0.70	284	8.2
20MAX-K3	100758-06	lights	7/8	88.8	22.54	-0.046	0.065	136.8	0.63	231	4.7
20MAX-K3	100758-07	lights	7/8	87.9	112.20	0.056	0.059	138.8	0.38	118	4.3
20MAX-K3	100758-08	lights	4/8	97.0	4.12	-0.024	0.106	126.7	0.34	293	17.4
20MAX-K3	100758-09	lights	4/8	87.5	6.54	-0.013	0.173	132.0	0.88	240	16.5
20MAX-K3	100758-10	lights	6/8	86.5	37.63	-0.056	0.021	135.8	0.46	263	2.8
20MAX-K3	100758-11	lights	4/8	93.6	40.11	-0.344	0.350	131.1	0.71	230	4.9
20MAX-K3	100758-12	lights	0/8	0.0	81.46	-0.165	0.199	0	0	209	3.0
20MAX-K3	100758-13	lights	4/8	91.7	11.70	-1.287	1.156	129.4	0.45	153	12.8
20MAX-K1	100755-04	lights	0/8	0.0	5.78	-0.074	0.077	0	0	710	164.7
20MAX-K1	100755-05	lights	4/8	68.9	23.40	0.164	0.067	71	4.4	-831	242.4
20MAX-K1	100755-06	lights	5/8	72.3	4.52	0.154	0.148	87	1.2	796	319.9
20MAX-K1	100755-07	lights	8/8	100.0	0.24	0.001	0.075	98	2.53	257	35.2
20MAX-K1	100755-08	lights	8/8	100.0	0.97	0.007	0.014	82	1.2	430	82.7
20MAX-K1	100755-09	lights	0/8	0.0	2.08	-0.007	0.011	0	0	4360	22037.3
20MAX-K1	100755-10	lights	8/8	100.0	0.51	0.041	0.029	87	1.8	316	13.8
20MAX-K1	100755-11	lights	8/8	100.0	0.25	0.020	0.023	62	4.3	298	6.3
20MAX-K1	100755-12	lights	5/8	60.5	12.17	0.026	0.026	78	1.0	306	9.2
20MAX-K1	100755-13	lights	0/8	0.0	4.39	-0.085	0.027	0	0	311	12.0
20MAX-K1	100755-14	lights	6/8	75.8	3.07	0.151	0.098	74	2.0	317	22.8
20MAX-K1	100755-15	lights	6/8	63.4	5.85	-0.002	0.028	55	1.6	230	16.2
20MAX-K1	100755-16	lights	8/8	100.0	0.83	-0.024	0.036	64.7	0.98	296	7.0
20MAX-K1	100755-17	lights	6/8	82.8	1.18	0.162	0.123	79	2.0	282	19.6
20MAX-K1	100755-18	lights	8/8	100.0	1.30	1.538	1.054	79	1.8	278	18.6
20MAX-K1	100755-19	lights	5/8	69.3	7.93	0.044	0.059	95.0	0.94	1584	1456.6
20MAX-K1	100755-20	lights	4/8	90.0	2.20	-0.217	0.142	77	1.5	329	27.5
20MAX-K1	100755-21	lights	8/8	100.0	1.13	0.014	0.038	85.7	0.74	341	78.2
20MAX-K1	100755-22	lights	3/8	75.6	16.39	0.026	0.043	64.2	0.95	667	128.9

Table A.6—Biotite $^{40}Ar/^{39}Ar$ step heating data for Maxwell A and Jackson A dike segments (continued).

Sample	Identifier	Material	N	$\%^{39}Ar$	MSWD	K/Ca	±1σ	Age (Ma)	±1σ	$(^{40}Ar/^{36}Ar)_I$	±1σ
2E5	100747-04	0.4A	8/8	100.0	2.63	0.642	0.130	125.3	0.38	1114	913.3
2E5	100747-05	0.4A	8/8	100.0	1.34	-0.203	0.284	125.2	0.33	376	76.1
2E5	100747-06	0.4A	0/8	0.0	5.79	0.033	0.025	0	0	303	7.3
2E5	100747-07	0.4A	6/8	60.6	2.61	0.012	0.011	124.5	1.5	284	10.1
2E5	100747-08	0.4A	4/8	94.5	3.33	0.141	0.056	126.4	0.51	266	21.0
2E5	100747-09	0.4A	0/8	0.0	11.99	0.308	0.238	0	0	300	2.2
2E5	100747-10	0.4A	0/8	0.0	9.64	0.005	0.431	0	0	2452	6341.6
2E5	100747-11	0.4A	0/8	0.0	20.31	0.401	0.359	0	0	300	2.3
2E5	100747-12	0.4A	0/8	0.0	2.37	0.251	0.403	0	0	235	47.9
2E5	100747-13	0.4A	8/8	100.0	1.19	0.063	0.165	127	1.5	406	98.5
2E1	100741-04	0.4A	6/6	100.0	0.06	0.032	0.062	33	1.3	296	32.5
2E1	100741-05	0.4A	6/6	100.0	1.00	-0.421	2.309	40	3.4	313	26.2
2E1	100741-06	0.4A	0/6	0.0	12.39	-0.047	0.088	0	0	1244	630.8
2E1	100741-07	0.4A	3/6	57.1	3.96	0.877	0.614	37	1.6	287	20.6
2E1	100741-08	0.4A	3/6	67.6	41.67	0.030	0.519	50	1.1	424	31.3
2E1	100741-09	0.4A	6/6	100.0	0.48	-0.020	0.095	27	1.9	313	15.4
2E1	100741-10	0.4A	0/6	0.0	40.75	0.031	0.099	0	0	-1629	1390.3
2E1	100741-11	0.4A	0/6	0.0	30.82	0.099	0.170	0	0	766	115.9
2E1	100741-13	0.4A	8/8	100.0	0.64	0.079	0.080	36	4.6	302	6.4
2E1	100741-14	0.4A	8/8	100.0	0.43	0.003	0.045	37	3.9	-1770	5834.6
2E1	100741-15	0.4A	8/9	65.4	6.62	-0.045	0.099	35	2.8	478	69.8
2E1	100741-16	0.4A	8/8	100.0	2.41	4.274	0.829	29	1.1	297	4.7
2E1	100741-17	0.4A	0/8	0.0	16.29	-0.101	0.122	0	0	291	21.6
2E1	100741-18	0.4A	0/8	0.0	3.76	0.472	0.375	0	0	1775	1870.0
2E1	100741-19	0.4A	8/8	100.0	1.31	0.082	0.291	31	13.1	3784	11936.4
2E1	100741-21	0.4A	8/8	100.0	1.59	0.077	0.087	29	9.1	307	8.6
2E1	100741-22	0.4A	0/8	0.0	44.35	-0.212	0.536	0	0	336	13.4

Notes: J factor = 0.003608 ± 0.00036